Holography Measurement for Crossed-Dragone Type Telescope & its Application to the Fred Young Submm Telescope

Inaugural-Dissertation
zur Erlangung des Doktorgrades
der Mathematisch-Naturwissenschaftlichen Fakultät
der Universität zu Köln

Vorgelegt von

XIAODONG REN

aus Shanxi

I. Physikalisches Institut
Universität zu Köln
2023

Gutachter:
Prof. Dr. Jürgen Stutzki
Prof. Dr. Ralf Bulla

Abstract

Microwave Holography is an accurate and efficient method for measuring the surface shape of large reflector antennas. The method is based on the Fourier transform relationship between the antenna's far-field diffraction beam pattern and its aperture field. Measuring the antenna's far-field beam both in amplitude and phase can deduce the aperture field distribution. The phase deviations of the aperture field are directly related to the antenna's surface shape. This technique has become a well-established method for surface metrology of large radio telescopes because of its high efficiency and measurement accuracy.

However, employing the traditional holography cannot identify the surface deformity in a 'two-reflector' antenna system. This thesis investigates a new multi-map holography metrology to overcome this limitation. The new method is developed to align the Fred Young Sub-millimeter telescope (FYST), a coma-corrected Crossed-Dragone antenna with two 6-m off-axis reflectors. The surfaces of the two reflectors must be aligned to be better than 10.7µm. The multi-map holography identifies the surface errors between the two reflectors by taking five holographic beam measurements by placing the receiver at well-separated points in the focal plane. The parallactic shift of the surface errors allows assigning them to either one of the two mirrors. A new data processing technique is developed using an inference technique to simultaneously analyze the five beams and convert them to two surface error maps. Extensive numerical simulations have been carried out to check the feasibility, measurement accuracy, and optimum set-up of the new holographic system by modeling the systematic errors in the system, such as random instrument noise and fluctuation of performance of the instruments. These indicate that a measurement accuracy of $\sim$ 2µm is achievable.

The critical part of the data processing technique of the 'Multi-map' holography is to develop a fast and accurate beam simulation algorithm. The conventional physical optics method is very time-consuming for analyzing the FYST antenna. A new 'two-step' Kirchhoff-Fresnel diffraction method is developed, which, compared to the conventional physical optics analysis, can reduce the computational time by four orders of magnitude without noticeable accuracy degradation.

The new multi-map holography and its data processing technique are implemented

to measure the reflector errors for a 0.4-m diameter Crossed-Dragone antenna in the laboratory. The experiments prove that the errors on the two reflectors can be discriminated and accurately measured with a statistic error lower than 1µm. The holographic measurements and reflector corrections also indicate that the large spatial errors existing on the two reflectors also can be measured.

Contents

1. Background and Introduction **12**

1.1. Background of Radio Astronomy 12

1.2. Alignment of Large Radio Telescope 14

1.2.1. Surface Tolerance Theory 16

1.2.2. Microwave Holography Technology 17

1.3. Fred Young Sub-mm Telescope, FYST 20

1.3.1. Instruments: Prime-Cam and CHAI 21

1.3.2. 'Coma-corrected' Crossed-Dragone Optics 23

1.3.3. Reflectors and Support Structure 24

1.4. Challenges in the FYST Holography 24

1.5. Organization of the Thesis 27

2. Optics Simulation for FYST **29**

2.1. Introduction of Physical Optics Analysis 30

2.1.1. PO currents 31

2.1.2. Surface currents integral 32

2.1.3. Far-field Characteristics of a Parabolic Antenna 34

2.2. PO Analysis for FYST 36

2.2.1. PO analysis flow 37

2.2.2. Near-field Beam Pattern 38

2.2.3. Diffraction effect of panel edges 40

2.3. 'Two-step' PO analysis Technique 44

2.3.1. Fields on the Intermediate Plane 45

2.3.2. Equivalent Currents 49

2.3.3. Accuracy 50

2.4. 'Two-step' Fresnel-Kirchhoff Analysis 53

2.5. Summary 55

3. Microwave Holography Technology **56**
3.1. Fundamentals of Microwave Holography 56
3.1.1. Spatial Resolution 59
3.1.2. Measurement Accuracy 61
3.1.3. Far-field Holography Measurement 62
3.2. Near-field Holography Measurement 63
3.3. Primary Holography Design for FYST 64
3.4. Summary 68

4. Multi-map Holography for a Two-Reflector System **69**
4.1. Introduction 69
4.2. Multi-map Microwave Holography Technique 70
4.2.1. Geometrical Optics Analysis 71
4.2.2. New Analysis Technique 72
4.3. Numerical Simulations for the FYST Holography 83
4.3.1. Effect of Random Noise and Holographic Setup 87
4.3.2. Effect of Atmospheric Turbulence 89
4.3.3. Optical Alignment Mismatch 91
4.3.4. Telescope Pointing Errors 92
4.3.5. Effect of Panel Fabrication Errors 94
4.3.6. Summary and Error Budget 95
4.4. Star Sampling Pattern 96
4.5. Summary 98

5. The FYST Holographic System **99**
5.1. Hardware Design 99
5.2. Beam Measurement and Data Analysis Procedure 107

6. Holographic Test for a Small Crossed-Dragone Antenna **112**
6.1. Overview the Holographic Testbed 112
6.1.1. Small Laboratory Antenna 112
6.1.2. Holographic Design 114
6.2. Experiment 1: Conventional One-beam Holography Analysis 120
6.2.1. Surface Diagnosis for the Smooth Reflectors 120
6.2.2. Diagnosis for Artificial Surface Errors in the Reflectors 125
6.2.3. Summary 127
6.3. Experiment 2: Multi-map Holography Measurement 127
6.3.1. Analysis for the Distorted Reflectors in Experiment 1 128

6.3.2. Analysis for the Case with Artificial Degenerate Errors 130
6.3.3. Measurement Accuracy 133
6.3.4. Summary 134

7. Conclusion and Outlook **136**

Bibliography **139**

Appendices **152**

A. Optical Parameters of FYST and Laboratory Antenna **152**

B. Optics in the Reference Receiver Module **158**

List of Figures

1.1. Five general telescope optical geometries. 15
1.2. A polar power pattern of a parabolic antenna. 15
1.3. The Ruze's analysis about reflecting antenna efficiency. 16
1.4. Effects of large-spatial reflector deformations on antenna's far-field beam. 17
1.5. Rendering of FYST on Cerro Chajnantor and its cross-section view. . . 20
1.6. Atmospheric transmission at Llano de Chajnantor and Cerro Chajnantor. 21
1.7. Overview of CHAI receiver design 22
1.8. Diffraction-limited Field of View of the FYST telescope. 23
1.9. Carbon-Fiber backup structure and backside of panels. 24

2.1. Geometry of an symmetrical parabolic reflector. 33
2.2. Far-field beam pattern of a 6-m diameter parabolic antenna. 35
2.3. The schematic of the FYST optics. 36
2.4. Standard Physical Optics analysis flow for crossed-Dragone antenna. . . 38
2.5. The simulated near-field beam pattern of the FYST telescope at 296GHz. 39
2.6. The beam pattern of the FYST with defocused optics. 40
2.7. Radiation pattern caused by the panel edges. 42
2.8. Radiation pattern caused by panel edges at 148GHz. 43
2.9. The calculation flow of the two-step Physical Optics method. 44
2.10. Gaussian beam transformation elements. 46
2.11. The equivalent optics of the secondary mirror of the FYST telescope. . . 47
2.12. The computed co-polarization and cross-polarization beams in the intermediate plane. 48
2.13. Comparison of the focused beams simulated by PO analysis and two-step PO method. 51
2.14. Comparison of the defocused beams simulated by PO analysis and two-step PO method respectively. 51
2.15. The difference patterns between the simulated fields calculated by using the PO analysis and two-step PO analysis. 52
2.16. Illustrating the Fresnel-Kirchhoff diffraction. 53

2.17. Diagram of the field diffraction by a reflector. 54
2.18. Diagram of the virtual diffraction field on the intermediate plane behind a mirror. 55

3.1. Principle of the microwave holography technique. 58
3.2. Diagram of the microwave holography measurement. 59
3.3. Spatial resolution of a holography measurement. 60
3.4. Equivalent Signal-to-noise ratio of a corrector receiver. 62
3.5. Location of FYST and the holographic source. 66
3.6. The locations of the Signal Receiver and reference receiver in the telescope. 67
3.7. Schematic of the FYST holographic measurement system. 67

4.1. The reflection points on M2 of the FYST telescope for the incoming light from three different angular directions. 72
4.2. The FYST optical layout for lights from different directions. 74
4.3. Diffraction field distributions on the M1 surface. 74
4.4. Distortions of a square panel and the positions of its adjusters. 76
4.5. Beam calculation process in the inference holographic analysis 79
4.6. Flowchart of the holographic analysis procedure. 82
4.7. Optics layout of the FYST telescope with a source at 300m away from the telescope and the holographic receive mounting positions. 84
4.8. The cut of the FYST's focused beam and out-of-focus beams. 84
4.9. Surface error maps of the two reflectors of FSYT. 86
4.10. Amplitude beam pattern of the simulated holographic beam maps with the receiver at five different points in the focal plane. 86
4.11. Deviations of the best-fitting reflector surfaces from the input surfaces where the measurement SNR is 65 dB. 87
4.12. The RMS of the surface measurement errors as a function of SNR of the measurement system and the receiver spacing. 88
4.13. Effect of the gain and phase fluctuations of the instruments on the measurement accuracy. 89
4.14. Temporal power spectrum of the phase fluctuations assumed for simulation of atmospheric effects. 90
4.15. Phase errors produced by atmospheric variations and the errors after calibration. 90
4.16. Beams modified by large spatial errors caused by inaccuracy of the receiver position and beam size. 91

4.17. The comparison of the measured telescope's beams and beams produced by the fitting reflector surfaces. 92
4.18. The effect of telescope pointing error on the accuracy. 93
4.19. Simulated telescope pointing error. 94
4.20. Fabrication errors of the panels on the two reflectors of FYST. 95
4.21. A 'star' scanning pattern. 97
4.22. Measurement accuracy of the cases using a 'star' scan pattern. 97

5.1. Radiation pattern of the conical-spline horn. 100
5.2. Schematic of the source. 101
5.3. Holographic source optical layout and CAD model. 101
5.4. Schematic of the receiver module. 102
5.5. View of receiver module with part of the cover removed. 102
5.6. The mount for the signal receiver in the telescope focal plane 103
5.7. Close-up view of the signal receiver module at one of the mounting positions. 103
5.8. Cut-away view of the reference receiver. 104
5.9. Diagram of the digital back-end correlator 105
5.10. Characterization of the vector voltage meter system. 106
5.11. A possible star scan pattern for the FYST holography measurement. . . 108

6.1. Optical layout of the designed Lab antenna. 113
6.2. CAD model of the scaled laboratory telescope and its two reflectors. . . 114
6.3. Simulated beam map of the Lab antenna. 114
6.4. Receiver mounting positions in the focal plane. 116
6.5. Focused optics of the Lab antenna for the source located at 5 meters. . . 116
6.6. Simulated beams of the Lab antenna with different amounts of defocus. 117
6.7. Setup of the laboratory holographic testbed. 118
6.8. Schematic of Lab electronic connection. 119
6.9. The initial measured beam of the Lab antenna and the simulated beam pattern for the ideal reflectors. 121
6.10. Measured beam pattern in amplitude and phase for the Lab antenna. . 121
6.11. Measured equivalent surface error in M1. 123
6.12. Simulated beam in different analysis stages. 124
6.13. Comparison of the equivalent surface errors in M1 analyzed by different software methods. 125
6.14. Artificial piston errors in M1 and M2 using copper foil and plastic tape. 125
6.15. The measured focused beam distorted by copper foils. 126
6.16. Measured artificial piston errors in M1. 126

6.17. Five measured beams of the Lab antenna with artificial errors on the reflectors. 128
6.18. Measured surface error maps of the Lab antenna using 30 × 30 parameters on each reflector. 128
6.19. Error maps analyzed using Zernike Polynomials to express the surface deviations. 129
6.20. Surface errors producing overlapped phase errors on the aperture plane. 130
6.21. Measured beam maps distorted by the reflector errors in figure 6.20 . . 131
6.22. Solved error maps of the Lab antenna using the focused and out-of-focused multi-map holographic measurement. 131
6.23. Holography analysis results after correcting the twist error on the M1 surface. 132
6.24. Measured focused beam after fixing the twist errors on M1. 133
6.25. Surface errors on M1 and M2 using high precise copper foil with thickness of 10µm and 20µm. 134
6.26. Measured surface error maps for the 10µm surface errors. 134

A.1. 2D layout slice showing the modified crossed-Dragone optical design for FYST. 153
A.2. Diagram of the FYST optics. 154
A.3. Diffraction limited FOV of the coma-corrected optics as a function of frequency. 156

B.1. Schematic diagram of Gaussian beam propagation. 159
B.2. Schematic of Gaussian beam transformation by a elliptical mirror. . . . 160
B.3. Schematic of the Gaussian transformations of the two-mirror system. . . 161
B.4. View of the CAD mode of the reference receiver module and optics. . . 162
B.5. Simulated beam of the designed reference receiver optics. 162
B.6. Simulated beam maps of the designed reference Rx optics. 163

Chapter 1.

Background and Introduction

1.1. Background of Radio Astronomy

Radio astronomy is a branch of observational astronomy which studies celestial objects through their radio emission using radio techniques. In 1932, K. G. Jansky, while working as a radio engineer for Bell Telephone Laboratories, detected natural radio emission from the center of our Galaxy at 20.5MHz (14.6 m wavelength) [1] and unexpectedly opened the radio observational window for astronomical research. Following Jansky's discovery, Grote Reber built a 9.6-m parabolic radio telescope and systematically observed at 160MHz (1.9 m), eventually confirming the discovery and suggesting that the observed signal is non-thermal radiation. Today, with tremendous improvements in radio techniques, people today can easily observe 21-cm (1.42GHz) line [2], which is emitted by neutral hydrogen atoms in our Galaxy, using a home-made 0.5-m tinfoil horn and a commercial software-define-radio (SDR) receiver. The frequency range of radio astronomy is roughly from 10MHz to 1THz. The high boundary is limited by the atmospheric opacity and given at the boundary between radio and far-infrared astronomy. The low-frequency boundary is limited by the Earth's ionosphere which reflects signals with a frequency below 10MHz. Through the radio window, a set of sources have been discovered, for example, thermal spectral-line emission from cold interstellar gas atoms and molecules, maser emission from interstellar [3], the 2.7K cosmic microwave background (CMB) radiation from the hot big bang [4], and extrasolar planets[5].

The development of solid-state technology for Schottky mixers and extremely low noise amplifiers and the implementation of superconductivity devices in radio instruments significantly improve the sensitivity of the radio telescopes, enabling the observation frequencies at millimeter (1mm $< \lambda <$ 10cm) and sub-millimeter (0.3mm $< \lambda <$ 1mm) bands. These bands cover a great number of spectral lines, for example, the rotational lines of CO and atomic lines of carbon in 350µm and 650µm bands, which are useful

for studying astrophysical process like the star formation within molecular clouds. The frequency peak of the 2.7K CMB radiation is in the millimeter band at 160.2GHz (1.9 mm). Measuring the B-mode polarization patterns of the CMB radiation [6] are important to detect the primordial gravitational wave, which would lead to the support to the inflation hypothesis. Inverse Compton scattering of the CMB photons by the hot electrons ($> 10^6$ K) in the gravitational wells of galaxy clusters results in a spectral distortion of the CMB due to the shift in photon energy, which is called thermal Sunyaev-Zeldovich (t-SZ) effect [7]. Using the CMB radiation as a backlight, the t-SZ effect offers an excellent approach to tracing the mass, spatial distribution, and peculiar motions of galaxy clusters.

Observation in millimeter and sub-millimeter bands on the ground-based observatory is limited by the attenuating nature of the Earth's atmosphere. In the millimeter band, the atmosphere is almost completely transparent except for a few broadened absorption lines of water vapor (22.235GHz) and Molecular oxygen O_2 (60GHz). The most critical limitation for sub-millimeter signals is the broadband absorption of water vapor in the atmosphere above the telescope expressed by precipitable water vapor (PWV). Hence, millimeter and sub-millimeter telescopes are commonly constructed in places where the climate is very dry, mostly also high, such as the Atacama Large Millimeter Array at an altitude of 5100 m in north Chile [8] and the CCAT observatory at 5600m, to minimize atmospheric attenuation. Even though, still, some spectral lines are blocked out by absorption and only can be observed from space or airborne observatories, for example, Herschel Space Observatory [9] and SOFIA airborne telescope [10]. But ground-based telescopes still have virtues compared to space and airborne telescopes. Telescopes with large and precise reflectors can be constructed on the ground to achieve better angular resolution and sensitivity. Telescope instruments can also be easily upgraded with the newest state-of-the-art receivers techniques, like efficient receivers with more pixels and wider operating bandwidth because of no weight, size, or power electricity limitations.

Another difficulty for millimeter and sub-millimeter observations is about constructing telescopes with high surface precision. The tolerance theory of random errors in the antenna surface indicates that an error of $\lambda/16$ root-mean-square deviation (RMS) leads to 50% loss of the antenna's efficiency that is the limit of the acceptable roughness of radio antenna surface. For a telescope operating in 350µm (850GHz) atmospheric window, the required surface deviations must be less than 21µm. Radio telescopes generally require large aperture sizes because they suffer from extremely poor angular resolution. According to Rayleigh criterion ($\theta = 1.22\lambda/\mathrm{D}$, D is the diameter of a telescope)[11], a 10-m telescope operating in 350µm has an angular resolution of about nine arcseconds, but a 10 cm diameter optical telescope can easily achieve an angular

resolution of about one arcsecond. Constructing a 10-m telescope with 20µm surface precision is very challenging. The common way is to segment the reflectors into a set of small and easily manufactured panels, and individual panels are supported by three or more adjustable screws called adjusters. This allows that reflectors can be adjusted to the desired shapes. Therefore, a technique that can measure the surface shapes with accuracy even less than the surface precision (< 10µm) becomes critical.

This thesis focuses on the development of metrology with a measurement accuracy of < 2µm for the coming Fred Yound Sub-millimeter Telescope located at 5600 m high. The specificity of this telescope is presented in section 1.3. The new challenges of the surface diagnosis for this telescope are detailed in section 1.4. The following section reviews the methods of measuring large reflector antennas.

1.2. Alignment of Large Radio Telescope

Most of today's radio telescopes operating in millimeter and sub-millimeter have an optical design with two reflectors: one large parabolic reflector used to achieve the required high angular resolution and referred to as the primary reflector, and a relatively small secondary reflector employed to fold the light path and make the telescopes more compact. If the required size of the antenna is larger than a few hundred operating wavelengths, an optical design similar to those of optical telescopes can be used. Optical layouts commonly used by radio telescopes are shown in figure 1.1. The radio receiver or detector is mounted in the focus of the optics. Then, the ray length from a planar wavefront to the focus is a constant for all reflection points on the reflectors, which means the collected signals are coherently added at the focus. Equivalently, suppose a transmitter replaces the receiver. In that case, the lights from the transmitter will be reflected to produce a planar wave and give a constant wavefront in any aperture plane. The far-field diffraction pattern propagated from such aperture has a narrow main beam and many sidelobes referred to as error beams. An excellent antenna can concentrate as much energy as possible into its main beam and compress the power levels of its error beams. Based on the reciprocity theorem in radio antenna, the receiving and transmitting properties of radio antennas are equivalent. In the following thesis, all simulated antenna beams are transmission patterns.

Any surface deviations of the reflectors in figure 1.1 will change the ray lengths and also modify the phase of the aperture field. Then the non-uniform aperture phase will degrade the gain of the main beam and increase the power levels of the sidelobes. The optical propagation in the reflector antennas has a Fourier transformation relationship between the far-field complex (amplitude and phase) beam pattern and the aperture

complex field. This is explained in detail in chapter 2. Figure 1.2 shows the distorted beam of a simple parabolic antenna with aperture phase errors of 30° RMS.

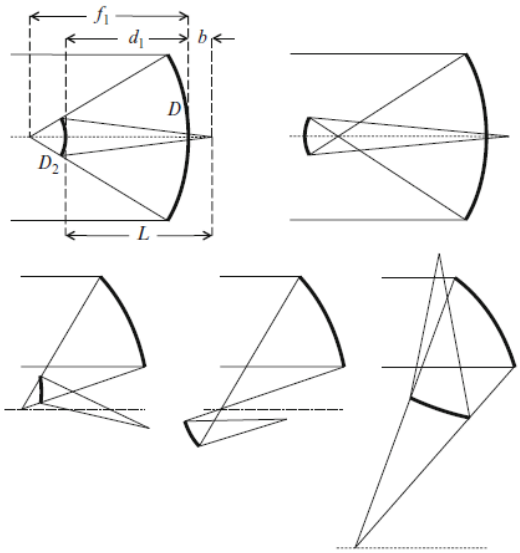

Figure 1.1.: Five general telescope optical geometries [12]. On-axis symmetrical Cassegrain (top left) and Gregory (top right), their off-axis configurations (bottom left and center), and the crossed-Dragone optics (bottom right). The horizontal dotted line in each diagram is the optical axis of the primary reflector. D and D_2 are the diameters of the primary and secondary reflectors.

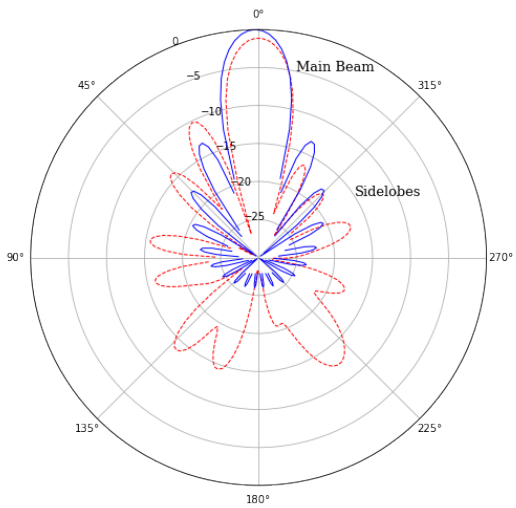

Figure 1.2.: A polar power pattern of a parabolic antenna. The ideal beam pattern (Blue) and the distorted beam pattern (red).

1.2.1. Surface Tolerance Theory

Deformity of reflector surfaces degrades the wave optical performance of the designed telescopes. In 1952, Ruze published his 'tolerance theory' of a statistical surface error in antenna reflectors [13]. Ruze's analysis gives the relationship between the random surface errors in the antenna reflector and the antenna's efficiency. If the surface error is small with respect to the operating wavelength and randomly distributed with a Gaussian distribution, the efficiency reduction or axis gain loss can be expressed as the following formula,

$$\frac{G(\delta)}{G_0} = e^{-\delta^2}, \ \delta = \frac{4\pi\epsilon}{\lambda} \tag{1.1}$$

where G_0 is the gain of the antenna with perfect surfaces, δ is the wavefront error caused by antenna surface errors ϵ. Figure 1.3 illustrates the antenna's efficiency as a function of operating wavelength or frequency for the case with different surface deviations [14]. It can be seen that a surface error of 1/16th wavelength RMS results in one-half efficiency reduction, and a value of 1/20th RMS reduces the antenna's gain to $\sim 67\%$ of the maximum. The power loss in the antenna's main beam is converted into the sidelobes, which increases the gain of the antenna's error beams and degrades the signal-to-noise (SNR) ratio of the antenna, see figure 1.2.

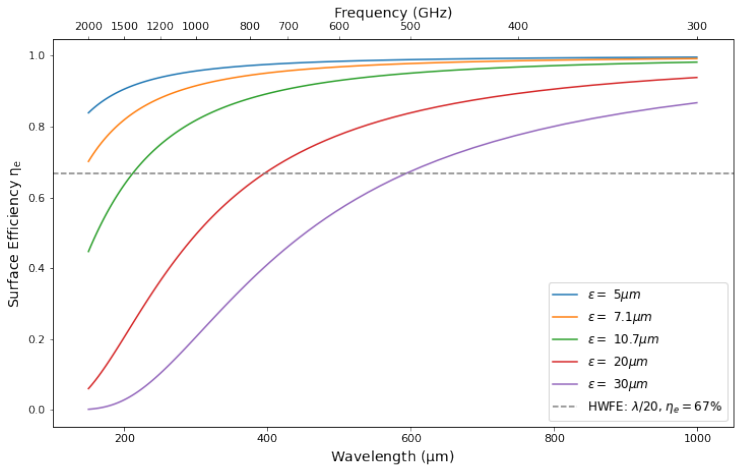

Figure 1.3.: The Ruze's analysis about the relationship of reflecting antenna efficiency and half wavefront error (HFWE) of incident light caused by its surface deviations, ϵ represents RMS of the surface deviations, and λ is the operating wavelength.

The following error sources contribute to the overall surface errors of reflector antennas: 1) profile errors in individual reflector panels, which are determined by the manufacturing

precision; 2) distortion caused by temperature difference in the telescope structure; 3) deformations produced by the wind stresses; 4) gravitational deformation of the panels and panel backup structure; 5) panel setting errors depending on the accuracy of the chosen method of the surface diagnosis.

The distortions caused by the thermal effect, gravity, and wind stresses generally produce surface errors in large spatial scales, for example, astigmatism, coma, and other large-scale features. These errors mostly reshape the main beam and increase the gain of near-in sidelobes. If the telescope observes extended objects, the near-in sidelobes with higher income also watch parts of the source, which results in overestimation of the source intensity and degrades the sensitivity of the telescope. Figure 1.4 presents the simulated beams with different large-spatial scale surface deformations. The simulations are based on the Fourier transformation relationship between the aperture fields of the reflector antenna and its far-field radiation beam pattern [15].

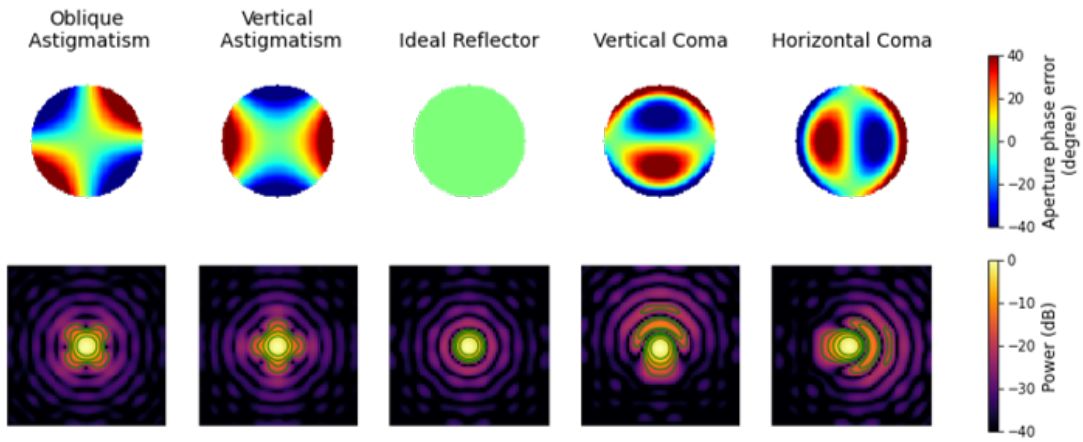

Figure 1.4.: Effects of large-spatial reflector deformations on antenna's far-field beam. The top plots are the phase deviations in the aperture plane. The bottom is the responding beams. The contour lines represent the values of -20, -15, -10, -5, and 0 dB from outer to inner. The beams are simulated using the Fourier Transform relationship between aperture fields and far-field beam[15][16].

After alignment, the desired surface precision of the antenna reflector should be better than 1/20th (5%) of the shortest operating wavelength. In order to achieve this precision, the error contributed by the surface measurement errors must be better than one or two percent of the wavelength. Therefore, it is desirable to have an approach to accurately and efficiently measure the surface profiles of the reflector antenna.

1.2.2. Microwave Holography Technology

The Fourier transform (FT) relationship between the aperture fields and far-field beam pattern of a reflector antenna has been discussed by S. Silver in his book 'Microwave

Antenna Theory and Design' [17] published in 1949. If the antenna's far-field beam pattern is measured both in amplitude and phase, the aperture field distribution can be given by making an inverse FT to the measured complex pattern. The surface deviations on the antenna's primary reflector are then deduced by geometrical optics if assuming the small secondary reflector is perfect. Bates and Napier published two papers [18][19] and presented the theory of the idea and experimental confirmations in 1971. Unfortunately, these papers did not attract the attention of astronomers. Until Richard Hills returned to Cambridge in the UK and suggested this method to Scott and Rylc, they measured the beam pattern of four of the eight antennas of the 5-kilometer synthesis telescope array [20] at 15.4GHz, both in amplitude and phase by using another four antennas as a phase reference. The measurement accuracy of ~ 0.1mm was achieved for the spatial resolution of ~ 1.5m, around one-panel size. The experimental tests were published in 1977 [21]. This method of measuring reflector surface profile has been called microwave holography.

The critical process of the microwave holography measurement is to accurately measure the far-field beam pattern of the antenna under test both in amplitude and phase. In order to get the phase of the beam, an additional antenna is required to keep observing a point source, e.g. available satellites and astronomical sources like 22.235GHz water maser in Orion [22] and provide a phase reference. Then the antenna under test is scanned across the source. Two receivers are mounted in the focal plane of the antennas and share the same reference, the receiver in the tested antenna is denoted by the signal receiver, and another is named the reference receiver. The amplitude of the signal receiver and the phase difference between the two receivers are recorded. The fundamentals of microwave holography and the designing criteria are detailed in Chapter 3. This technique has been widely used for large radio telescopes, such as 100-m Effelsberg telescope holography at 11.78GHz [23], 30-m IRAM millimeter radio telescope holography using the 22.235GHz Water Maser source [24] and so on. The test time of this technique is typically from the whole night to a few hours, according to the specific observation conditions. The accuracy of the method depends on the SNR of the measured antenna beam pattern, which is always in the range of $0.001\lambda < \sigma < 0.01\lambda$. For example, the 30-m IRAM holographic experiment achieved a measurement accuracy of around 25µm (0.002λ). This method analyzes the reflector surface profiles by measuring the telescope's beam, which is the antenna characteristics we want to improve. Repeating the reflector corrections and holographic analysis, we can check the correctness of the previous measurement and reflector correction. Based on this technique, there are some variations of the microwave holography approaches that are developed for special test conditions, like near-field holography measurement and phase

retrieval holography.

Near-Field Holography Measurement The accuracy of the holographic measurement is generally limited by the SNR of the reference antenna, which is generally much smaller than the antenna under test. To achieve the required measurement accuracy, an artificial source with strong output power will be used and placed relatively close to the antenna so that the reference receiver can achieve a high enough SNR without using an additional large telescope. But the measured antenna response is in the near field, and the Fourier transform relationship does not work any more. Instead a complex transform should be used. The near-field holography technique has been successfully implemented for several sub-millimeter telescopes, for example, measuring the 12-m Vertex ALMA telescopes at 104GHz and achieving a measurement accuracy of 8µm and 15-m James Clerk Maxwell Telescope (JCMT) at 80GHz and 160GHz with an accuracy of 5µm [25][26]. The main disadvantage of this method is that the surface analysis only can be measured for the telescopes pointing at one elevation defined by the elevation of the source.

Phase Retrieval Holography If direct phase measurement is difficult, the phase retrieval holography, introduced by Morris in 1985 [27], only requires the power response of the telescope. Therefore, extremely sensitive astronomical receivers and detectors can be employed to measure the telescope's power beam pattern with excellent SNR. The phase distribution in the aperture is estimated by measuring at least two power beam maps of the telescope with putting the receiver along the optical axis to either side of the focal plane. Then the method is often called out-of-focus (OOF) holography. Two analysis methods, the Missel algorithm suggested by Morris [27] and numerical inference technique developed by Nikolic [28], have been developed to analyze the surface shapes for the 30-m IRAM telescope [29], 100-m Green Bank Telescope (GBT) [28] and the 3-m Kölner Observatorium für SubMillimeter Astronomie (KOSMA) [30].

1.3. Fred Young Sub-mm Telescope, FYST

The Fred Young Sub-millimeter Telescope (FYST) [31][32], formally CCAT-prime, is a 6-m diameter, 10µm surface precision telescope located at an altitude of $\sim$ 5600 meters on Cerro Chajnantor in the Atacama Desert of northern Chile where is the second highest ground-based observatory (the highest is the University of Tokyo Atacama Observatory at 5640 meters). Figure 1.5 left shows the rendering of the telescope on Cerro Chajnantor. This high site offers an extremely dry atmosphere and excellent observational conditions. Figure 1.6 illustrates the Cerro Chajnantor's atmospheric transmission [33][34] compared to that on the ALMA site, which is around 5100 meters high on the Chajnantor plateau. It indicates that the PWV of the Cerro Chajnantor site is 40% lower than the ALMA site under normal atmospheric conditions (50% observing time). Around 10% observing time, the PWV on the Cerro Chajnantor is the value of about 0.21 mm. At the best observational condition, the dry atmosphere makes it possible to open the observation in the 200µm (1.5THz) atmospheric window. Through this window, the [NII] 205µm emission line can be observed from the ground-based observatory, which is very useful to trace the gas in the ionized region associated with newly formed early-type stars [35].

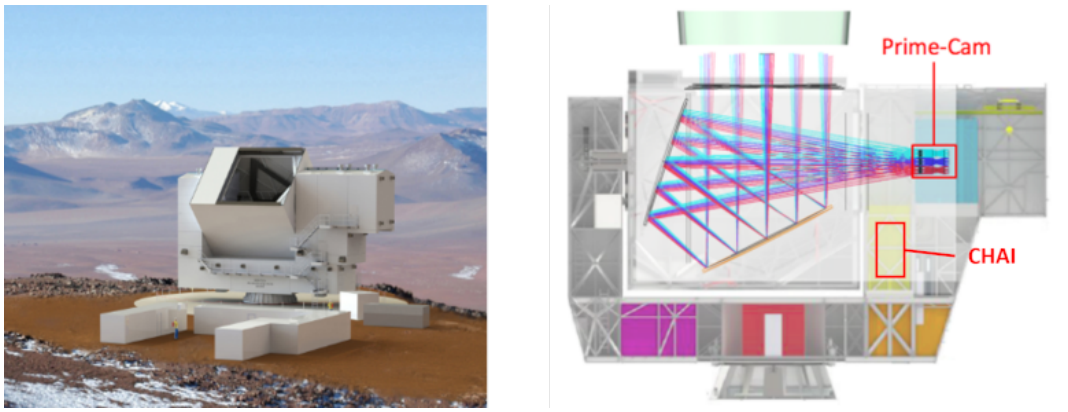

Figure 1.5.: Left: The Rendering of FYST [36]; right: the cross-section view of the FYST telescope and its optical layout. The instrument spaces are highlighted, the Prime-Cam [37] in the focal plane and the CCAT-prim Heterodyne Array Instrument (CHAI) marked by a yellow cubic, which needs extra optics to pick up the light from the telescope optics [38].

FYST will be an exceptional 6-meter survey telescope that uniquely combines the features of a large field of view (7.8° at 3 mm wavelength), high antenna efficiency, and excellent atmospheric transmission due to the superb site, its special Crossed-Dragone optics shown in the cross-section view of figure 1.5, and the advanced instruments. The rest of the section presents the first-light instruments of the telescope and its novel

optics.

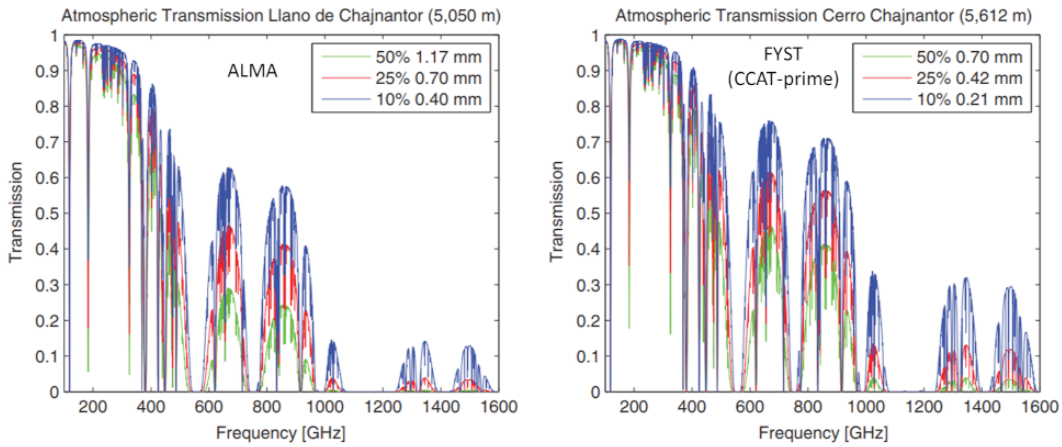

Figure 1.6.: Atmospheric transmission in the millimeter and sub-millimeter bands for Llano de Chajnantor (left) and Cerro Chajnantor (right) [39]. The transmissions are calculated using the observed 350µm zenith optical depths and the ATM model. The green, red, and blue lines indicate the transmission for 50%, 25%, and 10% of the observing time, respectively. The corresponding values of PWV are listed in the insert list.

1.3.1. Instruments: Prime-Cam and CHAI

FYST will accommodate two the-state-of-art instruments: Prime-Cam instrument [40][37][41] and the spectroscopy of the CCAT-prime Heterodyne Array Instrument (CHAI). The space of the two instruments is highlighted in figure 1.5.

Prime-Cam will be the first generation camera directly located at the focal plane to fill the central 4.9° of the 8° diameter field of view of the telescope. The instrument uses the direct-detection technique which only detects the power of the incident signals and cannot keep the phase information. The sensitive elements will be two superconducting detectors: transition-edge-sensor (TES) bolometers [42] and Microwave kinetic inductance detectors (KIDs) [43]. The two detectors are designed to operate at a temperature of around 100 mK. The instrument is split up into seven independent instrument modules that are housed together in a 1.8 meters diameter cryostat. Each module fills up to a 1.3° diameter field-of-view and is separated by 1.8°. These modules can be exchanged separately to meet different scientific purposes. The seven modules include: five broadband polarization-sensitive detector arrays to observe at five frequencies, 220GHz, 280GHz, 350GHz, 410GHz and 850GHz [44] for the wide field survey, and two spectrometer modules that utilize Fabry-Perot interferometers (FPIs) and the sensitive detectors to map the line intensity from 210 to 420GHz which are corresponding to redshifts

z=3.5-8.05 in the 158µm [CII] line and the [OII] 88µm line from the ionized medium at z>7.

The second first light instrument for FYST will be CHAI which will be developed by the University of Cologne. It is a dual-band heterodyne array spectrometer primarily designed to map extended sources in the two neutral atomic carbon fine-structure lines and the nearby rotational lines of carbon monoxide. The low-frequency array (LFA) operating from 455 to 495GHz will cover the [CI] $^3P_1 \rightarrow {}^3P_0$ 492GHz line and the CO $J = 4 \rightarrow 3$ (460GHz) rotational line. The 800-820GHz high-frequency array (HFA) will get access to the 350µm atmospheric window and observe the [CI] $^3P_2 \rightarrow {}^3P_1$ (809GHz) fine-structure line and the CO $J = 7 \rightarrow 6$ (807GHz) line. The two arrays consist of 8×8 pixels, respectively. They can simultaneously observe the sky in a field of view of $7.5' \times 7.5'$ for LFA and $4.5' \times 4.5'$ for HFA.

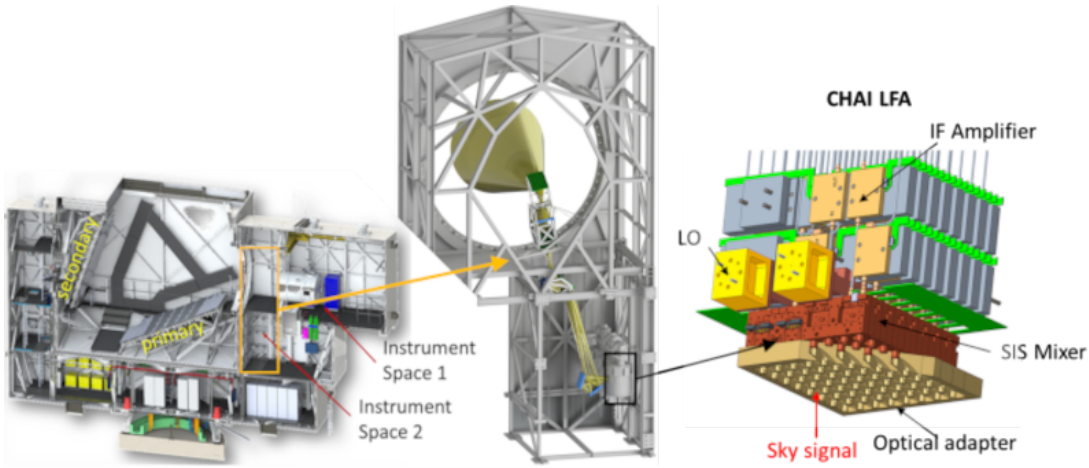

Figure 1.7.: Overview of the location (left) and the schematic of CHAI (right), and the beam path of the low-frequency array of CHAI from elevation bearing to down to the cryostat (middle).

CHAI uses the heterodyne technique, which converts the high-frequency signals from the sky to a lower-frequency band where the signal can be easily processed using conventional electronics. The heterodyne technique is based on the property that the multiplication of two input signals of slightly different frequencies results in a set of new signals that are the frequency difference between the two input signals. If the amplitude and phase of one input signal maintain constant, the produced new signal can reflect the changes of another input signal. The former signal is called a local oscillator (LO). The new signal is commonly called the intermediate frequency (IF). CHAI uses the advanced Superconductor-Insulator-Superconductor (SIS) mixers [45] to multiply the local oscillator and the sky signal. The IF output of each pixel of CHAI is from 4 to 8GHz and analyzed in a digital Fourier transform spectrometer with 100kHz spectral

resolution. The instrument will be placed in the second instrument space marked in figure 1.5. A complex optical system is designed to pick off the central part of incoming light from the FYST optics and deliver the light down to the CHAI receiver to the second instrument space [46]. The CAD model of the complex optics and the CHAI receiver is shown in figure 1.7.

1.3.2. 'Coma-corrected' Crossed-Dragone Optics

FYST has a novel Crossed-Dragone optics, which consists of two 6-meter reflectors. The optics is designed by satisfying the Mitzuguchi-Dragone conditions [47][48] to achieve the performance of zero-blockage aperture, large field-of-view (FoV), and excellent polarization isolation [49]. The feature of zero-blockage aperture can significantly improve the antenna's aperture efficiency (the ratio of effective illumination area to the physical area), which the conventional antennas like Cassegrain and Gregorian configurations suffer from the optical path blockage caused by their small secondary reflectors and the supporting structures. Since the optical beam of a radio receiver feedhorn mounted is Gaussian, and the beam power is mainly confined in the center of the region, which unfortunately is blocked by the secondary reflector. For example the aperture efficiency of the APEX telescope [50] is less than 60%. In addition, its large FoV and excellent polarization isolation make the telescope to be the next-generation CMB telescope [51], so the Simons Observatory Large Aperture Telescope (SOLAT) [52] also adopted the same optical design of FYST for the CMB-stage 4 experiments [53].

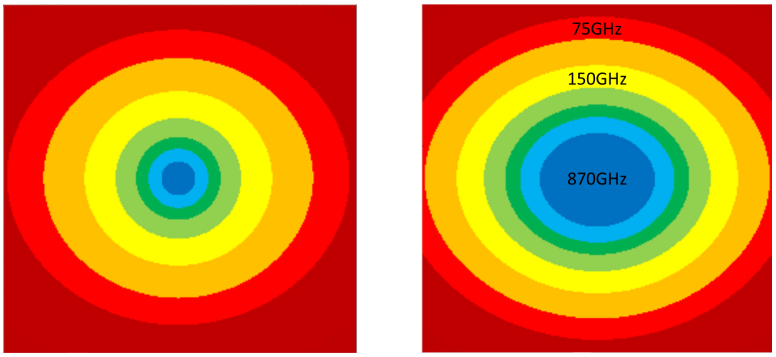

Figure 1.8.: DLFOV regions in an 8 by 8 degree field as a function of frequency with the standard crossed-Dragone design on the left and the coma-correction optics on the right. The colors (blue through red) show the regions where the Strehl ratio is > 80% at 870, 490, 345, 230, 150, 100, and 75GHz, respectively.

The primary design is based on Michael D. Niemack's study in paper [54]. Then the telescope FOV is further improved by Stephen C. Parshley and Richard E. Hills [55] applying additional coma-correction terms on its two reflectors. The diffraction-

limited field-of-view (DLFOV), where the Strehl ratio is $> 80\%$, is extended to 26 deg^2 at 2 mm wavelength and 4.4 deg^2 at 350µm. The DLFOV changes before and after the coma corrections are presented in figure 1.8. It can be seen that the DLFOV is significantly enhanced, especially at higher frequencies. The polarization performance of the modified optics was studied by Gallardo, P. in paper [56] by using commercial software GRASP [57], and it was found that the coma-corrected optics still maintains the low cross-polarization intrinsic to the classical design. The details of the FYST's geometry and the profiles of the modified reflectors are summarized in Appendix A.

1.3.3. Reflectors and Support Structure

The two 6-m reflectors of FYST must be segmented into panels. The panels are made from light-weighted aluminum plates and mounted onto a carbon-fiber backup structure (figure 1.9 left). There are 146 panels, 77 panels on M1 with sizes of 670×750mm 69 on M2 with panel sizes of 700×710mm. The panel sizes are chosen to ensure that the surface distortion caused by thermal gradient across the panel can be tolerated. The panels have been manufactured with a surface precision of < 3µm [58]. All panels have the same backside structure and consist of five z-axis adjusters shown in figure 1.9 (right), which allow the panels can be finely adjusted to correct the low-order panel distortions after the panel assembly.

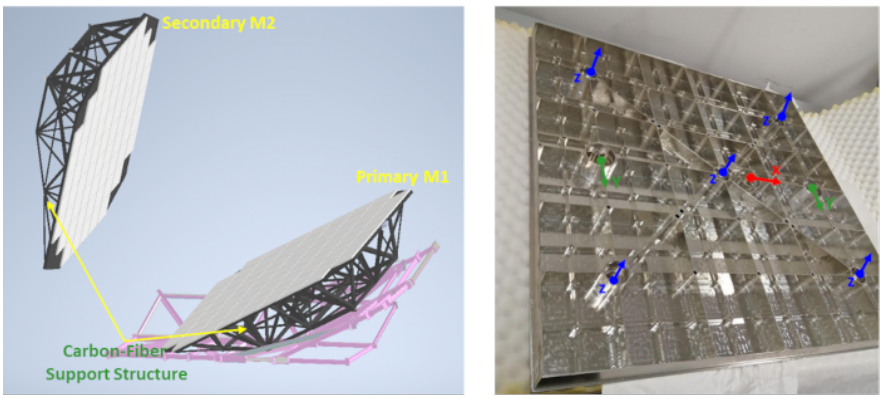

Figure 1.9.: Carbon-Fiber backup structure (left) and backside of panels (right) of the FYST's reflectors.

1.4. Challenges in the FYST Holography

To enable the observation in the $200-$µm atmospheric window, the reflectors of FSYT must be aligned to be more precise than 10.7µm, with a goal of < 7.1µm. Although the reflectors will be set to the correct shape with high precision in the factory and then

shipped to the site fully assembled, we regard it as essential to have an accurate method of measuring under operational conditions. We planned to use microwave holography for this. Because this technique has a well-proven record for the measurement of large sub-millimeter telescopes. For example, the 12-m ALMA telescopes were aligned by implementing a 104.02GHz near-field holography [59] and achieving surface accuracy of 20µm with the measurement accuracy of 8µm. But applying this technique to FYST presents several significant challenges:

1. The requirement on surface accuracy is for the whole telescope system, including manufacturing errors and items like deformations due to the changing orientation of the telescope and environment temperature. We expect the results from the holography measurements to be used for the final adjustment of the reflector panels, so any errors in the measurement will also contribute to the final surface errors. Therefore, we cannot allow them to take up more than a small fraction of the required error budget. We planned to adopt a goal of < 2µm under best test conditions, where this should include both random errors, e.g., those due to instrument noise and atmospheric fluctuations, and systematic errors due, for example, to inconsistency between the actual antenna and the designed model, and inaccurate modeling the antenna's electromagnetic effects. To the best of our knowledge, the FYST holography measurement is a significantly higher accuracy than has been reported for such measurement thus far.

2. The difficulty of measuring the surface shapes for the two reflectors using conventional microwave holography. The conventional approach employs a simple inverse Fourier transformation of the measured complex (amplitude and phase) beam pattern of the antenna under test. This can provide a map of the wavefront distortion at the aperture, which is the phase error contributed by the surface errors of the two reflectors. It cannot identify the error sources in the optical system. Therefore, a new technique is required to break the degeneracy in the two-reflectors system.

3. Since the measurements will often be made at night, it is not allowed to have personnel present at the telescope in the evening because of the high altitude. It must be possible to operate all aspects of the system remotely.

In addition to the above challenges, we also expect the measurement to be made fast enough so that the effect of thermal changes over the whole day can be studied. To meet the < 2µm measurement accuracy, a high operating frequency ($\sim$ 300GHz) is used, and an artificial source is designed and placed close to the telescope, which means the

measurement will be done in the near field. Using a higher frequency means that a given fractional error in measuring the beam pattern converts into a smaller surface measurement error because of the shorter wavelength. The high frequency also offers a narrow beam, which minimizes the effect of reflection of the signal by the ground and other objects between the telescope and the source. The close artificial source provides a strong signal to illuminate the telescope and get a high signal-to-noise ratio (SNR), which means that the noise from the instrument contributes to small errors in the measured surface shapes, even with measurement times as short as a few milliseconds per point. The relationship between the measurement accuracy, operating wavelength, and required SNR of the system is detailed in Chapter 3 of this thesis. Using short distance also minimizes the atmosphere volume so that the phase variations caused by the atmospheric fluctuations are reduced.

The central theme of my Ph.D. work is to develop a new technique to solve the degeneracy problem in Crossed-Dragone optics or any two-reflector systems. I discussed this issue with Richard Hills and Urs Graf in Cambridge, England, and we concluded that the degeneracy could be broken by making beam maps with the receiver at several well-separated positions in the focal plane because the projections of the panels on the two reflectors could be separated at the aperture plane. Since the new method requires more than one beam map, we call it 'Multi-map' holography. But the new issue is that there is no obvious direct method for converting the measured beam maps into two surface error maps, analogous to an inverse Fourier transform. Instead, we treat this as a numerical inference problem, which requires two parts: finding a way to parameterize the reflector surfaces and developing a fast and accurate algorithm for simulating the beam maps produced by the parameterized reflectors. To realize this method, a new approach to simulate the wave optical performance of the FYST's antenna has been developed, which is a critically important part. In turn, massive numerical simulations were studied to prove the feasibility of the multi-map holography and find the best configuration and measurement approach.

The development and test of the holographic hardware were conducted in parallel with the study of the new holographic technique. Before I was involved in the FYST holography project, the basic holographic design based on microwave holography theory had been discussed by Urs Graf and our collaborators, Nicolás Reyes from Max-Planck Institute and the University of Chile, Richard Hills from the Cambridge of University, and Stephen Parshley from Cornell University. The source and receivers were designed using commercial microwave components produced by RPG-Radiometer Physics GmbH [60]. Pablo Astudillo from Universidad de Chile designed, tested, and packed the source and receiver modules. The back-end digital correlator and its controlling software were

designed and programmed by Sebastian Jorquera in Chile based on the Re-configurable Open Architecture Computing Hardware (ROACH2) [61] platform. In March 2020, at the beginning of covid-19 pandemic, I visited Universidad de Chile to learn about the back-end correlator from Sebastian and measure the designed receiver feedhorn with Pablo. Richard and I studied and developed the optics for the reference receiver. Lars Weikert, Urs Graf, and the Mechanical workshop at Universität zu Köln helped me design and manufacture all mechanical structures, such as the receiver mounting structure in the focal plane, reference receiver optics, and the mounting frame for a small Crossed-Dragone antenna. In November 2021, all instruments were delivered to Köln and assembled to build a testbed to check the feasibility of the novel multi-map holographic method. The laboratory tests exhibit a promising and encouraging outlook for the future FYST holography test.

1.5. Organization of the Thesis

This dissertation is dedicated to the alignment of the reflectors for the Fred Young Sub-millimeter Telescope using microwave holography technology. The central theme of the thesis is to study and test a new holographic metrology for a 'two-reflector' configuration antenna, e.g., the Crossed-Dragone antenna used by FYST, which consists of two 6-m diameter reflectors that need to be measured and aligned. One critical aspect of the new metrology is to exploring an efficient method to calculate the wave optical performance of FYST, which is employed in the new software analysis technique. Furthermore, the experimental results of using the new holographic method on a small laboratory antenna are detailed. The whole thesis is structured into three parts:

1. **Optical Simulation** (Chapter 2). This part is about developing a method to predict the wave optical performance of the FYST telescope efficiently. The method is the key to the new holography technique discussed in the next part. In Chapter 2, the physical optics (PO) analysis technique is first demonstrated and applied to explain the diffraction theory of reflecting antenna, which provides the theoretical background under the holography technique. The wave optical performances of the FYST telescope simulated by the commercial software TICRA GRASP [57] using the PO analysis are presented. The effect of the FYST reflectors' panel edges on the optical performance is also investigated. Two new analysis techniques are studied to improve the efficiency of the PO analysis for FYST, and the accuracy of the two methods is reported in comparison with the results from the commercial software.

2. **Holographic Analysis** (Chapter 3-5). This part focuses on the microwave holography design for the FYST telescope, including the basic design of the holography method, the challenge of analyzing the reflector errors in the FYST's 'two-reflector' optics, and the new approach developed to solve the challenge. Chapter 3 explains the fundamentals of microwave holography and its design criterion and presents the primary holographic design for the FYST telescope. Chapter 4 addresses the difficulty of measuring the surface errors for the FYST's two reflectors using the conventional holographic method. To overcome this challenge, a new approach named 'Multi-map' holography, which analyzes the surface errors of the 'two-reflector' system by measuring multiple complex (amplitude and phase) beam maps is developed and investigated by numerical simulations. Chapter 5 details the hardware design of the FYST holographic system and the optimal measurement approach and data analysis procedure based on the preceding theory and simulations.

3. **Experiments and Conclusion** (Chapter 6-7). The developed 'Multi-map' holography technique is implemented to analyze the reflector surface errors for a small Crossed-Dragone antenna constructed for the holographic testbed. The feasibility of the new approach and the accuracy of the designed FYST holographic system are investigated and reported. In Chapter 6, the Lab antenna's optics and its holographic setup are detailed. The conventional holographic analysis is applied to check the performance of the beam measurement system, and it is also shown that discriminating the errors on the two reflectors using the one-beam holographic measurement is difficult. Finally, the multi-map holographic measurements are implemented to measure the surface errors produced by copper foils of known thickness. The experimental results are reported in the measurement accuracy and the ability of surface error discrimination between two reflectors. In Chapter 7 the conclusion and outlook for future work are presented in Chapter 7.

Chapter 2.

Optics Simulation for FYST

The key to the FYST holography measurement is to solve the issue of surface error degeneracy between the telescope's two reflectors. In 2018, I discussed this problem with Richard Hills in Cambridge and decided to analyze the surface errors by measuring multiple beam maps of the telescope. Richard suggested treating the surface analysis as an inference issue and solving the reflectors' surface shapes using numerical fitting techniques. Then the critical step is to build the fitting function, also called the 'forward function', which must precisely and fast compute the telescope's beam maps based on the given reflector surfaces.

Therefore, this chapter presents a fast and accurate method to simulate the diffraction beams of the special 'Crossed-Dragone' type antenna that FSYT uses. The developed approach also can be employed to speed up the optical simulations for any multiple reflector optics. The discussion starts with the fundamentals of the physical optics (PO) analysis used for modeling general reflector antennas. Then, the PO method is employed to calculate the far-field diffraction beam for a simple parabolic reflector. The simulated far-field beam indicates the Fourier transform relationship in the antenna radiation theory, which is the basis of understanding microwave holography technology. Then, the PO analysis is implemented to study the near-field diffraction beam for the FYST telescope. Since FYST is made of square aluminum panels, the diffraction effect of its panel edges is modeled by commercial software, TICRA GRASP [57], using the PO method and physical theory of diffraction (PTD). Next, two novel alternative methods, 'two-step' PO analysis and 'two-step' scalar Kirchhoff diffraction method, are developed to speed up the FYST beam simulations. The two new techniques can efficiently predict the diffraction fields of FYST without notable field accuracy degradation. The computational efficiency has been improved by four orders of magnitude compared to the conventional PO analysis.

2.1. Introduction of Physical Optics Analysis

A reflector antenna is an excellent option for radio astronomical observations, especially in millimeter and sub-millimeter bands, because the reflecting optics can offer a very low loss in radio frequency compared to refractive optics and can fold the optical path to make the telescope more compact. Since astronomical signals are usually extremely weak, the reflectors of radio telescopes commonly have a large diameter to provide a large collection area so that a high enough gain and high angular resolution can be achieved to observe faint and compact celestial objects. If the size of the radio telescope is thousands of its shortest operating wavelength, the geometrical optics (GO) method can be used to preliminarily design the telescope's optical layout. But the diffraction effects in large radio telescopes still cannot be neglected. The telescope's characteristics, such as the gain, main beam size (angular resolution), and levels of error beams, must be carefully considered. Therefore, after the optical design, a more precise diffraction analysis is required to fine-tune the optics so that the radio telescope can achieve the optimum performance, for example, high main beam efficiency and very low levels of error beams. To precisely analyze the telescope' wave-optical performance, a set of methods have been developed for the large reflector antenna, such as the most fundamental physical optics (PO) approximation [62][63], the physical theory of diffraction (PTD) [64][65] and geometrical theory of diffraction (GTD) [66][67].

In this section, the PO approximation technique is demonstrated and employed to analyze the diffraction optics of a simple parabola antenna illuminated by a Gaussian beam. Because the commonly two-mirror optical system, like Cassegrain, Gregorian, and their off-axis configurations shown in figure 1.1, can always be represented by an equivalent symmetrical parabolic reflector[68] based on geometrical optics. The PO analysis for the simple parabolic reflector gives the general optical characteristics of the reflector antenna.

In the actual telescope observations, the signal propagates from a distant source through the telescope's reflectors and into the receiver. If we scan the telescope over a point source and record the responses of the focal receiver, the recorded beam pattern is the reception pattern of the telescope. For numerical analysis, it is more convenient to simulate the equivalent time-reversed process (transmitting pattern), starting from the receiver and through the telescope's optics, to calculate the field on a spherical surface at the distance of the source. The reciprocity theorem [69] implies that an antenna's reception and transmission patterns are equivalent. Therefore, in the rest of this chapter, all simulated beam maps are transmission patterns.

The diffraction issue of a reflector antenna is about calculating scattered fields with

knowing antenna geometry and incident field. When an incident electromagnetic wave illuminates a reflector, surface currents are induced. If the reflector is perfectly conducting, its scattered fields are generated by these induced surface currents. Therefore, predicting the diffraction fields of a reflector antenna can be considered a three-step procedure. The first step is to calculate induced currents on the reflector; if the reflector is not a perfect conductor, the equivalent induced surface currents are used based on electromagnetic boundary conditions. The next step is to calculate the scattered fields radiated by the induced surface currents in Step 1. This calculation has a rigorous solution deduced from Maxwell's equations. Finally, the calculated scattered fields and the incident fields from the device, e.g., the receiver, which illuminates the reflector, are summed up to get the total diffraction field at the point we want to study. The last two steps are straightforward. The first step, estimating induced surface currents, becomes the most critical process. Generally, the method of moments is used to get a rigorous solution by meshing the entire antenna space. But, it is very time-consuming because the reflector is much larger than the operating wavelength. The physical optics method offers a valid approximation to compute the surface currents for perfectly conducting reflectors if the reflector is smooth and much larger than the operating wavelength.

2.1.1. PO currents

The basic PO method assumes that the induced surface current in a specific point on a curved reflector surface is equal to the surface current on an infinite flat surface if the dimension and surface curvature of the reflector is sufficiently larger than the wavelength of the incident light. An infinite perfectly conducting plane is illuminated by an arbitrary field called incident fields $\mathbf{H}_i$, the boundary conditions define the surface current as equation 2.1,

$$\mathbf{J}_e = \tilde{\mathbf{n}} \times \mathbf{H}, \tag{2.1}$$

where $\mathbf{H}$ represents the total magnetic fields which include the incident field and reflected or scattered field ($\mathbf{H} = \mathbf{H}_i + \mathbf{H}_r$), and $\tilde{\mathbf{n}}$ is the surface normal vector which points outward from the illuminated side of the surface. For the infinite perfectly conducting plane, the reflected magnetic field equals the incident magnetic field ($\mathbf{H}_i = \mathbf{H}_r$), then we get the equation 2.2.

$$\mathbf{J}_e = \vec{n} \times (\mathbf{H}_i + \mathbf{H}_r) = 2\vec{n} \times \mathbf{H}_i. \tag{2.2}$$

This equation gives a good approximation of simulating the induced currents on a curved surface. The method also assumes induced current is zero in the regions not

illuminated by the incident field. The PO method cannot deal with discontinuities in reflector surfaces, such as reflector edges and gaps where the PO approximate currents differ from actual currents. But these unusual currents are commonly concentrated in the region of less than a few wavelengths, so the effect can be ignored if the reflector size is much larger than the operating wavelength. For high precision requirements, the physical theory of diffraction (PTD) is used to correct PO currents at the discontinuous regions.

2.1.2. Surface currents integral

Once induced PO current distribution is known, the electromagnetic fields at any point can be found by summing the radiation fields contributed by all current elements. With introducing vector potential $\mathbf{A}$ (defined by $\mathbf{H} = \frac{1}{\mu}\nabla \times \mathbf{A}$), substituting it to Maxwell equations, and assuming the field is harmonic time dependence and written as $e^{-j\omega t}$, one can easily derive the wave equation as

$$\nabla^2 \mathbf{A} + k^2 \mathbf{A} = -\mu \mathbf{J}_e \tag{2.3}$$

where k is the wave number expressed by $k = \omega\sqrt{\epsilon\mu} = 2\pi/\lambda$. One wave equation solution is given by equation 2.4 [70].

$$\mathbf{A}(\vec{r}) = \frac{\mu}{4\pi}\int_{S'} \mathbf{J}_e \cdot \frac{e^{-jkR}}{R} ds', \quad R = |\vec{r} - \vec{r'}| \tag{2.4}$$

Here, R is the distance between current source $\vec{r'}$ and target field point P denoted by $\vec{r}$ in Figure 2.1, and the term of $\frac{e^{-jkR}}{R}$ is the Green function, which represents field on target point contributed by a unit current element. The integration is carried out over the entire surface S', which contains all current sources. From the calculated vector potential in the target field point, one can obtain the magnetic and electric fields by equation 2.5.

$$\mathbf{E}(\vec{r}) = -j\omega\mathbf{A} - \frac{j}{\omega\mu\epsilon}\nabla(\nabla \cdot \mathbf{A}) \tag{2.5a}$$

$$\mathbf{H}(\vec{r}) = \frac{1}{\mu}\nabla \times \mathbf{A} \tag{2.5b}$$

Then, replacing the vector potential in equation 2.5 with equation 2.4 and applying the vector operators on the current vectors and Green function, finally, the electric and magnetic fields on the target points can be calculated by following the integral equation,

$$\mathbf{E}(\vec{r}) = \frac{1}{4\pi}\sqrt{\frac{\mu}{\epsilon}}\int\int_{S'}\Big(\mathbf{J}_e(-\frac{j}{kR} - \frac{1}{k^2R^2} + \frac{j}{k^3R^3}) \tag{2.6a}$$
$$+ (\mathbf{J}_e \cdot \hat{\mathbf{R}})\hat{\mathbf{R}}(\frac{j}{kR} + \frac{3}{k^2R^2} - \frac{3j}{k^3R^3})\Big)e^{-jkR}k^2ds'$$
$$\mathbf{H}(\vec{r}) = \frac{1}{4\pi}\sqrt{\frac{\epsilon}{\mu}}\int\int_{S'}\mathbf{J}_e \times \hat{\mathbf{R}}\frac{1}{k^2R^2}(1 + jkR)e^{-jkR}k^2ds' \tag{2.6b}$$

where $\hat{\mathbf{R}}$ is the unit vector pointing from current source point to field point, defined by $\hat{\mathbf{R}} = \frac{\vec{r}-\vec{r'}}{|\vec{r}-\vec{r'}|}$. The area element ds' can be expressed by a weighted flat area element in x'-y' plane denoted by $ds' = J_s \cdot dx'dy'$. Figure 2.1 shows the geometry of a symmetrical parabolic reflector, illustrates the vectors mentioned above, and surface currents integral. Here, the x'-y' plane is the projection area of the integral surface S', and J_s is the weight factor that is called Jacobian transformation expressed as

$$J_s = \left[1 + \left(\frac{\partial f}{\partial x'}\right)^2 + \left(\frac{\partial f}{\partial y'}\right)^2\right]^{1/2}, \tag{2.7}$$

f is the function of x' and y', used to describe the surface S' profile. Then, the surface integral is converted to a two-dimension integration. The telescope's aperture plane is commonly chosen as the x'-y' integral plane. Under geometrical optics approximation, the light from the focal receiver through the telescope's optics is converged to parallel output light. The reflected light is perpendicularly projected to an infinite plane called the aperture plane. Consequently, the above interpretation indicates that the field point outside the reflector surface can be computed by the knowledge of electromagnetic field distribution over the reflector surface.

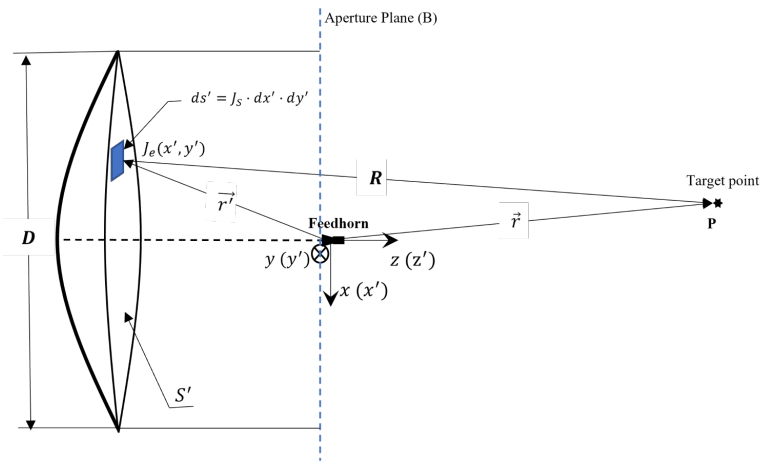

Figure 2.1.: Geometry of an symmetrical parabolic reflector.

2.1.3. Far-field Characteristics of a Parabolic Antenna

The PO approach is employed to analyze the radiation performance of a parabolic reflector in near and far field regions. The formulas 2.6 deduced in section 2.1.2 can be used to predict radiation fields at any point in finite distance from telescope. However, for the application of radio telescope, the far-field electromagnetic performance is more critical. To express it, the coordinate of the field point is replaced by angular coordinate. The far field is defined by

$$\mathbf{E}_{far} = \lim_{r\to\infty}[\mathbf{E}(r)kr\ e^{jkr}] \tag{2.8a}$$

$$\mathbf{H}_{far} = \lim_{r\to\infty}[\mathbf{H}(r)kr\ e^{jkr}], \quad (r = |\vec{r}|). \tag{2.8b}$$

Substituting equations 2.6 in above definitions gives the far-field expression,

$$\mathbf{E}_{far} = -\frac{j}{4\pi}\sqrt{\frac{\mu}{\epsilon}}\int\int_B(\mathbf{J}_e - (\mathbf{J}_e\cdot\hat{r})\hat{r})e^{jk\vec{\mathbf{r}'}\cdot\hat{r}}k^2 J_s dx' dy' \tag{2.9a}$$

$$\mathbf{H}_{far} = -\frac{j}{4\pi}\sqrt{\frac{\epsilon}{\mu}}\ \hat{r}\times\int\int_B \mathbf{J}_e e^{jk\vec{\mathbf{r}'}\cdot\hat{r}}k^2 J_s dx' dy', \tag{2.9b}$$

where $\hat{r}$ is the far-field direction and defined by $\frac{\vec{r}}{|r|}$. B is projection area of the reflector on its aperture plane shown in Figure 2.1. If the reflector optics is focused, the radiation fields is confined in a small angular range in far field, the phase term $\vec{\mathbf{r}'}\cdot\hat{r}$ in formula 2.9 can be simplified as

$$\begin{aligned}\vec{\mathbf{r}'}\cdot\hat{r} &= z'\ cos(\theta) + ux' + vy' \\ &\approx z' + ux' + vy',\end{aligned} \tag{2.10}$$

where

$$u = sin\theta cos\phi,\ v = sin\theta sin\phi. \tag{2.11}$$

Since the far-field direction $\hat{r}$ is closely perpendicular to the parabolic surface, the field component along radiation direction that is expressed by $(\mathbf{J_e}\cdot\hat{r})\hat{r}$ in formula 2.9 can be neglected, and substituting equation 2.10 and 2.11 into equation 2.9a, one obtains

$$\mathbf{E}_{far}(u,v) = -\frac{j}{4\pi}\sqrt{\frac{\mu}{\epsilon}}\int\int_B \widetilde{\mathbf{J}}\cdot e^{jk(ux'+vy')}dx' dy' \tag{2.12}$$

$$\widetilde{\mathbf{J}} = \mathbf{J}_e\cdot J_s\cdot e^{jkz'} \tag{2.13}$$

$\widetilde{\mathbf{J}}$ can be treated as the projection of reflector surface current on aperture plane, and called aperture current distribution. Formula 2.12 indicates that a Fourier Transforma-

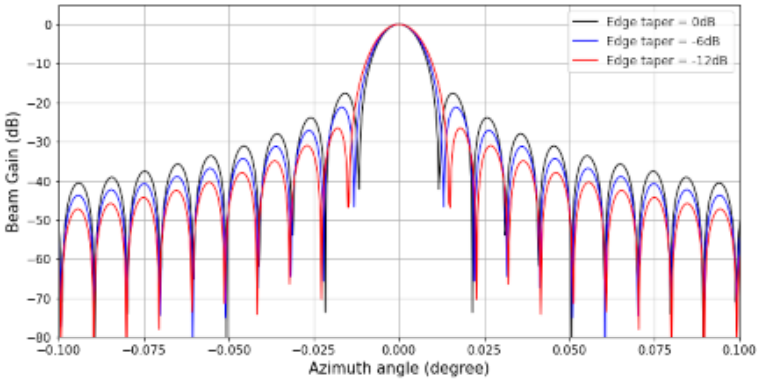

Figure 2.2.: Far-field radiation beam of 6 meter parabolic reflector operating at 296GHz with illumination edge taper of 0,-6, and -12dB.

tion relationship exists between telescope's far radiation fields and its aperture fields. Neglecting the integral sign and multiplier factor, the inverse Fourier Transformation of formula 2.12 can be written as

$$\widetilde{\mathbf{J}}(x^{'}, y^{'}) = \int\int \mathbf{E}_{far}(u, v) \cdot e^{-jk(ux^{'}+vy^{'})} du\ dv. \tag{2.14}$$

Hence, if the fields in the telescop's aperture plane are known, the diffraction beams of radio antenna in far field can be easily predicted by using Fourier transform algorithm. Figure 2.2 shows the far-field diffraction beams of a 6-meter symmetrical parabolic antenna illuminated by a Gaussian beam. The divergence of the incident Gaussian beam is changed to produce a illumination edge tape of 0, -6, and -12 dB. The illumination edge tape is defined by the ratio of field intensity at antenna center and edge. It is found that the large edge taper compresses telescope side-lobes, reduces noise coupled from its error beams, but degrades the angular resolution of the antenna.

Conclusively, the PO analysis method offers the way to precisely predict the diffraction beams of a reflector antenna based on the antenna's geometry and the illumination beam. Properly choosing input beam shape and modifying surface profile of the antenna can achieve required optical performance, such as narrow main beam size, low level of error beams and large field of view. The Fourier transformation relationship explained above is very important for understanding the microwave holography used for surface diagnosis of large reflector antenna, which derive the antenna geometry by measuring the antenna's diffraction beam map. If the far-field beam pattern $\mathbf{E}_{far}(u, v)$, including amplitude and phase, is measured, the current projection in aperture plane $\widetilde{\mathbf{J}}(x^{'}, y^{'})$ can be fully determined also in amplitude and phase by making inverse Fourier transform to recorded beam map. The phase of the current distribution is used to recover reflector

geometry. The details of this technique will be presented in Chapter 3.

2.2. PO Analysis for FYST

FYST uses a particular crossed-Dragone optical configuration, an offset dual-reflector antenna. Figure 2.3 shows the schematic of the FYST optics. An essential property of this optical design is zero blockage in the telescope aperture, so high efficiency and low error beams can be achieved. Its initial optical design uses the classical configuration, which satisfies the 'Mizuguchi-Dragone' condition [47][48][71] to minimize the first-order astigmatism aberration by following the method presented by Granet in paper [72]. Based on the classical design, comatic aberrations are corrected by reshaping the two mirror surfaces to improve the field of view further. The details of the optical design were summarized by Stephen C. Parshley in paper [55]. The optical parameters and mirror surface profiles are listed in appendix A. This section presents the simulations of the electromagnetic performance of the telescope.

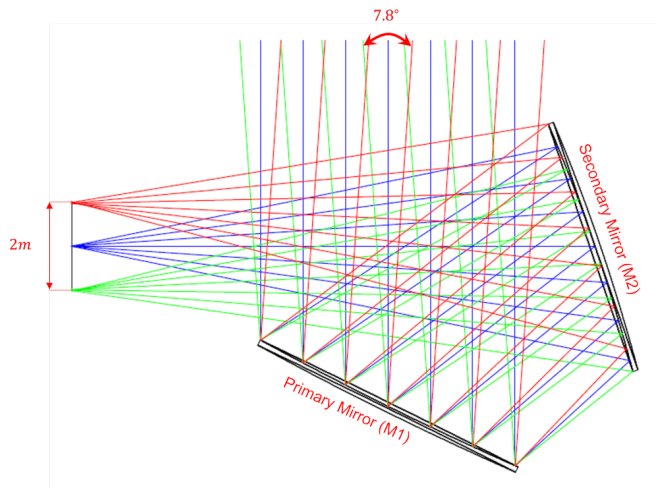

Figure 2.3.: The schematic of the FYST optics. The rays are shown for the lights from the Sky with offset angles of −3.9, 0 and +3.9 degrees.

The easiest way of estimating the FYST's electromagnetic characteristics, for example, the beam size and the levels of its sidelobes, is to simply treat the dual reflectors as an equivalent parabolic reflector [68][73][63] illuminated by a Gaussian beam from a receiver horn in the parabolic focus. Then employing the PO analysis to the equivalent reflector can predict the focused beam pattern. The simulated beam at 1mm wavelength is shown in figure 2.2. However, this method neglects the diffraction effects of the wave propagation between M2 and M1, and this parabolic equivalent method is only valid for the case where the receiver is located at the telescope's geometrical focus. In order to

study the field of view of the telescope, the receiver should be placed at a point that is offset from the optical axis.

Another approximation method uses the geometrical optics (GO) or geometric theory of diffraction (GTD) to calculate the field propagation from M2 to M1. The telescope's radiation fields are predicted by employing PO analysis for the M1 reflector. The GO and GTD techniques are fast but inaccurate or impractical for simulating antennae in microwave. For example, the two methods are hard to model Gaussian beam propagation, and the fields scattered by a finite reflector also cannot be expressed. In addition, the FYST's two reflectors are segmented into rectangular panels, and the diffraction feature of each panel also needs to be considered.

The most accurate and direct approach is to apply the PO analysis to model the wave propagation from M2 to M1, then continue the PO analysis for the fields scattered by M1 to the Sky. This means the PO analysis needs to be implemented twice. We call this analysis process the full PO analysis. This offers very high field accuracy but at the cost of computation time. In this section, the full PO analysis process is first explained and used to model the FYST radiation fields in the near field. The results are used as a gold standard to study the accuracy of the new techniques developed in the rest of the chapter.

2.2.1. PO analysis flow

In the actual telescope observation, the incident wave from a distant source is first collected by M1, reflected to M2, and delivered to the focal receiver. Adopting the time-reversed process is more convenient for modeling the telescope's transmission performance. The signal starts from the receiver, through the telescope optics, and propagates to the distant sky or a region at a finite distance from the telescope. The predicted field is the telescope's transmission pattern. In accordance with the reciprocal theorem [15], the reception and radiation patterns of a telescope are identical.

Figure 2.4 illustrates the wave propagation from the receiver to the region of the fields that we want to know. This involves finding the induced PO currents on M2 by the field radiated from the receiver horn, the calculation of the fields at the surface of M1 excited by those PO currents in M2, and hence finding the currents on M1 and finally, calculating the radiation fields that the currents on M1 produce at the required region. The calculations suffer from the tremendous amount of computing time of calculating the fields in M1 surface produced by PO currents in M2 because the two same-sized ($\sim$ 6m) reflectors are sited too close, 6 meters between their centers, and phase variation of the current integration is very rapid. To precisely simulate the fields at the M1 surface, for the case of a telescope operating at 300GHz ($\sim$ 1mm), the sampling interval

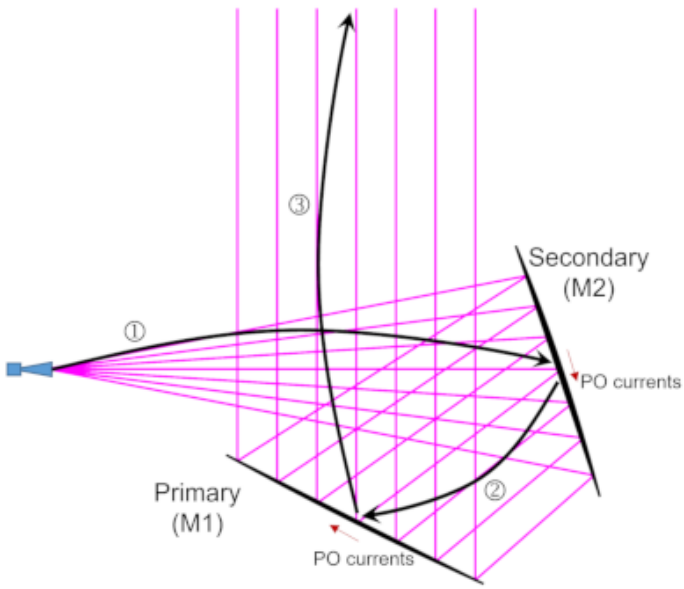

Figure 2.4.: The standard Physical Optics analysis process for the crossed-Dragone dual reflector antenna. Here the plot is the FYST telescope optical layout.

of PO currents in M2 needs to be less than half wavelength ($\sim 10^8$ sampling points in M2) because of the phase variations of the PO current integral. The simulations were done by the commercial TICRA GRASP package that is a software commonly used for reflecting antenna simulations, and took around a week for one beam simulation by a machine with 100 CPUs.

2.2.2. Near-field Beam Pattern

Since the holographic measurement of FYST is planed to be done in near field, an artificial source operating at $\sim$ 300GHz ($\sim$ 1mm wavelength) is mounted at $\sim$ 300m away from the telescope, predicting the radiation beam in near field is very important for holographic system development and simulations. The near source changes the new focus of the optics to $\sim$ 705mm behind its original focus, which can be easily computed by geometrical optics. The focused radiation beam maps, including the co-polarization beam map and its cross-polarization pattern, are shown in figure 2.5. The strong cross feature in the diffraction patterns is caused by straight mirror rims. The cross-polarization beam is around 65dB lower than the desired polarization beam peak.

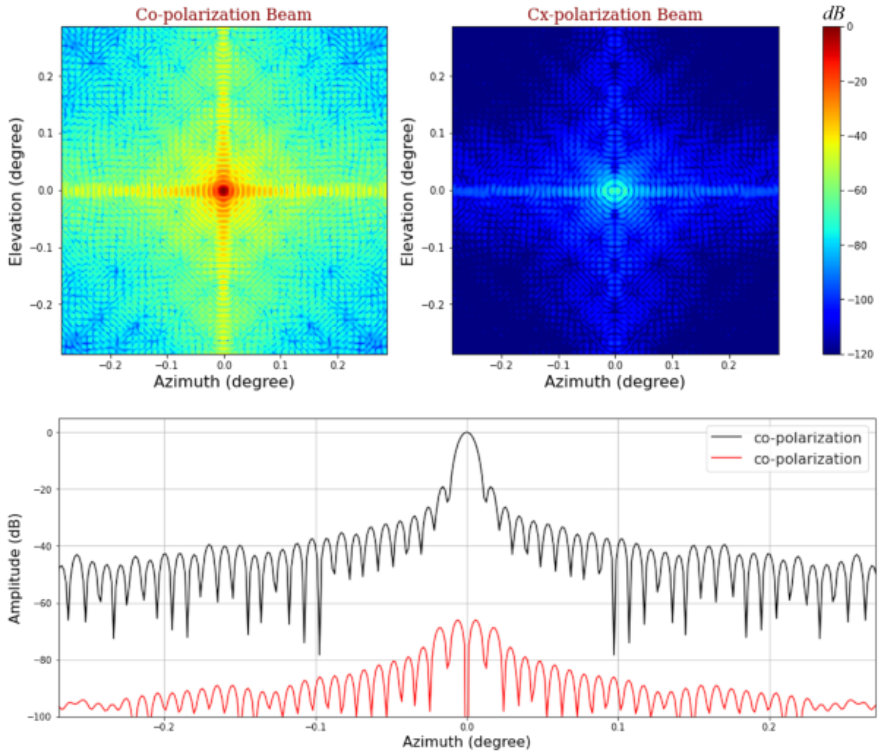

Figure 2.5.: The near-field radiation beam of the FYST telescope at the frequency of 296GHz is simulated with using physical optics analysis. The output beam from feed horn is linear polarization in x direction. The calculated field region is 300 meters away from telescope aperture. The receiver is moved to 705mm behind the nominal focus to re-focus the optics. Top plots are the simulated beam pattern with x polarization (left), and its radiation beam with y polarization (right). Bottom is the cut plots of the beam in azimuth.

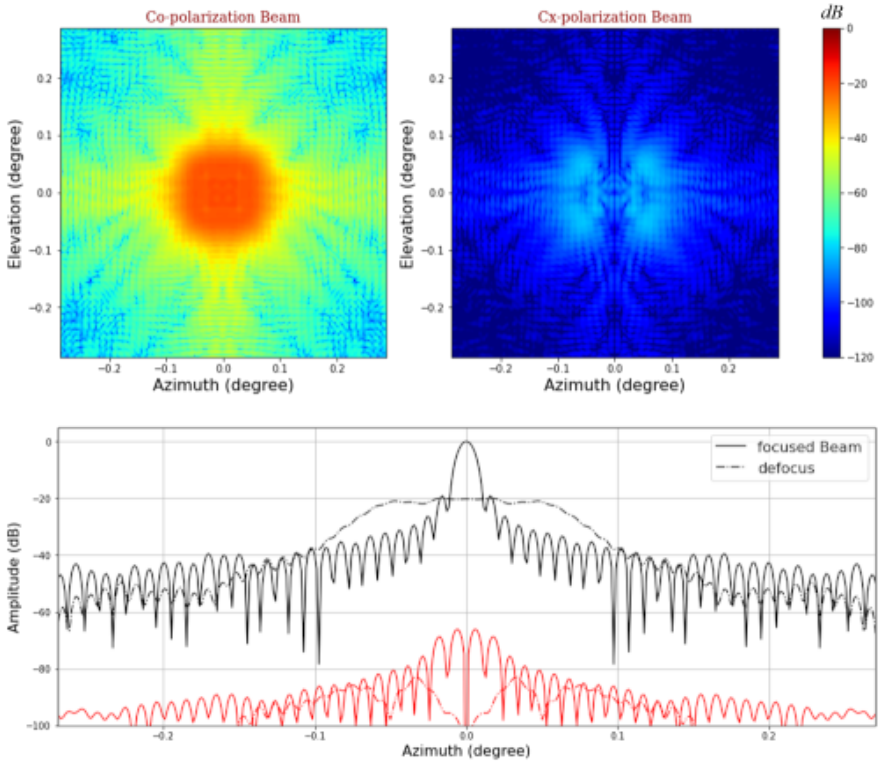

Figure 2.6.: The defocused beam patterns. The receiver is moved forward from the new focus by 105mm. The central beam is extended, gain of the beam is reduced by around 20dB.

Holographic measurement doesn't require the telescope's optics to be focused. On the contrary, it is better to defocus the optics and spread out the beam so that the required dynamic range of the measurement instrument, such as the digital back-end receiver, can be reduced. For the near-field FYST holographic system, we move the receiver 105mm forward from the focus, which is 600mm behind the nominal focus. Main beam is extended in angular range of $\pm 0.1°$. The gain of the main beam is reduced by 20dB. The defocused beam pattern and its cut plot compared with the focused beam are presented in figure 2.6.

2.2.3. Diffraction effect of panel edges

FYST is made of square panels. To avoid the issue caused by thermal expansion, these square panels are assembled with 1.2mm gap between them. The surface discontinuity results in that the induced surface currents close to the panel edges differ from the PO currents. The difference is concentrated in the boundary region only at a distance of the order of a wavelength. Therefore, we consider that the effect of the panel edges on the telescope's diffraction beam pattern could be neglected, if the operating wavelength is much shorter than the panel size.

The method called the physical theory of diffraction (PTD) [64][74] is a critical technique that addresses this problem. The method provides the additional current as a correction term for the PO solution to improve the accuracy. The PTD method used in the TICRA GRASP modeling software employs the algorithm developed by Johansen in paper [65]. The diffraction effect of the panel edges of the FYST telescope is studied by carrying out PO-only analysis and PO + PTD analysis separately. Their differences are the nonuniform part of the fields contributed by the diffraction effect of panel edges. The simulations are done at 100GHz (around 1/3rd of the holographic frequency) and 148GHz (half of the required frequency) because the PO analysis at a lower frequency is more efficient for the same telescope geometry. The effects at 296GHz, which is very time consuming, can be predicted by the results of these two lower frequencies. The simulations were done for the out-of-focus optics, where the receiver is 600mm behind its nominal focus, and the value of the beam peak is reduced by 20dB at 296GHz, and the input beam is linear polarization in the x direction. Figure 2.7 presents the diffraction fields produced by the panel edges. They are concentrated in the cross feature of the beam pattern and contribute to the total radiation beam with a ratio of -48dB at 100GHz and -52dB at 148GHz. If the operating frequency is turned to 296GHz, the contribution of the edge diffraction fields should go down to -58dB, assuming that the intensity of the edge diffraction fields is proportional to the operating wavelength. The maximum of the fields is -78dB below the peak of the focused beam, which is even much less than random noise in the beam measurement system. Therefore, we can ignore the panel edge effects in the holographic measurements. The case of the telescope reflectors illuminated by a y-polarized receiver beam is also simulated, we find that the edge diffraction patterns are similar for the x and y polarization but with opposite signs. This means that we could, in principle, cancel the edge diffraction effects by measuring two independent beam maps with different polarization signals and adding them up. The diffraction fields produced by the panel edges of FYST are shown in figure 2.7.

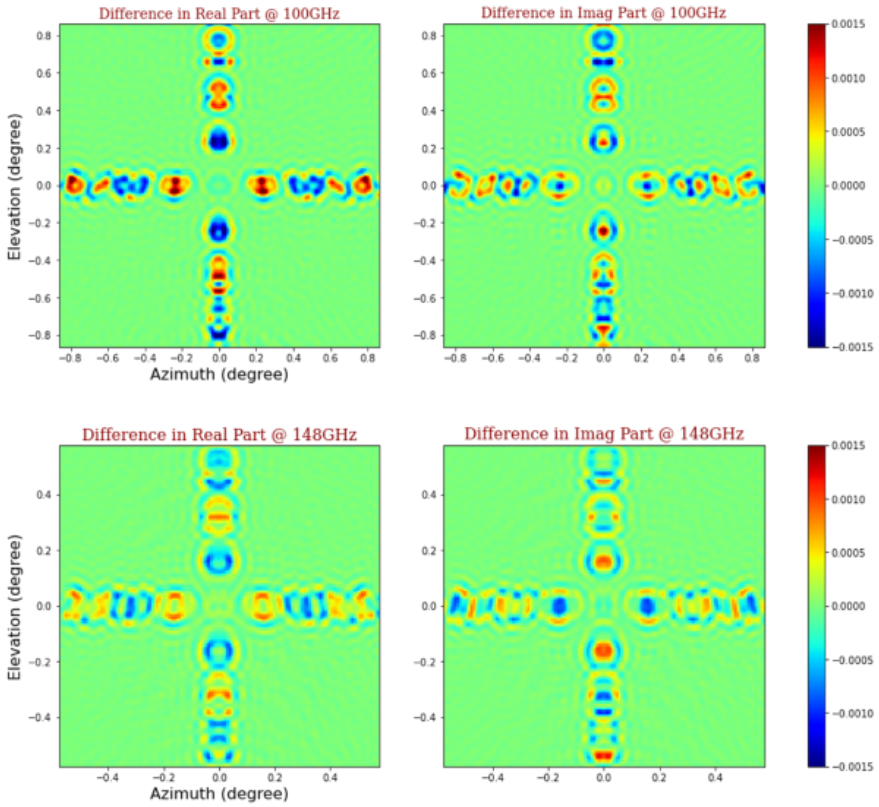

Figure 2.7.: Radiation pattern produced by the panel edges of the FYST telescope at 100GHz and 148GHz, respectively. The fields are calculated by taking the difference between the PO-only analysis and PO+PTD analysis results. The map size is around $1.72 \times 1.72 deg^2$ for the simulated fields at 100GHz and about $1.15 \times 1.15 deg^2$ for that of 148GHz. The simulated fields are normalized by the field of the map center.

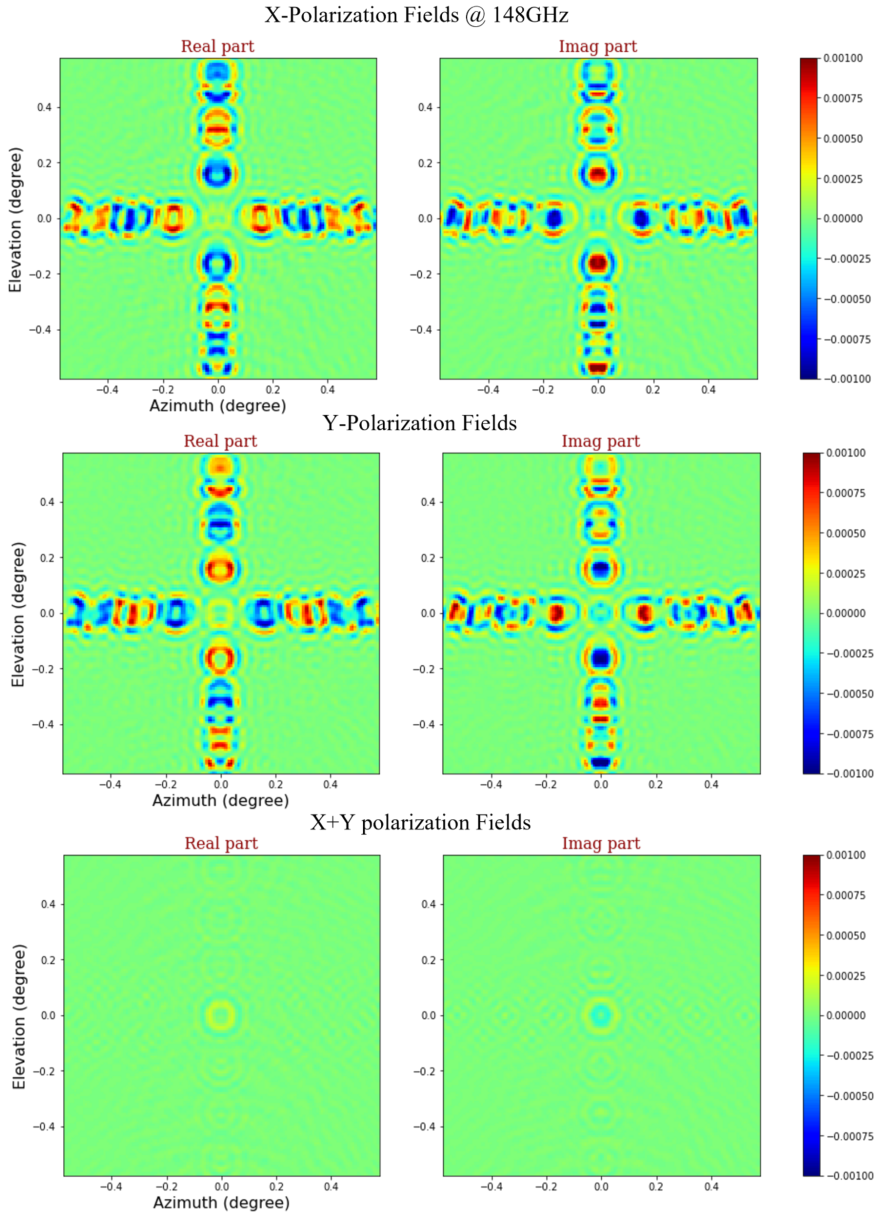

Figure 2.8.: Radiation pattern caused by panel edges at 148GHz. The top is the field with an x-polarized illumination beam; the Middle is the case with the y-polarized receiver illumination beam; the Bottom is the summation of the two polarized fields. The diffraction caused by panel edges can be eliminated by separately measuring the beam in two linear polarization cases.

2.3. 'Two-step' PO analysis Technique

The electromagnetic characteristics of the FYST telescope in the near field have been simulated and studied by the physical optics analysis. The method is accurate but very time-consuming. It is inconvenient for some applications that require fast beam prediction, for example, simulating the beam shape changes as the receiver is mounted at different positions in the focal plane and fitting the predicted beam with the observed beam for telescope surface diagnosis, which is called holography analysis described in chapter 4, and generally requires thousands of beam simulations. Thus it is of interest to develop a new method to speed up the PO analysis for FYST.

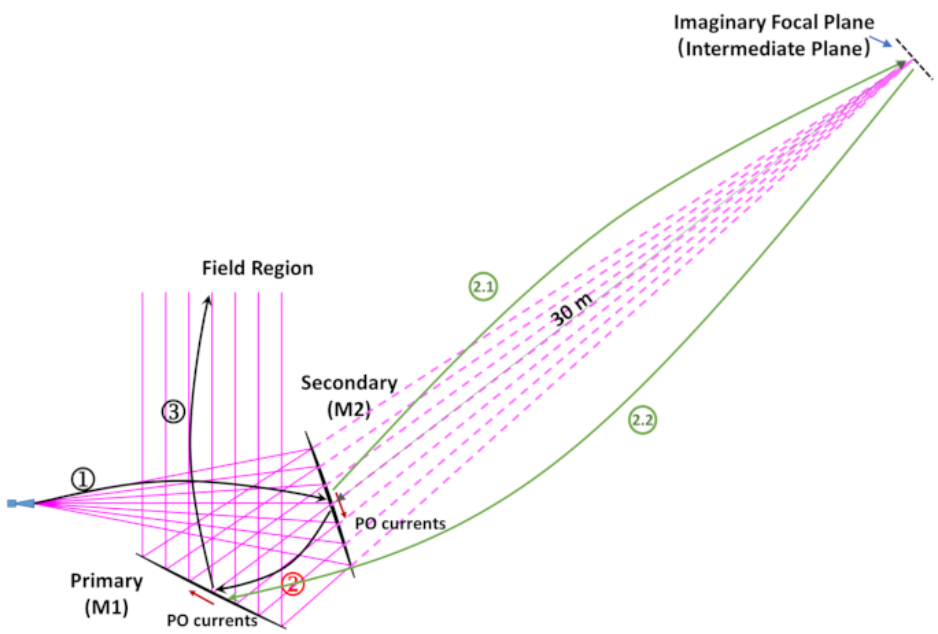

Figure 2.9.: The calculation flow of the physical optics analysis for the FYST telescope. Black arrows indicate the conventional PO analysis, and green arrows present the 'two-step' PO analysis processes. The calculation procedure by applying the 'two-step' PO method includes: 1) calculate fields in the M2 surface based on the illumination beam pattern of the receiver feed horn and convert the fields to induced PO currents; 2.1) Calculate the fields on intermediate focal plane by using PO integration, likewise calculate the equivalent PO current distributions on this plane by the fields; 2.2) Carry out PO analysis to calculate the fields in M1 and its induced PO currents; 3) Compute the fields in the region that we want to predict with the PO currents in M1.

The most time-costly step in the computation flow described in figure 2.4 is the integration of PO currents on the M2 surface to find the fields on M1 because the

two reflectors have similar size (∼6 meters) and are arranged too close, which implies that the phase varies rapidly in the current integration and a very fine sampling on M2 is required. Fortunately, we know that M2 forms two foci shown in figure 2.9; one is 12 meters in front of the mirror and occupied by the receiver feed, another is the image of the receiver feed at 30 meters behind the mirror and called the imaginary focal plane. The fields at the imaginary plane are confined to quite a small range. So, we can break down this costly computation into two steps: 1) Simulate the diffraction fields on the imaginary focal plane by PO analysis, then convert the computed imaginary fields to equivalent currents; 2) Calculate the desired fields in the M1 surface by taking the PO integration for these equivalent currents. The actual calculating procedure of modeling the FYST beam maps is illustrated in figure 2.9. This 'two-step' PO analysis can significantly reduce the computation time. For example, employing it to predict the FYST beam at 300GHz only requires around one hour for a computer with 12 Intel E5-2620 CPUs. The computing efficiency is improved by more than two orders of magnitude compared to the previous conventional PO analysis by GRASP software which took around one week using a machine with 100 CPUs). We also find that this method can make the simulations almost frequency independent.

This developed 'two-step' PO analysis technique uses the same idea, calculating a large mirror by two steps, as the technique presented by Bondo in paper [75][76], which was developed to model the quasi-optics mirror and len and has been successfully implemented to check the optics components of the Herschel SPIRE instrument[77]. Bondo named this technique A-PO analysis because the technique refers to the use of an Auxiliary plane or intermediate plane; here is the imaginary focal plane in figure 2.9. The basic clue of the method is to calculate the fields on an intermediate plane where the scattered fields of the mirror are concentrated in a limited spatial extension, leading to a fast convergence of the PO integral. Fields propagating from this intermediate plane to the target area are calculated by the equivalent PO currents on this ancillary plane. In this section, the method will be described in detail by applying it to speed up the FYST beam simulations. The accuracy of the technique is checked by comparing the simulated fields with the previous results from the GRASP package in section 2.2.

2.3.1. Fields on the Intermediate Plane

The key to the 'two-step' PO analysis is to properly choose an intermediate plane, and the fields on the plane scattered from a reflector can be computed very fast. In a reflecting optical system, an off-axis reflector is commonly used to focus or diverge a Gaussian beam from a feed horn to achieve the required beam size. Figure 2.10 shows the case where the beam is reflected and focused to a new plane, and the fields in this

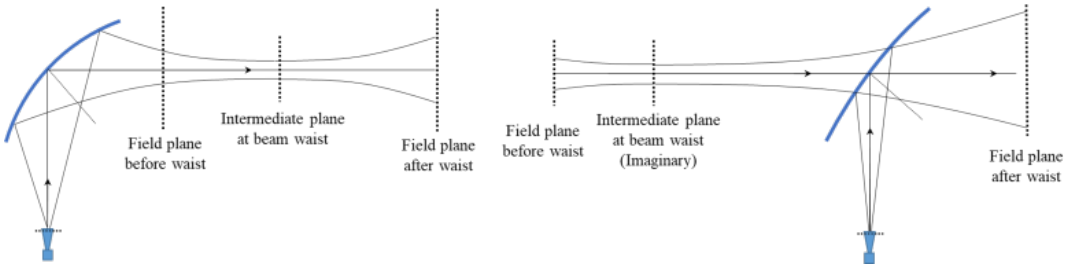

Figure 2.10.: Off-axis reflecting system where a feed horn produces a Gaussian beam scattered by elliptical or hyperbolic reflectors. The beam waist plane and the desired field plane after or before the beam waist plane are drawn. The beam waist of the reflected beam can be a real image in front of the reflector (left) or a virtual image behind the reflector (right).

plane are confined in a narrow region with a constant phase which is called the beam waist of the reflected beam. The beam waist can be an actual image in front of the reflector or a virtual plane behind the reflector. If the intermediate plane is placed at the beam waist, the scattered fields in this plane can be computed very fast because the fields contributed by each PO current element on the reflector have nearly identical phases. It means that the integrand in the PO integral is almost constant, so only a small number of PO current elements on the reflector must be sampled to compute the fields. The calculated fields in the beam waist plane are represented by equivalent PO currents used to predict the fields in the desired region. The fields in the beam waist plane are concentrated in the central beam region or within a few beam waist sizes. This can further speed up the calculations. Notably, the fields produced by fields in the intermediate plane are only exact if the intermediate plane is extended to infinite. Therefore, the accuracy and computation efficiency of the 'two-step' PO analysis is related to the size of the chosen intermediate plane. If there is such an intermediate plane where the fields are concentrated in a very small range, using the 'two-step' PO method can significantly improve the computation efficiency without degrading field accuracy that much.

For some cases, the beam waist is imaginary and located behind the reflector like a hyperbolic reflector shown in figure 2.10 (right). Directly applying the PO Integral formula 2.6 to predict the beam waist fields is incorrect. To predict the imaginary fields correctly, we need to back-propagate the reflector fields along the opposite direction of the reflected beam. The imaginary fields can be treated as a source area that radiates electromagnetic fields and produces the reflector surface fields. Therefore, instead of using the general retarded potential [11], the correct imaginary fields must be calculated using the advanced potential in the PO integral. The main difference between the retarded and advanced solution is that the exponential factor e^{-jkR} in formula 2.6 is replaced by e^{+jkR}, where R is the distance between the PO element in the reflector and

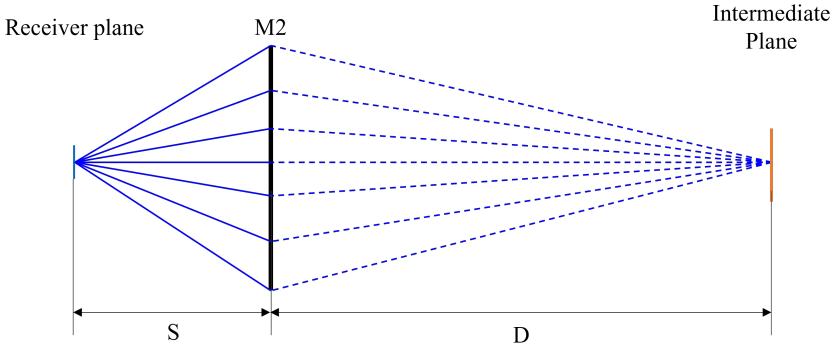

Figure 2.11.: The equivalent optics of the secondary mirror of the FYST telescope. S and D are the distance between M2, the receiver plane, and the receiver's image.

the target field point in the imaginary beam waist plane.

In the case of the FYST simulation, the intermediate plane is chosen as the imaginary focal plane of the secondary mirror shown in figure 2.9. The position of this plane can be found by using geometrical optics because the distance between the receiver and the secondary reflector is much larger than the confocal distance ($\pi w_0^2/\lambda$) [78] of the receiver horn, which means that the beam from the receiver can be considered as a point source with Gaussian amplitude profile. Although the shape of the FYST mirrors in the classical crossed-Dragone design has been modified to correct coma aberrations, the geometrical optics analysis indicates that the reflector's focus and local focal length remain similar to the original design. The optics of this reflector is equivalent to that described in figure 2.11. The geometrical relationship between the position of receiver (S), mirror local focal length (f), and position of imaginary focus (R) is expressed by following the formula 2.15. The local focal length of the M2 is 20 meters. We choose the intermediate plane to be perpendicular to the central ray.

$$\frac{1}{S} - \frac{1}{R} = \frac{1}{f} \tag{2.15}$$

Considering the configuration of near-field beam measurement described in section 2.2, the receiver is moved to 12.705 meters behind the M2 to refocus the telescope beam into the source 300 meters away from the telescope aperture. Then the intermediate plane is shifted around 4.8 meters further from M2. For the near-field optical setup, the beam size in this plane is about 6mm ($R \cdot \lambda/D$) at the wavelength of 1mm (300GHz). The computed field region is $750 \times 750\text{mm}^2$, around 125 beam size in each direction. This size is large enough to capture all relevant information for calculating the fields in M1. To avoid the aliasing errors in the generated intermediate fields, we sample the currents on M2 by $\sim 144 \times 144$ points with a sampling space of around 44mm. The calculated

intermediate fields in the co-polarization and cross-polarization are presented in figure 2.12. The fields are confined in the plane's center, and the cross-polarization beam is more than 30dB lower than the co-polarization beam. If ignoring the cross-polarization performance of the telescope, we can further simplify the computation by using the scalar Kirchhoff diffraction theory (section 2.4). Finally, the fields on the plane are meshed by 151 × 151 grids; the sampling spacing is about 0.8 times the beam size. In modeling the electromagnetic performance in different frequencies, the required region of the intermediate plane just needs to be enlarged or shrunk according to its beam size. This makes the 'two-step' PO technique is almost frequency-independent.

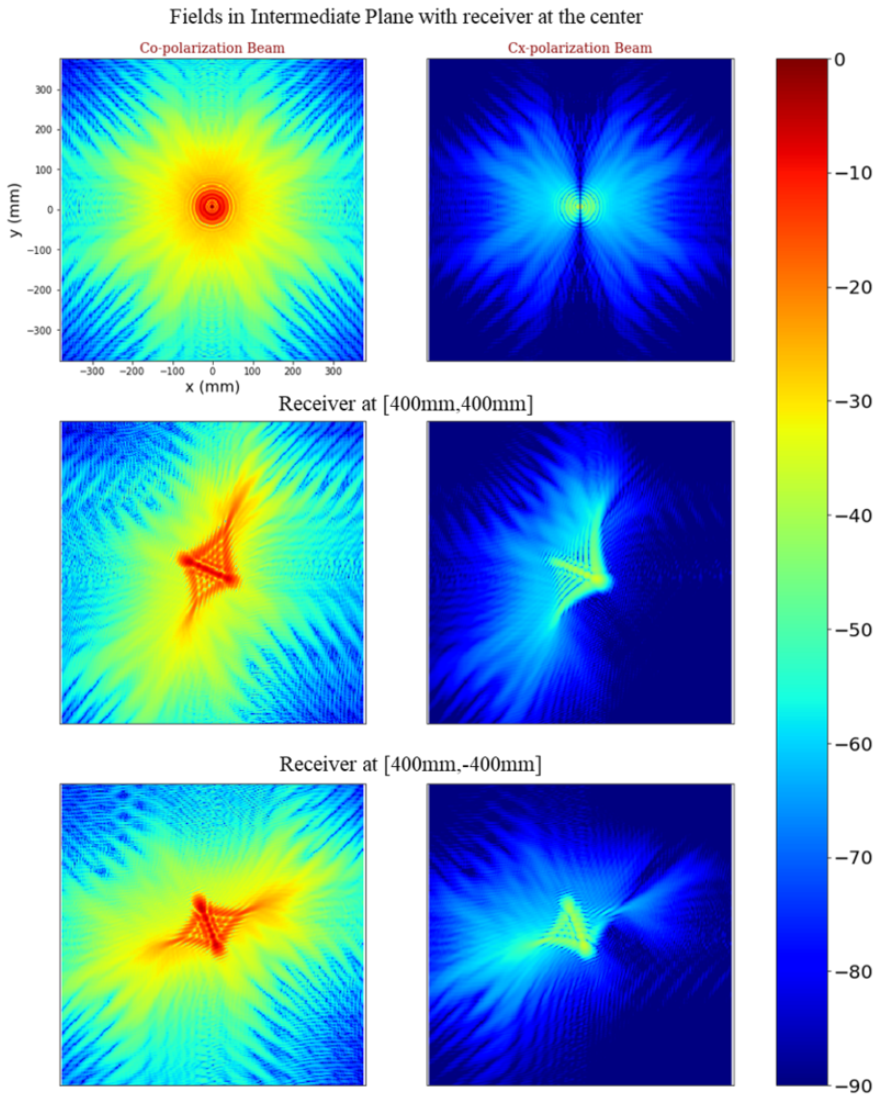

Figure 2.12.: The computed co-polarization and cross-polarization beams in the intermediate plane. The top is the case with the receiver in the center of the focal plane; the Middle and bottom are beams with the receivers at points of (400mm,400mm) and (400mm,-400mm).

In addition to the cases shown in figure 2.10 where the beam waist after reflection is at a finite distance from the reflector, the special case is that the reflected beam is focused in the distant region, which means the optimal position of the intermediate plane is in the far field. The far-field fields can be treated as an expansion of the fields on the reflector in a set of plane waves from different directions, which is called the plane wave spectrum of the fields in reflector. Considering the time-reversing case, the near fields on the desired surface are calculated as the combination of the set of plane waves described by the far fields that are expressed by the following formula,

$$\mathbf{E}_{near}(\mathbf{r}) \propto \int_0^\infty \int_0^\infty \mathbf{f}(k_x, k_y) \cdot e^{-j\mathbf{k}\cdot\mathbf{r}} \cdot dk_x dk_y \tag{2.16}$$

where $\mathbf{k}$ is wave vector and $\mathbf{f}(k_x, k_y)$ is the complex far-field plane wave spectrum.

2.3.2. Equivalent Currents

When the field distribution on the intermediate plane is generated, we replace the fields with a set of equivalent surface currents as the radiation source to predict the fields in M1. The field equivalence principle[70] indicates that the field outside or inside a closed surface can be deduced by a set of virtual electric and magnetic currents at the surface. These currents are chosen to satisfy the proper boundary conditions of the electromagnetic field. Here, the closed surface is the infinite intermediate plane; assuming a null field behind this plane, the equivalent electric currents $\mathbf{J}_e$ and magnetic currents $\mathbf{J}_m$ on the plane are expressed by following:

$$\mathbf{J}_e = \hat{n} \times \mathbf{H}_i \tag{2.17a}$$

$$\mathbf{J}_m = -\hat{n} \times \mathbf{E}_i \tag{2.17b}$$

where $\mathbf{E}_i$ and $\mathbf{H}_i$ are the calculated incident fields on the intermediate plane and $\hat{n}$ is the normal vector of the plane pointing from the plane to M2 in figure 2.9. The scattered fields in the region from this plane to the reflectors can be exactly represented by the PO currents integral if the plane has an infinite spatial extension. The equivalent currents radiate a zero field behind this plane. The PO integration, in this form of the equivalence principle, includes the electric current integral expressed by formula 2.6 and also the magnetic current integral, which is represented by the following formulas:

$$\mathbf{E}(\vec{r}) = -\frac{1}{4\pi} \int\int \mathbf{J}_m \times \hat{\mathbf{R}} \frac{1}{k^2R^2}(1 + jkR)e^{-jkR}k^2 ds' \tag{2.18a}$$

$$\mathbf{H}(\vec{r}) = \frac{1}{4\pi}\sqrt{\frac{\epsilon}{\mu}} \int\int_{S'} \Big(\mathbf{J}_m(-\frac{j}{kR} - \frac{1}{k^2R^2} + \frac{j}{k^3R^3}) \tag{2.18b}$$

$$+ (\mathbf{J}_m \cdot \hat{\mathbf{R}})\hat{\mathbf{R}}(\frac{j}{kR} + \frac{3}{k^2R^2} - \frac{3j}{k^3R^3})\Big)e^{-jkR}k^2ds',$$

The symbols in the formula are the same as those described in formula 2.6.

Two variations of this field equivalence principle can further simplify the calculations. Since we assume a null field behind the intermediate plane, we can place an infinite perfectly conducting surface in the plane. Then the electric current in formula 2.17a is short-circuited. Thus the scattered fields can be computed by the magnetic currents on an infinite perfect conductor. The equivalent magnetic current can be obtained using the Image Principle, which is twice the current calculated in formula 2.17b. In the same way, if we place a perfect magnetic conductor in the intermediate plane, the magnetic currents on the surface must vanish. The scattered fields are found from the electric current on the magnetic conductor. In the region behind the intermediate plane, these currents radiate the mirrored field in front of this plane.

2.3.3. Accuracy

When the fields on the M1 surface are predicted, the beam map in the near or far field is continuously calculated following steps 2 and 3 in figure 2.9. The computation time and accuracy of the fields simulated by the 'two-step' PO are investigated by comparing to the results of the PO analysis from the GRASP software. The near-field beam maps, which is 300 meters away from the telescope's aperture, are simulated by the 'two-step' PO technique for the focused and defocused setups. Figure 2.13 and 2.14 show the co-polarization and cross-polarization beams in the symmetrical plane at 300GHz. The beams are normalized by the peak value of the focused beam. If we treat the beam from the full PO analysis presented in section 2.2 as the standard gold reference, the errors of the 'two-step' PO are shown in figure 2.15. It can bee seen that the maximum error of the co-polarization beam is down to 65dB below the peak value of the focused beam. The cross-like error patterns is caused by the panel edge diffraction simulated by using the PTD analysis in the results from the full PO analysis. The field errors in the map center is caused by the inconsistencies in the definition of the input Huygens Gaussian beam, but the difference is very small.

The required computation time as a function of the operating frequency is also studied. The beam maps of the telescope are simulated at frequencies of 1500GHz, 296GHz, 148GHz, and 100GHz. It indicates the method is almost frequency-independent for the similar field accuracy and only takes around one hour for modelling the FYST telescope. Consequently, the properties of fast convergence, frequency-Independence and good

accuracy of the 'two-step' technique make this technique to be an excellent alternative algorithm for the full PO analysis.

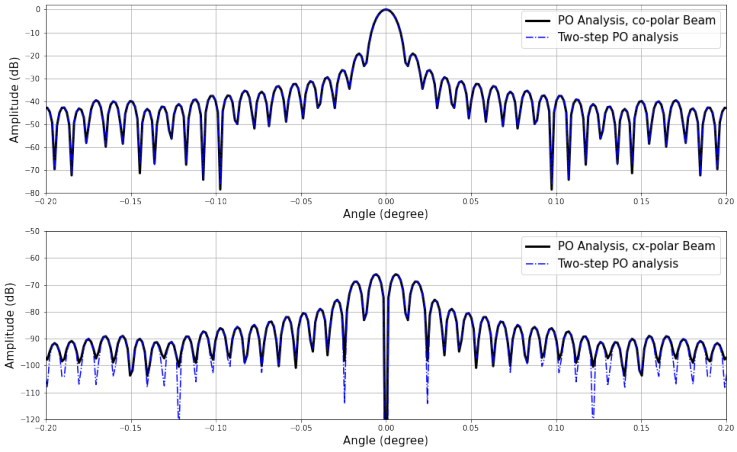

Figure 2.13.: Comparison of the focused beam of the FYST telescope simulated by PO analysis and two-step PO method. The field region is 300 meters away from telescope aperture. Top is the co-polarization beam and bottom is the cross-polarization beam.

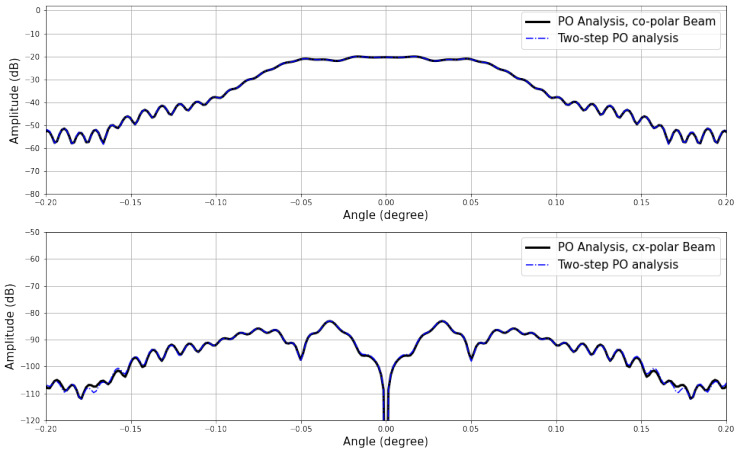

Figure 2.14.: Comparison of the defocused beams simulated by PO analysis and two-step PO method respectively. The field region is the same with the focused case. The beam is spread out by moving the receiver 105mm forward from the system focus. The co-polarization (top) and cross-polarization (bottom) beams are plotted.

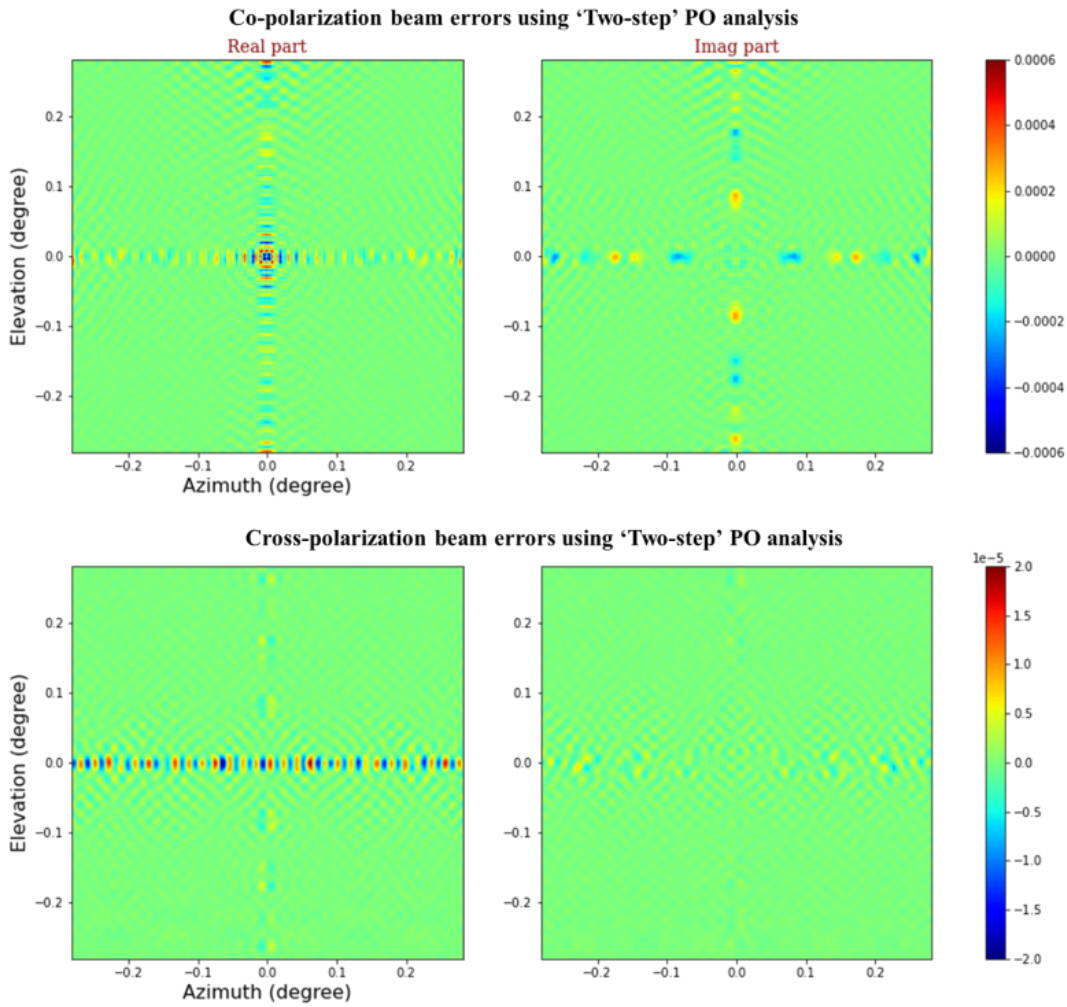

Figure 2.15.: The difference patterns between the simulated fields calculated by using the PO analysis and two-step PO analysis. The telescope is illuminated by a x-polarized Gaussian beam from the receiver horn. Top is the error patterns of the co-polarization beam in real and imaginary components. Bottom is the error map of the fields in another polarization. All the fields are normalized by the co-polarization beam peak value.

2.4. 'Two-step' Fresnel-Kirchhoff Analysis

Employing the two-step PO analysis has significantly improved the radiation beam simulations for FYST without notable accuracy degradation. Meanwhile, all electric performances of the telescope, including co-polarization and cross-polarization fields, are preserved and predicted. It has been proven that the 'coma-corrected' FYST telescope still has excellent cross-polarization isolation, which is more than 65dB lower than the peak value of the focused co-polarization beam. To further speed up the PO simulations for FYST, we will neglect the cross-polarization effects and treat the fields as scalars. The scalar Kirchhoff's diffraction theory [11][79][80] gives the field solutions of the scalar Helmholtz wave equation in homogeneous space with given boundary conditions. The Fresnel-Kirchhoff diffraction formula is the solution for the case where the field is scattered by an aperture surface shown in Figure 2.16, which is expressed by

$$U(P) = -\frac{j}{2\lambda}\int\int_S \frac{A \cdot e^{-jk(r+s)}}{rs}[cos(n,r) + cos(n,s)]ds, \tag{2.19}$$

where U is the space-dependent part of the studied monochromatic scalar wave $V(x,y,z,t) = U(x,y,z)e^{-j\omega t}$, and the trigonometric terms, $cos(n,r)$ and $cos(n,s)$, are the cosine of the angle between normal vector on the reflector and incoming and outgoing rays, r and s are the distance between reflection point Q and the source and target field point. The Amplitude A in the original formula in chapter 8 of the book [11] is a constant and represents a source radiating equally in all directions, here we should allow the illumination pattern function from the source, for example, the Gaussian radiation pattern from feed horn. This formula presents the field U at point P produced by a source with amplitude of A at P_0, which has been diffracted by an aperture at surface S.

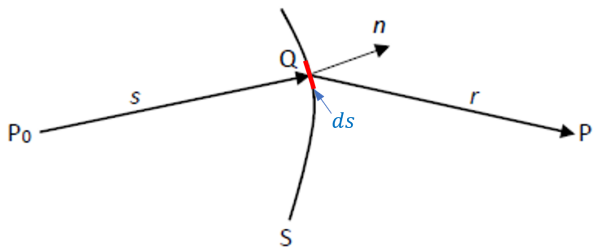

Figure 2.16.: Illustrating the diffraction formula 2.19.

Applying the scalar diffraction theory to deal with the case where the surface is a reflector does not need real modification on this formula. Strictly, there is a phase reversal on reflection, but that can be represented by a multiplication factor $e^{j\pi}$. The

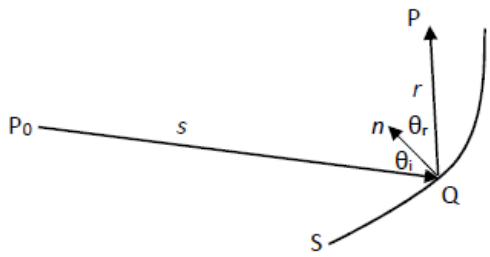

Figure 2.17.: Diagram of the field diffraction by a reflector.

diagram of the field scattered by a reflector now looks like Figure 2.17. We rewrite the cosine terms in formula 2.19 as $[cos\theta_i + cos\theta_r]$ where θ_i and θ_r are the angles between the incoming and outgoing rays and the normal vector on the reflector. Following the two-step analysis flow described in Figure 2.9 and replacing the vector PO current surface integration by simple scalar field integral, processes of the two-step Kirchhoff analysis are summarized as follows:

1. Calculate the field at M2 produced by the illumination from the feed horn.
2. Calculate the field on the intermediate focal plane, the imaginary focal plane in Figure 2.9, produced by the fields on M2.
3. Calculate the field on M1 produced by the fields on the intermediate plane.
4. Calculate the field at the region we want to study, produced by the fields on M1.

Step 2 of the field calculation on the intermediate plane is still critical to speed up the field integration. The way of choosing the intermediate plane and sampling issues explained in section 2.3.1 is still adaptable. Meanwhile, the field propagation in the back side of the reflector, for example, M2 in FYST seen Figure 2.18, needs to use the 'advanced values' e^{+jkr}. The virtual field on the intermediate plane is computed by the following:

$$U(P) = -\frac{j}{2\lambda}\int\int_S \frac{A \cdot e^{-jk(s-r)}}{rs}[cos\theta_i + cos\theta_r]ds. \tag{2.20}$$

Since the intermediate plane is chosen to be perpendicular to the central ray and the field in the plane is confined in the area of around $750mm \times 750mm$ at 300GHz, the value of trigonometric terms approximately can be replaced by 2 for the calculation of field on M1 from the field on the intermediate plane. Using the two-step Fresnel-Kirchhoff method for the beam pattern prediction of FYST gives the same level of field accuracy in the co-polarization beam simulations. The required computing time for simulating

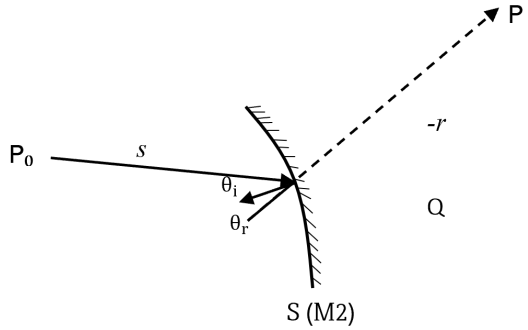

Figure 2.18.: Diagram of the virtual diffraction field on the intermediate plane behind a mirror.

the 300GHz near-field beam map of the FYST model in this way is now down to only about 1 minute using a private computer with an Intel i7-10700 CPU and 8GHz RAM. Compared to the results from the GRASP computation, the difference is 68dB down related to the peak value of the beam. This new technique will be used to build a new algorithm for the FYST holographic analysis described in the coming chapter 4.

2.5. Summary

In this chapter, two precise and efficient methods for simulating the optical characteristics of the FYST telescope have been studied and presented. The study began with an explanation of the principle of the physical optics approximation technique for analyzing reflector antennas. The physical optics analysis was used to study the far-field radiation performance of a simple parabolic reflector. Then the Fourier transform relationship in the antenna's radiation was deduced. This relationship is the guidance theory of the microwave holography technology. Next, the near-field FYST beam was simulated using the PO method, which took around a week for one beam simulation due to the two close reflectors. After the PO analysis, the diffraction effects of the panel edges of FYST on its near-field beam pattern were studied by the physical theory of the diffraction method. The simulation indicates that the panel edge effects can be neglected at 300GHz because the effect is 78dB below the peak value of the FYST's focused beam. Finally, in order to speed up the beam simulations for FYST, a new 'Two-step' PO analysis technique and 'Two-step' Fresnel-Kirchhoff diffraction method were developed to speed up the beam simulations for the special Crossed-Dragone FYST telescope. The computational time has been reduced by four orders of magnitude without notable accuracy degradation. The two advanced methods can be used to speed up the simulations for general two-reflector optics.

Chapter 3.

Microwave Holography Technology

This chapter is dedicated to the principle of microwave holography technology and the primary holographic design for the reflector surface diagnosis of the FYST telescope. The discussion begins with an explanation of the microwave holography fundamentals using the far-field radiation theory of reflecting antenna. The criterion of designing a holographic system is interpreted to meet the required surface accuracy and spatial resolution. Next, the microwave holography measurement in near field is explained. Finally, this .

3.1. Fundamentals of Microwave Holography

The electromagnetic characteristics of a large reflecting antenna have been studied in the preceding chapter by the physical optics analysis. The scattered fields of a reflecting antenna can be predicted in far or near field (Fraunhofer region or Fresnel region) if knowing the antenna's geometry and the fields illuminated on its surface. Here, the illumination fields are the beam pattern of the antenna's receiver feed horn. Naturally, we can think of using the inverse process, inferring the antenna's geometry by observing its scattered fields with assuming the beam pattern of the receiver is known both in amplitude and phase. The far-field radiation theory of a reflecting antenna indicates that the Fourier transform relationship exists between the far-field radiation pattern ($E_{far}(u, v)$) of the antenna and its surface induced current's projection ($\widetilde{\mathbf{J}}(x, y)$) on aperture plane [15][81]. The details of the radiation theory have been explained in Chapter 2. Here, we rewrite the radiation formula by the equation 3.1 and neglect the constant factor. In this expression, x and y are coordinates of the points on the

aperture, and u, v are the antenna pointing directions.

$$E_{far}(u,v) = \int \widetilde{\mathbf{J}}(x,y) \cdot e^{-jk\cdot(ux+vy)}\ dxdy; \tag{3.1}$$
$$u = cos(\theta)sin(\phi),\ v = sin(\theta)cos(\phi).$$

The reversible Fourier Transform relationship offers elegant theoretical support for solving the antenna's shape by measuring its far-field radiation fields both in amplitude and phase with microwave receivers.

The principle of holography is illustrated in Figure 3.1 for a simple symmetrical parabolic antenna on the left. The field distribution on its aperture can be computed in amplitude and phase by taking an inverse Fourier transform to the observed complex radiation fields of the antenna; see the blue curves in Figure 3.1b. The ideal parabolic antenna produces a constant phase distribution on this aperture. The phase changes $\Delta\phi(x,y)$ of the measured aperture fields are calculated by the formula 3.2a, where $\mathbf{E}_{meas}$ is the observed antenna beam, and $\mathbf{E}_{ideal}$ are simulated ideal complex beam. Then the measured phase changes can be converted to the surface deviations of the antenna reflector by optical ray tracing shown in Figure 3.1a and the operating wavelength λ. This is expressed by equation 3.2b, where ξ is the reflection angle at the reflection point.

$$\Delta\phi(x,y) = phase(\mathscr{F}^{-1}[\mathbf{E}_{meas}]) - phase(\mathscr{F}^{-1}[\mathbf{E}_{ideal}]) \tag{3.2a}$$
$$\epsilon(x,y) = \frac{\Delta\phi(x,y)\lambda}{4\pi cos\ \xi} \tag{3.2b}$$

Hence, the critical step is to accurately measure the far-field radiation beam of the antenna under test. The principle of reciprocity in antenna theory [15][69] indicates that the transmission field pattern and reception pattern of an antenna are equivalent. It is convenient to measure the antenna's reception beam pattern using microwave receivers instead of the radiation beam pattern. The schematic of holographic analysis is summarized in Figure 3.2. We let the antenna keep observing a distant point source. The antenna's reception pattern can be recorded by taking the response of its focal receiver and scanning the antenna in azimuth and elevation coordinates. However, the instability of the terrestrial atmosphere between the point source and antenna messes up the phase measured by the receiver. Therefore, an extra antenna is used for looking at the source in its bore-sight to provide a phase reference. Since the two antennas look through the same atmosphere layers, the effect of atmospheric instability on the signal phase can be canceled by taking the phase difference between the two antennas.

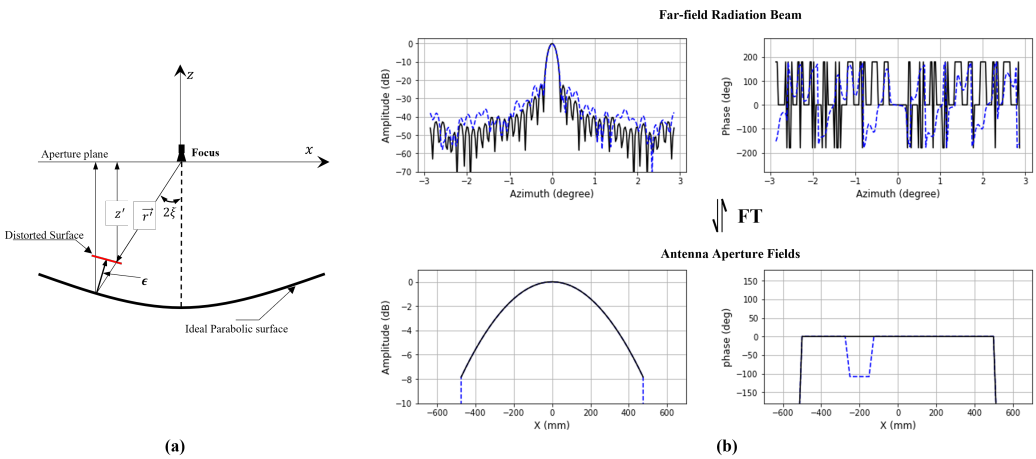

Figure 3.1.: Principle of the microwave holography technique. **a)**: Enlarged surface distortion on a simple parabolic reflector with feed horn located in its focus; **b)**: The simulated far-field radiation beam (top) and aperture field (bottom) for the case of the antenna with an ideal surface (black curve) and distorted surface (blue). The complex far-field beam and aperture field are a Fourier transform pair.

Hereinafter, the second antenna is called a reference antenna. The receivers in the two antennas are locked by sharing the same local oscillator (LO). The outputs from the two antennas are sampled and fed into a cross-correlator. Their phase differences are collected and recorded as the measured phase pattern of the antenna under test. The main receiver of the antenna under test records the amplitude pattern. After the complex beam measurement, the collected data needs to be calibrated to remove the electronic drift of the measurement system, for example, the gain fluctuation of the receivers and slow phase changes between the light path of the two antennas. Next, the recorded fields are interpolated into regular rectangular grids with the required resolution for the subsequent Fourier Transformation. The aperture fields are computed applying the fast Fourier transformation (FFT) algorithm. Then the surface deviations of the antenna are inferred from the aperture phase error distributions, finally, converted to the corrections of the antenna's adjusters.

The advantage of employing the holography technique is that it directly measures and assesses the antenna's electromagnetic performance, which is the main concerned feature of the designed antenna. After one circle of the antenna surface measurement and correction, the second beam pattern measurement can help check the previous measurement's correctness. This method can use the advanced receiver system of the antenna. It means the holographic measurement can be carried out during the antenna operation so that the effect of different operating conditions on the antenna's surface deformations, such as the antenna deformation produced by gravity at different elevations, can be explored. This technique also can achieve very high measuring

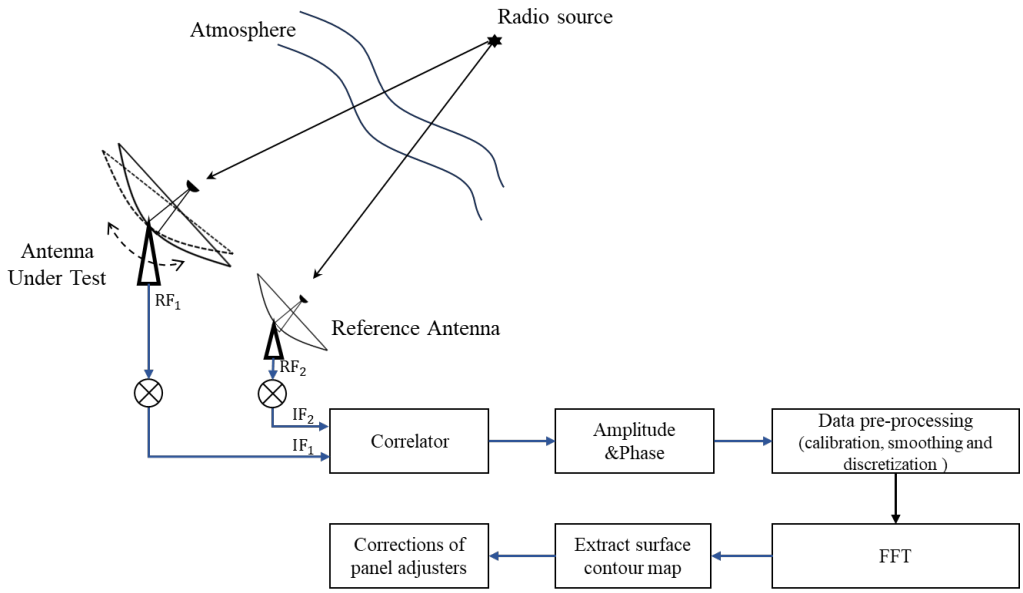

Figure 3.2.: Diagram of the microwave holography measurement.

accuracy by improving the signal-to-noise ratio of the beam measurement system. For example, the 100-m Green Bank Telescope (GBT) holography measurement aligned the reflector with an accuracy of $< 250\mu m$ by measuring its beam with a signal-to-noise ratio of ~ 73dB at 12GHz [82]. The details of designing a holographic system, which can measure the surface error map that meets the required accuracy and spatial resolution, are demonstrated in the rest of this section based on the most fundamental Fourier transform theory.

3.1.1. Spatial Resolution

A large radio telescope generally is segmented into a set of small panels. These panels are placed on a back structure where they are supported by three or more adjusters. The antenna surface error map measured by the holography system must have enough spatial resolution and accuracy so that we can determine the movement values of the adjusters to compensate for these panel errors and achieve the required surface precision. The spatial resolution of the aperture field function is determined by the measured angular size of the beam pattern.

Considering the case that the beam pattern is sampled by $N \times N$ points in square grid, based on Nyquist sampling theorem, the separation between two adjacent sampling points must be less than beam size of the antenna, so that the entire aperture fields can

be determined without aliasing error. The sampling interval Δ is expressed as below

$$\Delta = \frac{K\lambda}{D} \tag{3.3}$$

where D is the diameter of the antenna aperture, and K is a constant less than one. Then we record the beam pattern in angular size of $\mathrm{N} \cdot \frac{\mathrm{K}\lambda}{\mathrm{D}}$. This can be treated as the multiplication of the practical antenna beam and a rectangular function from $\frac{\mathrm{N}}{2}\frac{\mathrm{K}\lambda}{\mathrm{D}}$ to $\frac{-\mathrm{N}}{2}\frac{\mathrm{K}\lambda}{\mathrm{D}}$. Based on convolution theorem, applying the inverse Fourier transform to the recorded data gives the convolution of the real aperture fields with a sinc function which is the Fourier transform of the rectangular function. The sinc function is represented in equation 3.4.

$$\frac{sin(\pi N K \lambda x/D)}{\pi N K \lambda x/D} \tag{3.4}$$

That is illustrated in Figure 3.3. The spatial resolution of the measured aperture phase is defined by half width δ of the sinc function (equation 3.5).

$$\delta = \frac{D}{KN} \tag{3.5}$$

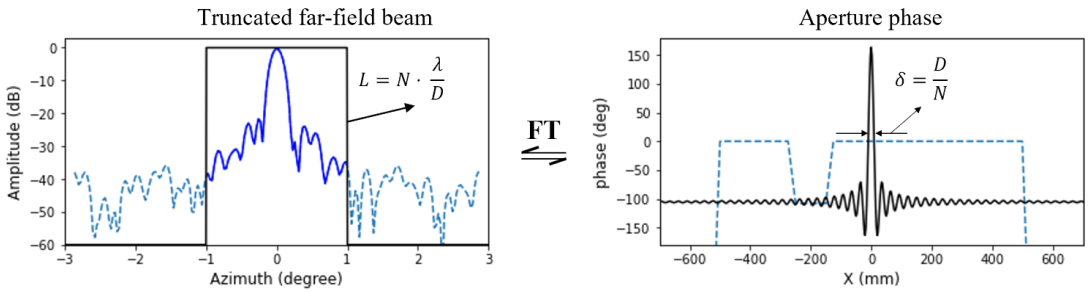

Figure 3.3.: Fourier transform relationship between a rectangular window function in angular domain and a sinc function in aperture spatial plane (black curves). The practical far-field beam (dash curve) is truncated by a rectangular window function to be the measured beam (blue) for holography analysis. The computed aperture field is the convolution of the real aperture field and the sinc function with size of $\delta = D/N$.

Therefore, when we know the spatial resolution δ required to describe the antenna's panel errors, the holographic beam is sampled in an angular range of $\theta = \frac{\lambda}{\delta}$ with the sampling interval of Δ. For the case of measuring the surface deformations for the 6m diameter FYST telescope, if the holographic system operates at wavelength of $\sim$ 1mm (300GHz) the telescope's beam needs to be measured in a 0.6° field with 0.01° sampling interval.

3.1.2. Measurement Accuracy

The accuracy $\Delta\epsilon$ of the measured antenna surface is related to the signal-to-noise ratio of the measured aperture fields denoted by SNR(Aperture). If neglecting the reflection angle ξ shown in Figure 3.1, the surface accuracy of the measurement is defined by

$$\Delta\epsilon = \frac{\lambda}{4\pi SNR(Aperture)}. \tag{3.6}$$

For simplicity, we assume the receiver illuminates the antenna uniformly, so the aperture field points have the same SNR value. The Fourier transform relationship between the antenna's radiation fields and aperture fields indicates their noise relationship by the formula

$$SNR(Aperture) = \frac{SNR(O)}{N}, \tag{3.7}$$

where SNR(O) is the signal-to-noise ratio of measuring the beam on boresight, called peak signal-to-noise ratio (p-SNR). Substituting this formula to equation 3.6 and replacing the sample point number N by D/Kδ give the equation 3.8 that relates the SNR of the beam measurement system to required surface accuracy and spatial resolution.

$$\Delta\epsilon = \frac{\lambda D}{4\pi K\delta\ SNR(O)} \tag{3.8}$$

Therefore, to achieve high surface accuracy, the beam measurement system must be sensitive enough to measure the antenna's distorted beam or uses a high operating frequency. For example, the 12m VertexRSI ALMA antenna carried out the holography analysis at a frequency of 78.92 or 104.02 GHz and obtained the measurement accuracy of $\sim$ 5µm [59]. For the 6-m FYST telescope, if the operating frequency is 300GHz and the sampling interval is about 0.8 beam size, the SNR of the observed fields has to be better than 70dB to achieve $<$ 2µm measuring accuracy and 10cm spatial resolution.

The complex fields of the antenna are measured by taking the cross-correlation of the output of the two receivers, the receiver on the tested antenna, and the reference antenna. The equivalent SNR of the cross-corrector receiver is expressed by the following equation

$$\frac{1}{SNR_E^2} = \frac{1}{SNR_1^2} + \frac{1}{SNR_2^2} + \frac{1}{SNR_1^2 \cdot SNR_2^2}, \tag{3.9}$$

where SNR_1 and SNR_2 are the signal-to-noise ratio of the antenna under test and reference antenna, Figure 3.4 shows the output SNR as a function of SNR_1 if fixing the SNR of the reference antenna. It is found that the noise of the recorded complex field

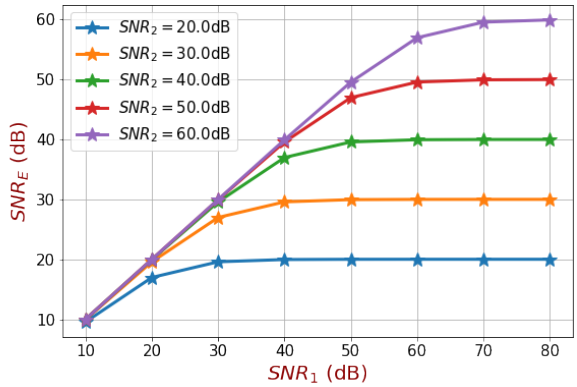

Figure 3.4.: Signal to noise ratio of cross-correlation receiver as a function of the SNR of the output of under test antenna for the cases with fixing receiver SNR to be 20, 30, 40, 50, 60dB.

points is limited by the lowest signal-to-noise ratio of the two receivers. Normally, a small antenna is used as the reference antenna and offers much less gain than the large tested antenna. The holographic setup, such as the signal source selection, integration time, and antenna scanning speed of the beam measurement, strongly depends on the noise performance of the reference antenna.

3.1.3. Far-field Holography Measurement

The holographic method described above requires to observe the antenna's complex beam in far field. The far-field region of an antenna [83] is defined by a distance that is larger than

$$R_{far} = \frac{2D^2}{\lambda}, \tag{3.10}$$

where D is the diameter of the antenna. The distance R_{far} is also called Fraunhofer distance which can easily reach a value of several hundred kilometers for a 10m diameter telescope. For example, in the 300GHz FYST holographic system, its Fraunhofer distance is about 72km. The point-like source has to be placed beyond this distance, then the Fourier transform relationship starts to be valid, and the simple FFT algorithm can be used for the data analysis. Celestial sources become attractive choices. These sources can also provide a range of elevation angles and allow the study of the antenna deformations caused by gravity. The first far-field holography experiment was made by Scott and Ryle for the Cambridge 5km radio telescope array [21][20] to observe the source of 3C84 which is compact at 15.4GHz. Four of the eight dishes were simultaneously measured by using the rest four telescopes as the reference antennas, and each field point

was observed or 1min to get the SNR of ~ 250 (48dB) and achieve 100µm accuracy. Another astronomical source is the water-vapor maser at $\sim$ 22GHz in Orion Nebula [84]. The 30-m IRAM telescope used this water-vapor maser as a signal source, and a 1.75m antenna mounted parallel to the optical axis of the IRAM telescope was used as a phase reference antenna. The beam was measured at 32×32 points by taking around 20 hours telescope time. This measurement achieved an effective surface accuracy of 65µm with 10µm uncertainty [85]. Other option is to use the available satellite beacons. for example, the Lincoln Experimental Satellite (LES-8), at a frequency of around 38GHz, has been used for the holographic analysis of the NRAO 12-m radio telescope and the Heinrich Hertz Telescope [86][87].

Using celestial sources to measure the groud-base antenna cannot avoid the influence of terrestrial atmosphere [88]. The variations in the atmospheric water vapor column density lead to signal path changes from the source to the antenna. Fortunately, the path changes can mainly be compensated by using a reference antenna mounted close to the beam axis of the antenna under test. The two antennas almost look through the same atmosphere. However, the atmospheric turbulence [89] still creates the path difference between the two antennas, which can degrade the accuracy of the holographic measurement.

3.2. Near-field Holography Measurement

If there is no sufficiently strong celestial source to satisfy the required operating frequency and surface accuracy, we have to use an artificial source and put the source from several hundred meters to a few kilometers away from the antenna under test. In practice, the distance is much shorter than the antenna's Fraunhofer distance. The holographic beam needs to be measured in the near field. The short distance can improve the signal arriving at the antenna, so that a sufficient high SNR of the measured fields can be obtained. It also reduces the atmospheric volumes that the signal passes through and minimizes atmospheric variations. Usually, artificial sources are mounted on a steel tower on the ground or mountain site with an elevation angle of $< 10°$. The gravitational deformation of the antenna for different elevation angles cannot be studied.

Since the source is close to the antenna, the phase front of the incoming wave front from the source is not a plane and will contain higher orders phase terms over the antenna aperture plane. We cannot directly apply the inverse Fourier transform to the measured beam map until these high-order terms are corrected. For example, one high-order term is the spherical wave front caused by the finite distance, which behaves the same way as defocus error. This error can be compensated by an axial

displacement of the antenna's receiver. The details of the corrections of these high-order phase terms are demonstrated by Jacob W. M. Baar for the near-field holography of the ALMA telescopes [59][16]. Successful near-field holography measurements using the Earth-bound transmitters have been reported for the Texas 4.9-m millimeter telescope [90], The 12-m VertexRSI ALMA telescope [59][91], the JCMT telescope [25][26].

3.3. Primary Holography Design for FYST

In this section, as an exercise of using the technique described above, we present the primary holographic system design for the FYST telescope based on the required surface accuracy and spatial resolution. FYST will be located at the CCAT observatory at an altitude of about 5600 meters. The telescope is designed to observe up to 1500GHz, the 200-micron atmospheric window. Antenna tolerance theory indicates that the efficient surface precision of FYST should be better than 10.7µm to preserve the desired performance at 1500GHz. Under good measurement conditions, e.g., stable temperature and moderate wind, the goal of a < 7.1µm surface precision. Since FYST consists of two 6-m reflectors, to achieve the < 10.7µm surface precision, the rms of the surface errors on each reflector should be less than < 7.6µm. The reflector errors are contributed by panel manufacturing errors, deformations due to gravity and ambient temperature changes, and panel alignment error that depends on the surface diagnosis method, such as microwave holography. The total reflector error sources are summarized in Table 3.1 and 3.2 [58], where Table 3.1 shows the errors of an individual panel, and Table 3.2 gives the error budget of each reflector.

Error Source	RMS Error (µm)
Panel manufacturing error	3.0
Gravity ($30 - 150°$ elevation)	0.8
Ambient temperature changes $\Delta T = 15k$	0.14
Temperature Gradients (front to back side)=0.3K	1.86
Total panel	3.6

Table 3.1.: Surface error budget of an individual panel.

The error from the reflector measurement must account for a small fraction of the overall surface error budget, then the errors contributed by other sources can be measured and corrected. Here, We adopt the holographic measurement to align the reflectors and set its accuracy $\Delta\epsilon$ to 2µm which includes the effect of random errors due to the instrument noise and atmospheric fluctuations, and systematic errors, for example,

errors caused by telescope pointing trajectory errors and phase front errors from the receiver feed horn. In this primary design, we expect the contribution from random noise of the measurement system to be less than 1µm. To achieve such high measurement accuracy, we use a high frequency (300GHz) and put the holographic source relatively close to the telescope (300m away). Using a higher frequency means that a given fractional error in measuring the aperture phase converts into a smaller error in the surface.

Error Source	RMS error M1 (µm)	RMS error M2 (µm)
Total panel error	3.6	3.6
Panel alignment error	2	2
Manufacturing margin CFRP	3.5	3.5
Gravity	3.5	1.8
Wind (6m/s)	< 0.1	< 0.1
Ambient temperature change ΔT = 15K	1.4	1.4
Temperature Gradients (front to back side)=1K	< 0.44	< 0.44
Total reflector	6.6	5.9

Table 3.2.: Surface error budget of M1 and M2.

Parameters		**Value**
Frequency	freq	$300GHz$
Wavelength	λ	$\sim 1mm$
Aperture Diameter	D	$6000mm$
Beam size	λ/D	34.4 arcsec
Spatial Resolution	δ	$100mm$
Measured Map size	θ	0.6×0.6 deg^2
Sampling Points	N	61×61
Total measurement error	$\Delta\epsilon$	< 2µm
Error contribution from receiver noise	$\Delta\epsilon_1$	< 1µm
Other systematic errors	$\Delta\epsilon_2$	< 1.8µm
Required Signal-to-noise ratio for random error $\Delta\epsilon_1$	SNR	> 73.6dB
Measurement Time		< 1h

Table 3.3.: The main requirements for the FYST holography system

The spatial resolution of the measured reflector surfaces must be high enough to guide the corrections for individual panels. FYST consists of 146 square panels, 77 on M1 and

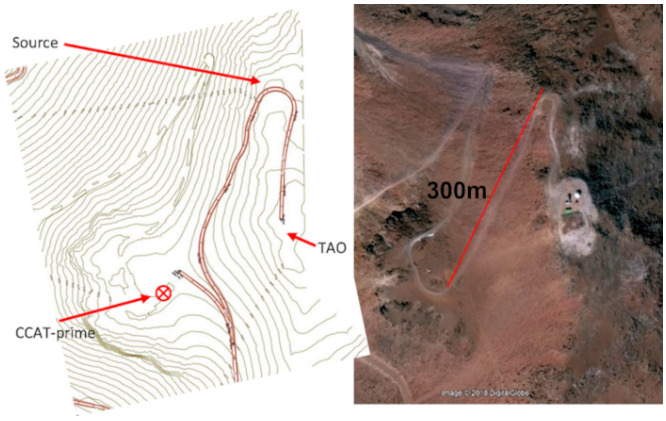

Figure 3.5.: Location of the holography source relative to the CCAT-prime and TAO site. South is at the top. The source is on the shoulder of the mountain where is about 20 meters higher than the telescope and 300 meters away.

69 on M2, with the size of 670 × 750mm and 700 × 710mm respectively. Each panel is supported by five vertical adjustment points to allow for correcting the higher-order panel deformations. A spatial resolution of 10cm is sufficient enough to resolve the panel errors and convert the surface error maps to the value of the adjuster movements. The holographic beam must be measured in an angular range of 0.6° at 300GHz. According to the equation 3.8, the required peak SNR of the measured beam map is around 73.6 dB. In addition, the measurement needs to be completed within an hour so that the reflector deformation caused by ambient temperature changes can be studied. In Table 3.3, we summarize the requirements for the FYST holography system.

Near-field holography system

To meet the requirement of high speed and high SNR holographic measurement, a 300GHz artificial transmitter is used and placed around 300m away from the telescope and 20m higher than FYST. Figure 3.5 shows the satellite geographic map of the locations of FYST and the holographic source. The transmitter acts as a point source and produces > 100µW (10dBm) output power. Extra optics is designed to converge the transmitter's output wave and provide a narrow beam (beam size of 1.8°), which makes the illumination pattern on the telescope's aperture nonuniform, but further improves the SNR. The nonuniform illumination can be corrected by taking deconvolution on the measured beam. The narrow beam also reduces the effect of stray light caused by the reflections of the ground between the transmitter and the telescope. The short distance also minimizes the influence of the atmospheric turbulence on the phase front distortion of the source beam.

The telescope's beam will be measured in both amplitude and phase, so a reference

antenna is required. Because the transmitter has a strong output power, we can use a heterodyne receiver [92] and an additional 10cm-size reflector to observe the transmitter and provide a phase reference for the holographic measurement. Here, the reference receiver uses the same electronic design as the receiver in the telescope's focal plane (signal receiver) and is mounted in the yoke of FYST (see Figure 3.6). The two receivers share a common microwave reference for their local oscillator. Their intermediate-frequency (IF) outputs are coherently sampled and converted to the frequency domain by fast Fourier transform by a digital correlator [61]. The measured signals will be operated in the specific channel. The digital correlator acts as a digital filter to reduce the noise bandwidth and further improve the SNR of the recorded data. The two receivers' power and cross-correlation are recorded in time sequence. The diagram of the electronic schematic of the FYST holography system is illustrated in Figure 3.7. The design of the electronic parts and the extra optical system in the source and reference receiver shown in Figure 3.7 will be described in Chapter 5.

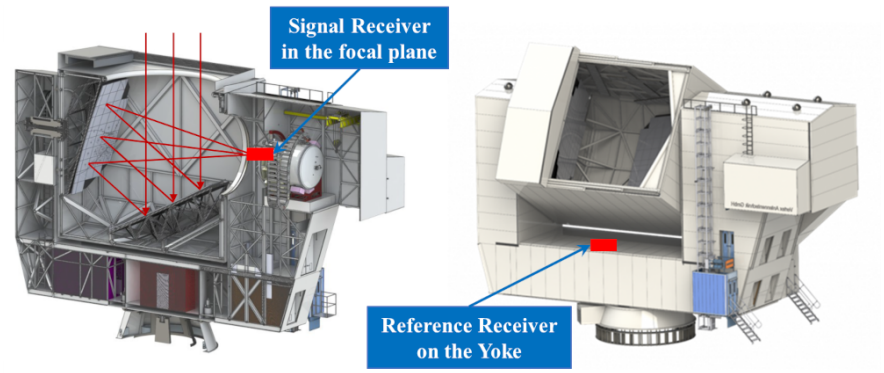

Figure 3.6.: The locations of the Signal Receiver and reference receiver in the telescope.

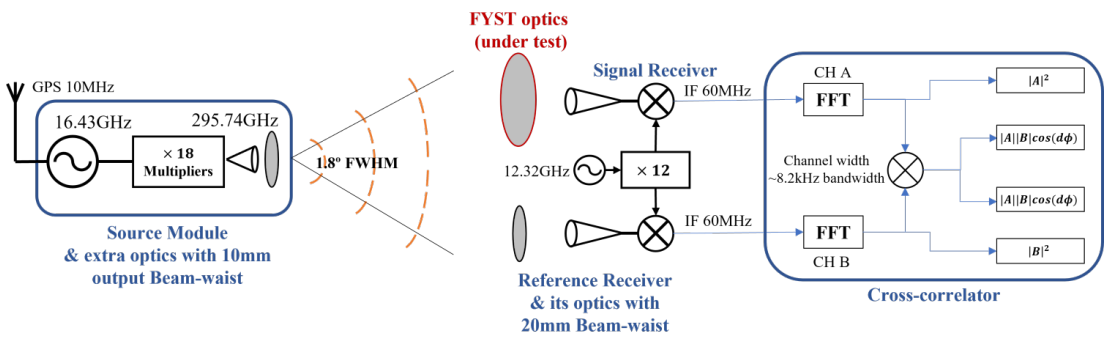

Figure 3.7.: Schematic of the FYST holographic measurement system.

3.4. Summary

In this chapter, the basic theory of the microwave holography technology has been presented. In the first part of this chapter, the holographic fundamentals and its designing criterion were explained based on the reflecting antenna's radiation theory. Next, the near-field holography measurement was presented. Finally, this chapter ended with a discussion of the primary holographic design for the FYST telescope to achieve $< 2\mu m$ measurement errors. In the next chapter, the issue of measuring the surface deviations for the FYST's two reflectors will be discussed.

Chapter 4.

Multi-map Holography for a Two-Reflector System

In this chapter, a new holographic metrology developed for measuring the shapes of the FYST's reflectors is presented. The chapter first points out the difficulty of using the conventional holography analysis to diagnose surface errors of a 'two-reflector' system. To address this challenge, a novel approach for measuring multiple beam maps is proposed, and its feasibility is demonstrated through geometrical analysis. This is followed by developing the corresponding software technique to convert the measured multiple maps into two surface error maps. Subsequently, a numerical study is conducted to assess the feasibility of the novel approach in which the effect of several noises and errors in the measurement system is explored. Next, this section concludes with a summary of the error budgets of the FYST holography measurement. Finally, this chapter ends with a discussion of the effect of the beam sampling grid that commonly is rectangular grids with uniform sampling, but it is proven that the new holography technique is not limited by the data sampling grid. In this chapter, the measured FYST's beam maps used for the numerical simulations are computed by the 'two-step' Fresenl-Kirchhoff method described in Chapter 2.

4.1. Introduction

The microwave holography technique described in Chapter 3 provides an efficient and accurate way to measure large radio telescopes' reflector shapes by observing their beam maps in the far or near field. But, employing this method to analyze the reflector surfaces of FYST presents challenges. Conventional holography only gives one surface error map, which is the sum of the surface errors of all telescope reflectors. For regular large radio telescopes, for example, Cassegrain telescopes, errors on the telescope's

secondary reflector can be neglected because of its small size and small and measurable manufacturing errors. So we can say the measured surface error map is the actual surface deviations of the large primary reflector. However, FYST is a Crossed-Dragone telescope with two 6-m reflectors (M1 and M2). Both reflectors are segmented into a set of rectangular panels, and these panels are assembled and aligned on the backup structure, which means the surface errors on the secondary reflector cannot be neglected anymore. Clearly, a single beam measurement cannot offer enough information to discriminate the surface errors between the two reflectors. We call this indeterminacy degeneracy between two surfaces. It could be argued that this does not matter since one could adjust one reflector, say M1, until the phase in the aperture plane was flat, which would provide a perfect beam even if there were errors in M2 which were being compensated by the deviations that had been put into M1. Unfortunately, this is impractical for two reasons: 1) The reflectors are made of relatively large panels (around 0.5m^2); Each panel only has five vertical adjusters to correct its shape, and the projections of these panels onto the aperture plane do not match, so an exact compensation is not possible; 2) A critical property of the FYST optical design, coma-corrected Crossed-Dragone optics, is to provide a wide field of view; the surface error compensation made by M1 would only work for the receiver at one position in the focal plane. As one moves the receiver to other positions, the projection of the two reflectors onto the aperture plane will change, and the compensation will not work anymore. Therefore, to preserve the best optical performance of the telescope at its entire field of view region, a new measurement technique is developed to break the surface error degeneracy in the 'two-reflector' system and measure their surface shapes separately.

4.2. Multi-map Microwave Holography Technique

Any surface errors in the FSYT's two reflectors lead to phase front errors on the telescope's aperture. In turn, the phase errors on the aperture distort the telescope's beam in the far and near fields. Adjusting the surface shape of one reflector can compensate for the aperture phase error produced by the other reflector and optimize the telescope's beam. But if the receiver was moved to different points in the focal plane, the compensation would fail because the phase errors contributed by the two reflectors are shifted in the aperture plane, which means the effect of the two surface errors is separated. Therefore, if we measure the telescope's beam at several separated points in the focal plane and analyze the observed beam maps simultaneously, we think the surface error degeneracy can be broken, and the error maps of the two reflectors can be obtained separately. Since this measurement requires more than one beam map,

we name it 'Multi-map' holography. The section first explains the feasibility of the new method in geometrical optics. Then the new holographic analysis method is presented to convert the measured beam maps to two surface error maps.

4.2.1. Geometrical Optics Analysis

We first make a simple discussion in ray optics to show that it should be in principle possible to adjust the FYST optics by measuring a few beam maps. Consider a distant source and a receiver located at the center of the focal plane. When the telescope reflectors are perfect, the light paths from the source to the receiver through different parts of the aperture are all the same. Now suppose that each of the reflectors M1 and M2 is introduced some path errors called δ_1 and δ_2. Within the approximation of ray optics, the total path error to the receiver becomes then $\delta_1 + \delta_2$. If we have an ideal measuring system with mounting receiver on-axis, we can adjust any of the reflectors to make the $\delta_1 + \delta_2$ to be zero, i.e. just correcting M1 surface to compensate error in M2. Because of the degeneracy, we cannot make δ_1 and δ_2 both to be zero, but we can make sure that δ_1 is equal to $-\delta_2$. This will be true at all points on the mirror surfaces, so we can write $\delta_1(\mathrm{x}_1, \mathrm{y}_1) = -\delta_2(\mathrm{x}_2, \mathrm{y}_2)$, where the points $(\mathrm{x}_1, \mathrm{y}_1)$ and $(\mathrm{x}_2, \mathrm{y}_2)$ lie on the same ray trace at M1 and M2 respectively.

If we then move the measuring system to a different point in the focal plane, i.e. off-axis, the rays now take a different path through the telescope. If we consider the same reflecting points $(\mathrm{x}_1, \mathrm{y}_1)$ on M1, they now are projected to $(\mathrm{x}_2^{'}, \mathrm{y}_2^{'})$ on M2 that can be expressed by $\mathrm{x}_2^{'} = \mathrm{x}_2 + \Delta\mathrm{x}$ and $\mathrm{y}_2^{'} = \mathrm{y}_2 + \Delta\mathrm{y}$. We should note that with the off-axis layout of the crossed-Dragone geometry $\Delta\mathrm{x}$ and $\Delta\mathrm{y}$ are not constant because the distance of the two reflectors top part is much further than that of the bottom part. Figure 4.1 illustrates the changes of the reflection points on M2 for the light coming from the same point on M1 but from different angles of the sky. So the measured path error becomes $\epsilon = \delta_1(\mathrm{x}_1, \mathrm{y}_1) + \delta_2(\mathrm{x}_2^{'}, \mathrm{y}_2^{'}) + \mathrm{A}(\mathrm{x}_2^{'}, \mathrm{y}_2^{'})$, where A is the additional path error due to the off-axis aberrations and can be calculated and corrected. Assuming the surface error varies smoothly, we can write $\delta_2(\mathrm{x}_2^{'}, \mathrm{y}_2^{'}) \approx \delta_2(\mathrm{x}_2, \mathrm{y}_2) + \Delta\mathrm{x} \cdot \mathrm{d}\delta_2/\mathrm{dx}_2 + \Delta\mathrm{y} \cdot \delta_2/\mathrm{dy}_2$. Since we already adjusted the surface of one mirror and arranged that $\delta_2(\mathrm{x}_2, \mathrm{y}_2) = -\delta_1(\mathrm{x}_1, \mathrm{y}_1)$, we can get the expression $\epsilon = \Delta\mathrm{x} \cdot \mathrm{d}\delta_2/\mathrm{dx}_2 + \Delta\mathrm{y} \cdot \mathrm{d}\delta_2/\mathrm{dy}_2$. Therefore, it means we can make just one additional measurement with an offset the receiver in the x direction, employing the conventional holographic analysis can get ϵ, then we integrate the $(\epsilon/\Delta\mathrm{x}) \cdot \mathrm{dx}_2$ to compute $\delta_2(\mathrm{x}_2, \mathrm{y}_2)$. In principle, making a beam measurement with an offset in the y direction for the receiver also gives the same result $\delta_2(\mathrm{x}_2, \mathrm{y}_2)$. This argument based on ray tracing optics proves that employing at least two holographic measurements with putting the receiver at different well-separated points in the focal

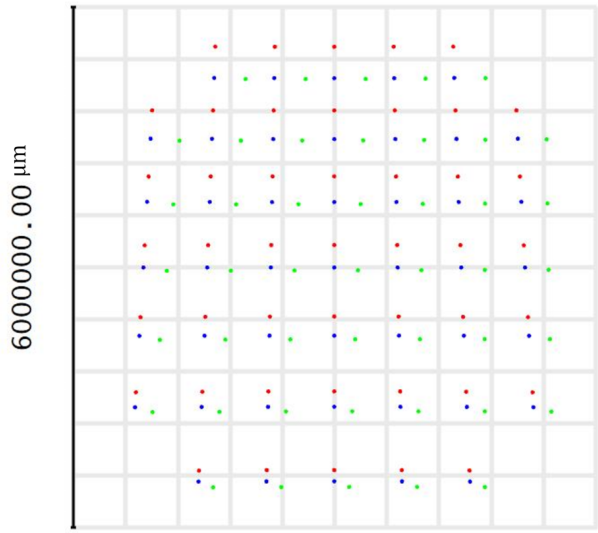

Figure 4.1.: The reflection points on M2 surface for the light reflected by same points on M1 with 3 different incident angles, blue points for light from $(0°, 0°)$ of the sky, green for $(2.6°, 0°)$ and red points for $(0°, 2.6°)$.

plane can discriminate surface errors on the two mirrors. But the ray tracing optics does not consider the diffraction effects between the wave propagation between the two reflectors.

4.2.2. New Analysis Technique

Based on the analysis in ray optics, moving the holography to two different well-separated points in the focal plane would be sufficient to break the degeneracy between the panels of the two mirrors. Considering the presence of noise in the measurements, we think the degeneracy breaking can be further improved by making additional measurements by moving the receiver both in the x and y axes. We plan to use five points - the center of the field and the corners of a square, as illustrated in figure 4.2 left, to cover the focal plane. The corresponding focused beam patterns with the receiver at the five positions are simulated and displayed in figure 4.2 right. As the holography beam patterns are observed, we cannot find any obvious direct method, which is analogous to an inverse Fourier transform, for converting the five beam maps into two surface error maps. Instead, we treat this as a numerical inference problem. We come up with three approaches:

1. Direct inversion and fit the mirror surface using ray optics. Taking the inverse transform of the observed beams gives five aperture field distributions. For the near-field measurement, geometrical corrections are required because the source

is located at a finite distance from the telescope. The second step is to use the ray tracing method to fit the movements of the panel adjusters that can produce wavefront errors that best match the measured wavefront. Applying this method doesn't consider the diffraction issues of the detailed geometry of the telescope, such as the diffraction that takes place from one reflector to the other, including the effect of the panel gaps in the reflectors. Figure 4.3 shows the diffraction fields on M1 that are produced by M2, which shows strong diffraction fringes on M1 edge panels.

2. Direct inverse transform of the measured and simulated beams. This method still takes the direct inversion for measured data and also for the ideal beam maps that are simulated by the accurate physical optics method described in Chapter 2. Then, we could subtract the perfect aperture fields from the measured aperture fields, and the diffraction issue mentioned in method 1) can be removed. After this, we can continue using the ray optics fitting process to fit the shapes of the two reflectors.

3. Fit the reflector surfaces by directly comparing measured beams to simulated beam maps. We think it is not necessary to convert the beam maps of the telescope to its aperture fields and process the data there. We can fit the reflector surfaces by directly comparing the measured data with the simulated beams. Specifically, we should find a way to parametrize the surface deviations of the reflectors, such as using a set of orthogonal two-dimensional polynomials (e.g., Zernike polynomials for circular mirrors) or direct using the movement values of the panel adjusters to describe the panel errors. Then the beam maps of this parameterized model can be predicted by numerical simulations. We call this calculation the 'Forward' function with variables of these parameters. Employing the numerical fitting technique, we can find the set of parameters for the two reflectors that best account for the measured data. This method requires a fast and accurate algorithm for computing the 'forward' function for any given reflector parameters.

The third method will be employed to analyze the five measured beams. There are numerous advantages with this approach: 1) we can use an accurate formulation of the electromagnetic aspects that includes a proper treatment of the rather complex geometry of the telescope and of the diffraction that takes place between the components and in the path from the source; 2) we directly deal with the original measured data, it means more information is preserved so that we can study the effect of systematic errors, like telescope unknown pointing errors, and find a way to avoid or minimize their influence; 3) using this method, we can include various parameters that are used to

represent systematic effects such as the uncertainty in the position of the receiver and inaccuracy of the illumination pattern of the receiver and the source. In the rest of this section, the details of this approach are explained, including the parameterization of the mirror surfaces and systematic errors, the algorithm of the 'forward' function used to predict the telescope's beam map with any reflector surface errors, and the details of the fitting procedure.

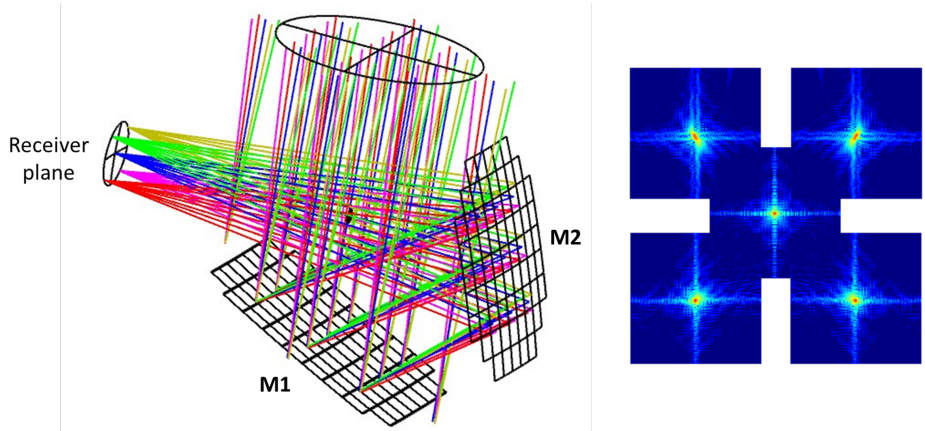

Figure 4.2.: Left: The optical layout of the 'crossed-Dragone' FYST telescope. The ray trace shows that the light path error produced by two mirror surface errors is degenerate. It also indicates that moving the receiver to different points in the focal plane, here the focal plane center (blue) and four corners of a square 800mm on a side, can change the reflection points on the M2 surface, breaking the light path degeneracy between the reflectors. **Right:** The corresponding focused beams with the holography receiver at the 5 points in the focal plane.

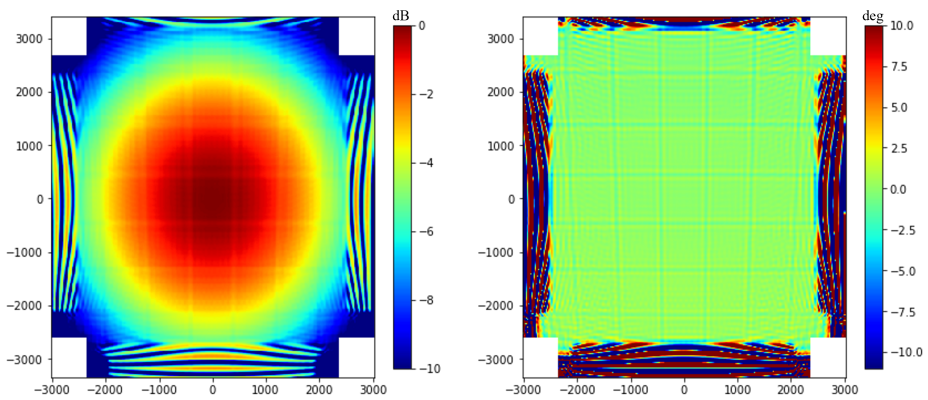

Figure 4.3.: The field on the primary mirror (M1) of the FYST telescope that is produced by its secondary mirror at frequency of 296GHz for the holography receiver at the telescope's nominal focus. **Left:** The amplitude distribution of the field on panels of M1; **Right:** The projection of the phases of the M1 fields on telescope aperture.

Parametrize Reflector Surface Errors

The FYST's reflectors are made of a set of square panels, 69 on M2 and 77 on M1, with panel sizes of 670 × 750mm and 700 × 710mm respectively. Each panel is supported by five adjustable mounts in the z-axis, one of which is in the center and the four at the corners of a rectangle, $440 \times 500mm$ in size shown in figure 4.4 (left). Since we wish to be able to set the reflectors, rather than simply measure them, what we actually need is the values of the adjustments that should be made to obtain a perfect reflector surface. Therefore, we decided to choose these adjustment values as the parameters that we tune to find the best fit for the measured beam patterns. Since the panels are almost square, and the four supporters are located close to the panel corners, with these five adjusters we can control five surface error terms for each panel - piston, x or y tilt, curvature, and twist shown in figure 4.4 right. This means that the panel deformations $\epsilon(x, y)$ can be described by a 2nd-order polynomial expressed by formula 4.1.

$$\epsilon(x, y) = a + bx + cy + d(x^2 + y^2) + exy \tag{4.1}$$

If the five adjustments on each panel are noted by s_0, s_1, s_2, s_3 and s_4, the coefficients of the formula can be expressed by $a = s_0$ for piston, $b = (s_1 + s_4 - s_2 - s_3)/4l_x$ and $c = (s_1 + s_2 - s_3 - s_4)/4/l_y$ for x/y-tilt, $d = [(s_1 + s_2 + s_3 + s_4)/4 - s_0]/(l_x^2 + l_y^2)$ for curvature term, and $e = (s_1 - s_2 + s_3 - s_4)/4l_xl_y$ for twist panel error, here, l_x and l_y are the offsets of the four corner adjusters in x and y axes. The formula will be used to interpolate between the support points onto a grid suitable for performing electromagnetic calculations. The more accurate way of modeling the panel deformation caused by supporter movements is to do finite element analyses (FEA) for a panel, here, since the supporter errors will be less than 20µm, then using the above model should be a reasonable approximation.

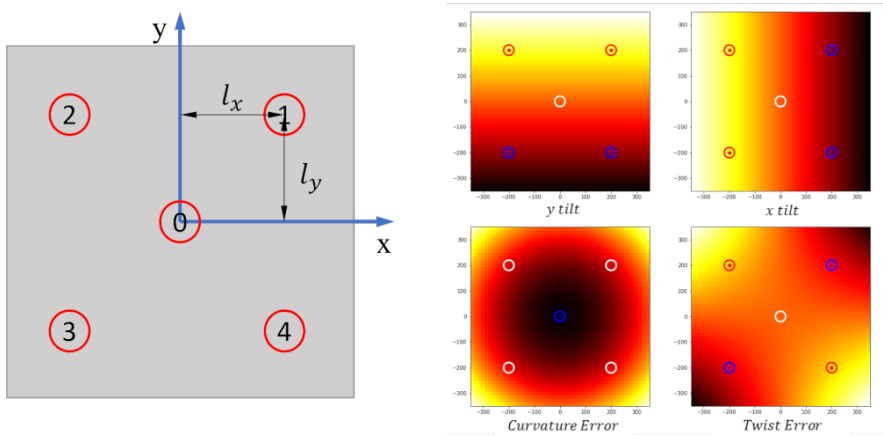

Figure 4.4.: Left: The five z axis adjusters locations in the panel. **Right:** The four low-order panel deformation terms, x and y tilt error, curvature Error, and twist error.

As an alternative, which may be useful for the diagnosis of some issues such as thermal deformations, we can ignore the panels and their mounting points, and parameterize the whole of each mirror in terms of a set of orthogonal functions such as Zernike polynomials [11] that is widely used to analyze aberrations of circular optics. Although the mirrors of the FYST telescope have zigzag rims, and the illumination fields on the mirrors are not uniform, the strict orthogonality are not meet when the Zernike polynomials are applied to the FYST surface parameterization. We though that nonetheless approximate orthogonality is still maintained. The maximum order of the polynomials is determined by the spatial resolution required.

Parametrize Errors in Large Spatial Scales

There are a number of effects in the practical system other than surface errors, which will cause a mismatch between the observed data and simulations. These include an error in the position of the holographic receiver, uncertainty of the receiver's beam, and inaccuracy of the assumed distance from the telescope to the source. These errors will make a smooth modification in the field phase over the aperture, which are called errors in large spatial scale, for example, the pointing offset and receiver lateral displacement corresponding to linear phase gradients across the aperture and aperture phase curvature produced by z-position error of receiver and source. We also need to account for that the amplitude pattern in the aperture is not an exact match to the one that we have assumed, which is affected by the inaccuracy of the designed Gaussian beam size of the receiver's feed horn and the illumination taper of the source.

These large spatial errors can degrade the measurement accuracy of the reflectors. Fortunately, we do not need to know these errors for the purpose of setting the reflector

panels, we can parametrize these errors and include them as free parameters in the model. We do this by including in the model a multiplication term $\mathbf{M}_{ap}(x, y)$ for the aperture fields, which is expressed by equation 4.2.

$$\mathbf{M_{ap}}(x, y) = \Delta A_{ap} \cdot e^{i \cdot \Delta\phi_{ap}}, \tag{4.2}$$

$\Delta \mathrm{A_{ap}}$ and $\Delta\phi$ in this equation represent correction terms in amplitude and phase expressed by equation 4.3, where x and y are the positions of the point in the aperture plane.

$$\Delta A_{ap} = A_0 \cdot (1 + ux + vy + wxy + sx^2 + ty^2) \tag{4.3a}$$

$$\Delta\phi_{ap} = \phi_0 + ax + by + c(x^2 + y^2) \tag{4.3b}$$

The phase term $\Delta\phi$ gives four parameters, allowing for fitting the large spatial errors that cause tilted and quadratic phase terms in the aperture plane. The correction term $\mathrm{A_{ap}}$ for amplitude is a linear approximation for the Gaussian beam assuming the changes in beam center and beam width are small. The accuracy of using these correction terms has been verified by numerical simulations in section 4.3.3. It should be noted that these approximations in phase and amplitude corrections only work as long as these errors are small, for example, < 5 mm position error of the receiver. Now there are 10 additional parameters required to be fitted for each measured beam map. We also should pay attention to that these large spatial errors on the aperture also could be represented by certain combinations of the movements of the panel adjusters in either of the reflectors, which are not the real surface deformations on the reflectors. This gives rise to the new degeneracy in the solution when seeking the best fit. To deal with this, we plan to use a regularization term in the fitting model to compress the total amount of the adjuster movements and assume the large spatial phase errors come from the misalignment of the system. The details will be explained in the fitting procedure section.

Forward Function

When the surface deviations of the reflectors are parametrized, the 'forward' function of these parameters is used to predict the telescope's distorted beam maps. This section talks about how to establish a 'forward' function that can efficiently and accurately simulate the telescope's beams. In the actual experiment, the reception beams of the telescope are measured. The process is that the signal comes from a distant source and is scattered by the telescope's reflectors and recorded by the receiver in the focal plane. According to the antenna's reciprocity theorem, the reception beam of an antenna is

equivalent to its radiation beam pattern which is the time-reserved process of that we described above. In order to simulate the telescope's beam performance, it is convenient to model the telescope's radiation beam pattern, starting from the receiver and through the telescope's optics, to find the field on a spherical surface at the distance of the source.

The numerical fitting technique will be used to solve the reflector surface errors from the measured beam maps. According to the numerical simulations that we will be presented in the later sections, the fitting process generally requires thousands of calculation loops to find the optimum solutions. To achieve a reasonable analysis time e.g., < 1 hour, we expect one calculation loop needs to be done within a few seconds or even less. One option is to apply the highly efficient fast Fourier transform (FFT) algorithm to convert the aperture fields to the telescope's far-field beam based on the Fourier transformation relationship described in Section 2.1.3. The aperture fields can be computed using geometrical optics. But this technique does not consider the diffraction effects of the wave propagation between the FYST's two reflectors. Then, a more accurate but time-consuming method, physical optics (PO) analysis, is employed to account for this effect. Fortunately, in Chapter 2 the new 'two-step' Fresnel-Kirchhoff analysis has been developed to speed up the physical optics analysis, which can reduce the computation time of the PO analysis from a week to < 1 minute on a personal computer (e.g. Intel i7-10700 CPU) and still achieve the field accuracy of < 70 dB below the peak value of the beam. As our goal is to reduce the computing time to less than a second, additional linear approximation is studied and applied to the beam calculation, which will be discussed in the rest of the section.

The details of the 'two-step' Fresnel-Kirchhoff analysis for the FYST telescope have been presented in Chapter 2. This technique speeds up the fundamental PO analysis by incorporating two changes: 1) instead of using the complex PO expressions, the scalar Fresnel-Kirchhoff integration formula [11] is applied, where the vector electromagnetic field is described as scalar quantify. So the cross-polarization beam of the telescope cannot be expressed, which is not important for the holographic analysis; 2) the PO analysis flow explained by the black arrows in figure 4.5, are replaced by the four-step calculations, see the green arrows in the figure. The most time-consuming process in the PO analysis is step 2 which is the calculation of the fields in M1 scattered by M2 because the two reflectors are separated only by 6 m, the phase of the fields on M1 radiated by the PO current elements on M2 changes very fast over the M1 surface, we need to sample the M2 surface very densely (e.g., $> 7000 \times 7000$ points) to preserve the calculated field accuracy on M1. Step 2 is broken into two processes, calculating the fields in the intermediate focal (IF) plane of M2 where the fields are confined in a small

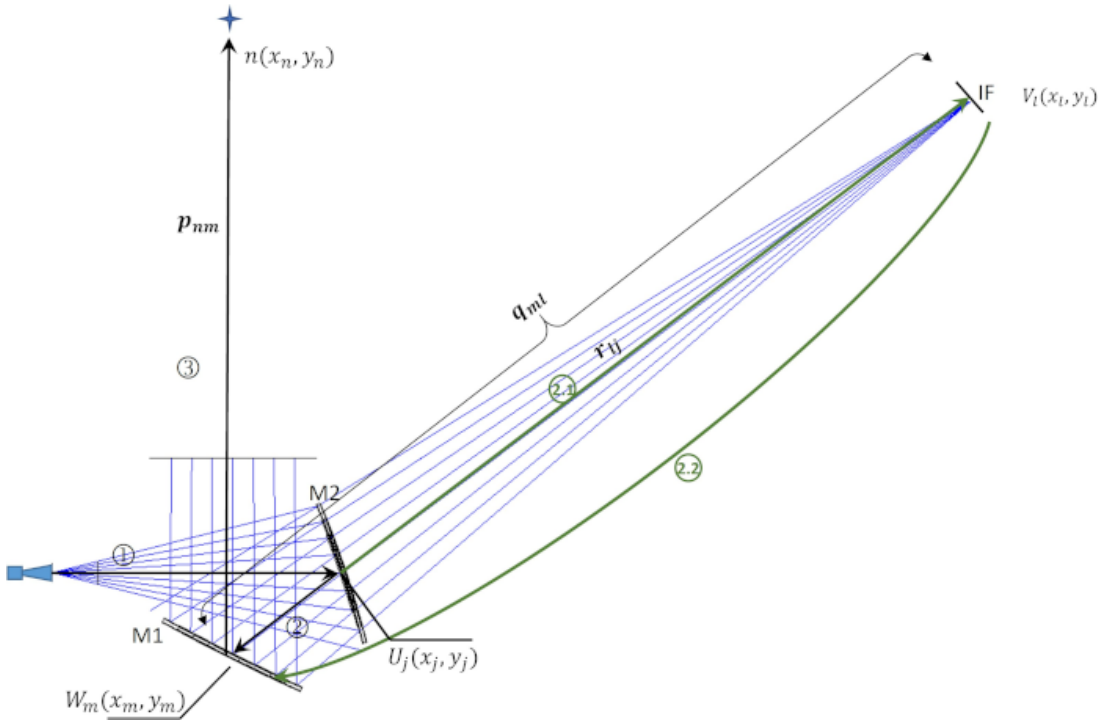

Figure 4.5.: Beam calculation process in the inference holographic analysis. The black arrows indicate the standard wave propagation process, where the output beam starts from the receiver feed to illuminate M2, then is scattered to M1, and reflected to the sky or source region. The blue arrows represent the calculation process of the new two-step Fresnel-Kirchhoff diffraction method, which breaks the wave propagation from M2 to M1 into two steps using the intermediate focal plane of M2.

region, and calculating the fields on M2 from the fields in M1.

We first formulate the calculation processes described above in figure 4.5. We denote the field as U_j in M2, V_l in IF plane, W_m in M1, and S_n for fields in the source region, where the subscript represents the point on the reflectors or plane surface. Based on the Fresnel-Kirchhoff integration formula expressed in equation 2.19 the computing steps can be expressed by following equations:

$$V_l = \frac{-i}{\lambda} \sum_j \frac{e^{ikr_{lj}}}{r_{lj}} \cdot \Delta S \cdot U_j \tag{4.4a}$$

$$W_m = \frac{-i}{\lambda} \sum_l \frac{e^{-ikq_{ml}}}{q_{ml}} \cdot \Delta A \cdot V_l \tag{4.4b}$$

$$S_n = \frac{-i}{\lambda} \sum_m \frac{e^{-ikp_{nm}}}{p_{nm}} \cdot \Delta S' \cdot W_m, \tag{4.4c}$$

where λ is the operating wavelength, and r_{lj}, q_{ml} and p_{nm} represent the distance between source field points and target field points in each wave propagating process, ΔS, ΔA and $\Delta S'$ are the surface elements on M2 surface, IF plane and M1 surface respectively. Here,

the sum of the cosine term in the integration formula 2.19 is approximately constant, equal to 2.

The next step takes the reflector surface errors into account in the calculations. The slight reflector distortions do not impact the intensity of the fields on the reflector surfaces. Phase changes of the fields are proportional to the surface deviations from the ideal position. Here we denote the surface deviations ε_1 on M1 and ε_2 on M2 as shown in figure 4.5, the field calculation process in equation 4.4 is rewritten as below:

$$\begin{aligned} V_l &\approx \frac{-i}{\lambda}\sum_j \frac{e^{ik\cdot(r_{lj}-\varepsilon_2 cos\theta_j^r)}}{r_{lj}}\cdot \Delta S\cdot U_j e^{-jk\varepsilon_2\cdot cos\theta_j^i} \\ &= \sum_j \mathbf{A}_{lj}\cdot U_j\cdot e^{-ik\varepsilon_2\cdot(cos\theta_j^i+cos\theta_j^r)} \\ &= \mathbf{A}\cdot\mathbf{U} \end{aligned} \tag{4.5a}$$

$$\begin{aligned} W_m &\approx \frac{-i}{\lambda}\sum_l \frac{e^{-ikq_{ml}}}{q_{ml}}\cdot \Delta A\cdot V_l^{'} \\ &= \sum_l \mathbf{B}_{ml}\cdot V_l \\ &= \mathbf{B}\cdot\mathbf{V} \end{aligned} \tag{4.5b}$$

$$\begin{aligned} S_n &\approx \frac{-i}{\lambda}\sum_m \frac{e^{-ik\cdot(p_{nm}+\varepsilon_1 cos\theta_m^r)}}{p_{nm}}\cdot \Delta S^{'}\cdot W_m e^{-jk\varepsilon_1\cdot cos\theta_m^i} \\ &= \sum_m \mathbf{C}_{nm}\cdot W_m\cdot e^{ik\varepsilon_1\cdot(cos\theta_m^r+cos\theta_m^i)} \\ &= \mathbf{C}\cdot\mathbf{W}, \end{aligned} \tag{4.5c}$$

where the metrix elements, A_{lj}, B_{ml} and C_{nm} are the summation elements $e^{ikr_{lj}}/r_{lj}\cdot\Delta S$, $e^{ikq_{nm}}/q_{nm}\cdot\Delta A$ and $e^{ikp_{nm}}/p_{nm}\cdot\Delta S^{'}$ in equation 4.4, here we neglect the factor $\frac{i}{\lambda}$. It is seen that these matrixes do not depend on surface deviations, so they just need to be computed once for the distorted beam calculations. In equation 4.5, θ^i and θ^r represent the incident and reflection angles at the field points on the two reflectors. Therefore, to predict the beam map distorted by the surface deviations, we convert the surface errors (ε_1 and ε_2), which are expressed by the parameters of the panel adjuster movements, into the field phase changes. Then following the matrix multiplication in equation 4.5, the fields distorted by the given surface errors are gotten.

In addition, the parameters used to compensate for the large spatial scale errors described in section 4.2 are also included in the forward calculation. Before calculating the field S_n in the source region, the field on the M1 surface (W_m) is multiplied by the compensation term in the equation 4.2. The compensated M1 field and then is expressed by $W_m^{'}\cdot\Delta A_{ap}\cdot e^{i\Delta\phi_{ap}}$. Finally, the desired field S_n in the source region is

computed. This method requires one detailed and time-consuming beam calculation in advance that costs around 3 minutes for one beam calculation of the FYST telescope using a normal personal computer, and the intermediate results are saved in memory. Then carrying on the matrices multiplications will require < 1 second using normal 4 cores CPU and < 0.1 second with a graphics processing unit (GPU) e.g. using Nvidia GeForce RTX 3070.

Fitting Procedure

We are now presenting the inference process using the forward function and parameters developed in the sections mentioned above. The measured complex fields at a set of points i in the beam map are denoted by $\mathrm{D_i}$. The fields are normalized by the total power of the entire measured beam, and the phase terms are corrected by the phase in the beam center. Then the fields computed by the developed forward function are labeled as Y_i, assuming initially that the telescope surfaces are perfect and the same normalization and phase correction are applied to the data. The disagreement between the measured data and modeled fields is characterized by the residual vector $\mathrm{E_i} = \mathrm{Y_i} - \mathrm{D_i}$. The best fitting movements $\mathrm{S_n^{M1}}$ and $\mathrm{S_m^{M2}}$ of the adjusters on M1 and M2 and large spatial parameters described in section 4.2 are found by minimizing the sum of $|\mathrm{E_i}|^2$ over all the data points.

Although the degeneracy between the surface errors of the two reflectors can be broken by measuring more than one beam map in the focal plane, it should be noted that this separation will only work really well for errors with relatively small spatial scales; the errors on larger scales will still be nearly degenerate. This can be easily seen by considering a sample case of a linear phase error; a tilt of one mirror would be compensated almost exactly by the reverse tilt of the other mirror, no matter where the receiver is located in the focal plane. In addition, the large spatial errors described in section 4.2 are also degenerate with the reflector deformations in large scales. The existing degeneracy can result in over-fitting of the parameters $\mathrm{S_n^{M1}}$ and $\mathrm{S_m^{M2}}$. To avoid the degeneracy, we include in a quantity to be minimized the magnitudes of the adjuster movements multiplied by the regularization factor λ_0, which assumes that mirror surface deviations are small and dominated by panel distortions. The value of the regularization factor is not critical. It needs to be large enough to suppress the degeneracy but not so large that it prevents the fitting process from finding real surface deformations. We can do the minimization process and inspect the fitting mirror surfaces and data matching between model beam patterns and measured data by changing the value of this factor.

Therefore, the quantity to be minimized is given by equation 4.6 called the loss function.

$$R = \sum_i |\mathbf{Y}_i - \mathbf{D}_i|^2 + \lambda_0 \cdot (\sum_n (S_n^{M1})^2 + \sum_m (S_m^{M2})^2) \tag{4.6}$$

The analysis flow of the fitting technique is illustrated in figure 4.6. If five beam patterns were measured and used for the surface analysis, there would be 750 parameters (5×69 adjusters on M2, 5×77 adjusters on M1, and 10×5 large scale parameters for the five measured beams) required to be fitted. We employed the Broyden–Fletcher–Goldfarb–Shanno (BFGS) algorithm [93] as the iterative method for solving the nonlinear minimization problem that requires the gradient of the loss function R defined in equation 4.6. Computing the function's gradient is expensive if there are abundant variables. We employ the automatic differentiation technique [94], which is based on applying the chain rule to accumulate the numerical value of the differential as the developed algorithm executes. Then gradient of the loss function $\nabla\mathbf{R}$ for all variables can be calculated by tracing back along the algorithm execution path. This technique has the advantage that the computing time of evaluating $\nabla\mathbf{R}$ is in the same order as calculating the loss function $\mathbf{R}$ and independent of the number of variables. The method is established using the package PyTorch [95], which makes it easy to use and automatic offloading onto GPUs.

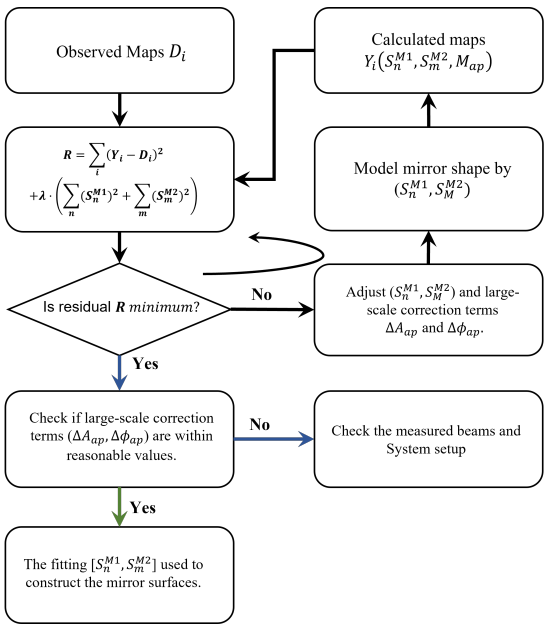

Figure 4.6.: Flowchart of the basic inference process used to find the panel adjuster movements required to set the mirror surfaces.

The fitting software will be very sensitive to large-scale parameters if the holography

system has a large absolute pointing offset or focus error. According to numerical simulations, it is more efficient to find the best-fit mirror surfaces by two steps: 1) fit the large-scale parameters to find telescope pointing and focus error by setting all adjuster movements to be zeros; 2) the fitting large-scale parameters are fed into the software as the initial values to fine-tune these values and find the values of the adjuster movements. This inference method's feasibility and detailed data analysis process will be tested with numerical simulations in the next section.

4.3. Numerical Simulations for the FYST Holography

In this section, the feasibility, accuracy, and sensitivity of the new holography technique described above are investigated by numerical simulations. These simulations are carried out at 296GHz for the FYST telescope to find the optimum set-up, observational approach, and data analysis flow for the FYST holography. The following aspects are investigated: 1) What is the best-separated distance of the receiver for measuring the multiple beam maps; 2) the effect of realistic errors, including random errors and systematic errors, such as measurement system drift, telescope tracking error, and atmospheric turbulence; 3) the influence of modeling errors for the holography system, such as telescope optical misalignment and inaccuracy of source illumination beam and feed-horn beam pattern; 4) check if the new technique can measure large-scale surface errors on the two reflectors.

The FYST holography system described in Chapter 3 requires measuring the telescope beam map in the near field where the source is around 300m from the telescope. The 'best' focus of the telescope is moved to $\sim$ 725mm behind the astronomical focal plane. The new holographic analysis method does not rely on having the receiver at this 'best' focus. It is easy to see that, in fact, it is better to have the receiver somewhat closer to the focal plane. Figure 4.7 shows the FYST optics layout, the position of the original focal plane, and the 'best' focus plane. Figure 4.8 shows the cut through the beam pattern for the focused optics and the cases with the receiver moved forward by 125, 225, 325, and 425mm from the new focus. The plane with a 125mm offset mounts the receiver and measures the telescope's beam maps. The effect is to spread out the beam so that the peak gain is reduced by $\sim$ 20 dB. This offers the advantage of reducing the dynamic range required for the measurement system. In principle, we could defocus the beam further, but if we spread the beam too far, we will start to lose some of the detailed information on the reflector surfaces because parts of the beam patterns are pushed outside the measured area, like the green curve in figure 4.8. Therefore, beam maps must be measured in an extensive angular range to achieve the required spatial resolution.

It can be seen that with 125mm of defocus, the power is still largely contained within a region $\sim 0.2°$ in diameter, which is small compared to the $0.6°$ diameter of the map designed to achieve 100mm spatial resolution in the measured surface maps.

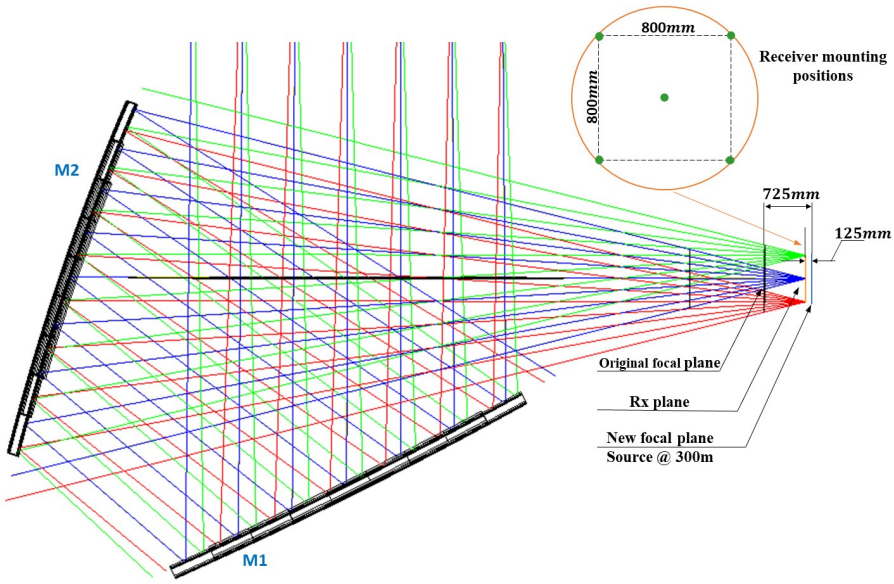

Figure 4.7.: Optics layout of the FYST telescope with a source at 300m from telescope aperture and the receive mounting locations. The new focus is changed to $\sim$ 725mm behind the original focus. The receiver plane is 125mm before the new focal plane. The receiver will be mounted in the center and four corners of a square that is 800mm on a side.

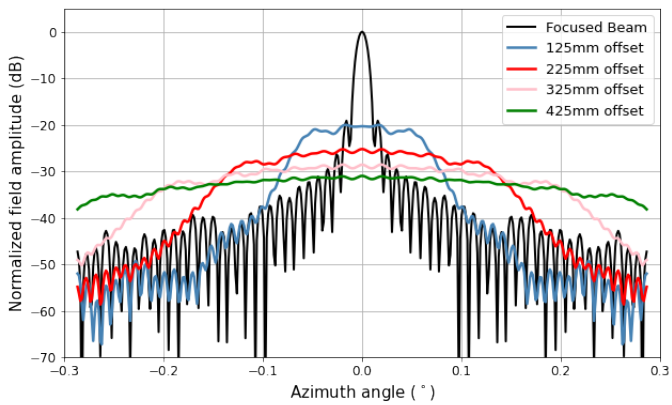

Figure 4.8.: The cut of the focused beam (black) and the defocused cases with the receiver 125mm closer to the original focal plane than the best-focus position (blue). The beam patterns are simulated using the 'two-step' Kirchhoff diffraction method for the FYST telescope with perfect mirror surfaces.

The new holography technique requires measuring two or more beam maps. In the

practical FYST holography, we plan to measure the beams at five points in the focal plane shown in figure 4.7, four at the corners of a square and one in the center. To test the new data analysis approach, a set of random movements at the panel adjusters with a magnitude of 30µm RMS are introduced. Figure 4.9 shows the produced surface errors on the two reflectors. The four off-axis beams together with the on-axis beam, with and without the surface errors, are calculated by the 'two-step' Kirchhoff diffraction approach and shown in figure 4.10. The beam calculation method has been developed in Chapter 2, and the accuracy of this method has been checked by comparison with the industry-standard GRASP software. If we load the five beam maps into the developed inference software and take the perfect surface as the starting point, the offset values of the adjuster from their ideal positions can be solved to very high accuracy ($\ll$ 1µm). This is not surprising since we use the same method to get the measured beam maps and to do the forward calculation in the fitting.

In the rest of the section, the measurement noise and the instrument effects in the practical tests are simulated and added to the measured beam maps. The measured data denoted by $\mathrm{D_i}$ is replaced by noisy data $\mathrm{D_i^{'}}$ expressed by the following equation.

$$D_i^{'} = D_i \cdot (1 + \Delta G_i)\ e^{j\Delta\phi_i} + N_i, \tag{4.7}$$

where $\mathrm{N_i}$ is a set of random Gaussian variables with zero mean and RMS of σ, representing additive noise, and $\Delta\mathrm{G_i}$ and $\Delta\phi_\mathrm{i}$ are multiplicative errors which could arise from gain and phase fluctuations of the holographic instruments or the atmosphere. We define the signal-to-noise ratio (SNR) as the ratio of the peak amplitude, for the case of the map made with perfect reflectors and with the receiver at the best-focus position, to the noise, σ. The multiplicative terms are random, but, to make them realistic, they are not white noise but instead filtered to produce a smoother variation with time. This enables us to study the effects of systematic drift and atmospheric turbulence on the final measurement accuracy and to develop a method or observational approach to remove these effects.

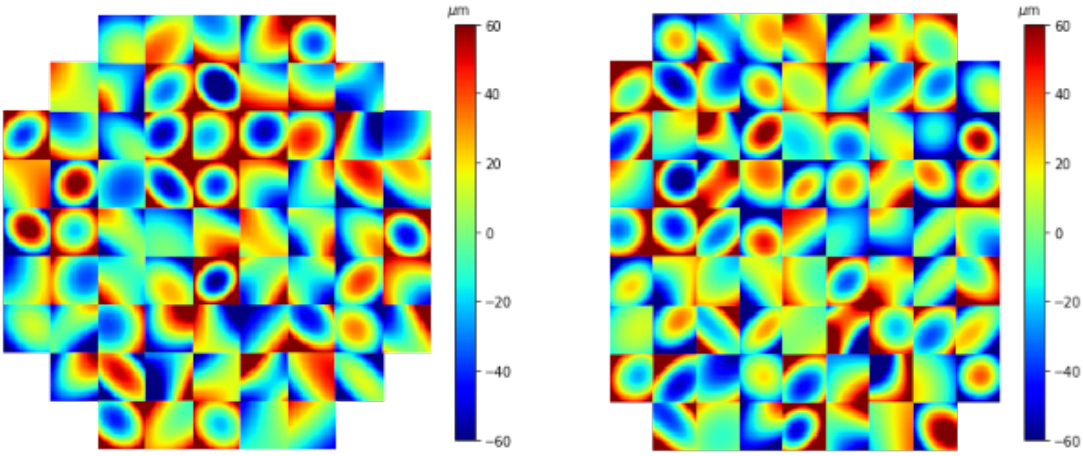

Figure 4.9.: Surface error maps with 30µm RMS random movements at the adjusters: secondary mirror (M2) on the left and primary mirror (M1) on the right.

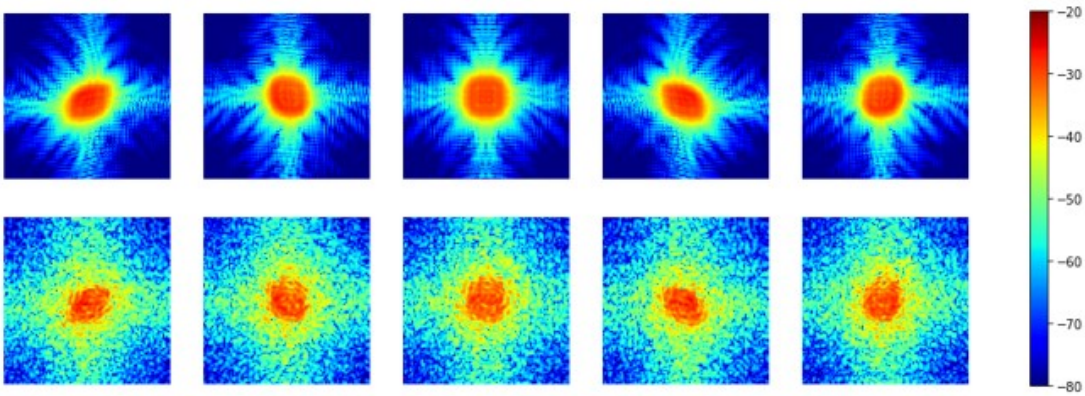

Figure 4.10.: Amplitude of the beam maps (relative to the focused peak) with the receiver located at four off-axis points and center in the focal plane, from left to right, a receiver located at [400,400], [400,-400], [0,0], [-400,400] and [-400,-400]. Top row - ideal mirror surfaces; bottom row - with the surface errors shown in figure 4.9. The square maps cover 0.57×0.57 degrees.

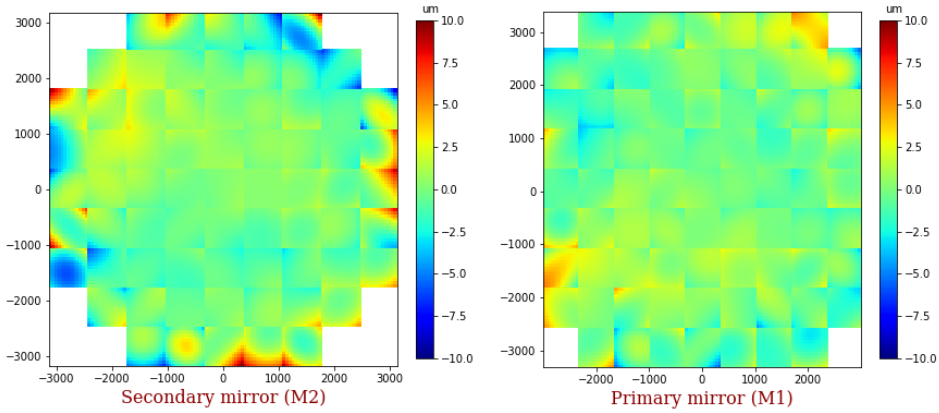

Figure 4.11.: Deviations of the best-fitting surfaces from the input surfaces where noise with amplitude -65dB with respect to the peak power was added to the data. The root-mean-square of the illumination-weighted surface errors is 0.5µm on M1 and 0.6µm on M2.

The simplest case is to add the random noise to the five off-axis beam maps in figure 4.10, assuming the noise with amplitude -65 dB related to the peak power of the focused beam. The values of the adjuster movements are solved from the five noisy maps and converted to surface deformations of the two reflectors. Compared to the input reflector surfaces shown in figure 4.9, the error of the measured surface shapes are plotted in figure 4.11. RMS of the measurement errors is about 1.5µm. It can be seen, however, that most of the errors occur near the edges of the mirrors, particularly on M2. In the case of M1, the reason for this is the lower illumination at the outer edge by the receiver horn. On M2, only the inner region contributes to all five of the beam patterns - the regions near the corners are in the signal path for only one of the maps. This means that the RMS over the whole surface is a pessimistic estimate of the actual operational performance of the telescope. A reasonable representation of the measurement error is multiplying the surface errors by the illumination amplitude pattern of the feed horn. RMS of the 'illumination-weighted' surface errors is used to present the measurement accuracy expressed by ϵ. Then RMS of the illumination-weighted surface errors in figure 4.11 is about 0.6µm.

4.3.1. Effect of Random Noise and Holographic Setup

We first study the relationship between measuring accuracy, measurement noise, and space of the receiver locations in the focal plane. The ratio of the peak of the focused beam to the deviation σ of the thermal noise is expressed in terms of the voltage ratio. The range is from 55dB (voltage ratio 560) to 70dB (3200). The measured maps

consist of 61 by 61 points to sample each beam map in the range of 0.6×0.6 degrees, which satisfies the Nyquist sampling theorem. The curves in figure 4.12 illustrates that the measurement error is inversely proportional to the signal-to-noise ratio of the measurement if assuming the holographic setup is fixed. This agrees with the measuring accuracy of the holography system described in Chapter 3. The conventional holography measurement with SNR of 65dB produces a 2.6µm surface accuracy.

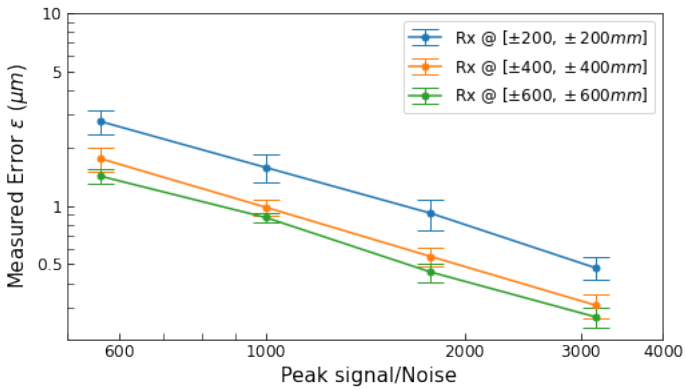

Figure 4.12.: The RMS of illumination-weighted error ϵ in deriving the reflector surfaces as a function of signal-to-noise ratio with respect to the peak of the focused beam. The three curves are the results when using different sets of receiver positions, as indicated in the legend. This simulation put the receiver in the plane that is 105mm in front of the best-focused plane.

The simulations are respectively carried out for the setup with the receiver separated by ±200mm, ±400mm, and ±600mm in each direction. Figure 4.12 shows the measurement errors for the three setups. It is found that using large spacing (±600mm) produces little errors because the large separated space of the receiver can significantly shift the phase errors produced by the two reflectors on the aperture plane. Figure 4.12 also indicates that measuring accuracy of 600mm receiver spacing is only slightly better than the accuracy of the case of 400mm receiver spacing. The designed receiver mounting structure in the telescope's cabin allows the receiver movement up to 500mm from the focal plane center. The simulations in the rest of this section use the 400mm receiver spacing. This simulation also indicates that the accuracy of < 1µm is achieved if the SNR of the holographic system is greater than 60 dB. Here, the SNR is defined as the ratio of the peak focused power to the noise, whereas the model case is for an out-of-focus beam measurement where the peak power is reduced by 20 dB. It means the required SNR of the defocused beam measurement just needs to be larger than 40 dB.

The effects of gain and phase fluctuation of the instruments are also studied. The

variations of the gain and phase are assumed to be random and have a flat spectrum. For example, the gain of the receivers changes at the level of 1 part in 100, $\langle(\Delta G_i/G)^2\rangle^{1/2} = 0.01$ (-20dB) or $\langle\Delta\phi_i^2\rangle^{1/2} = 0.01$radians ($\sim 0.5°$), these contribute the final surface errors of around 0.5µm seen the simulations results in figure 4.13. We expect that the gain and phase fluctuation in the electronics of the system should be much lower than those levels.

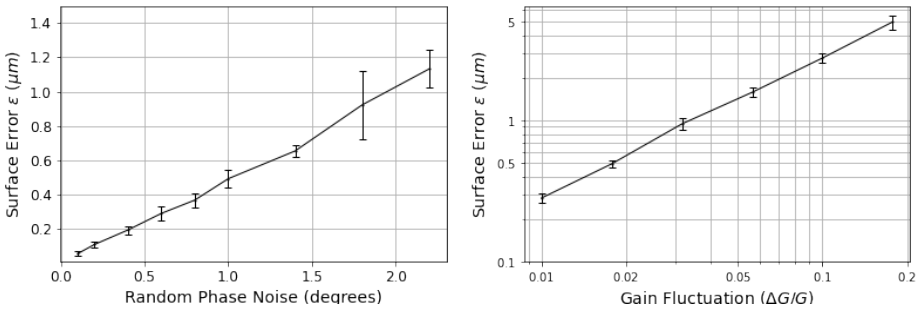

Figure 4.13.: The RMS of measured surface error ϵ as a function of random gain (right) and phase (left) fluctuations. These simulations are for the set-up with the receiver separated by $\pm 400mm$ in both directions. The receiver plane is 105mm in front of the best-focus plane

4.3.2. Effect of Atmospheric Turbulence

As the signal from the source passes through the atmosphere, the effective path will fluctuate due to variations in the refractive index of the air. At millimeter wavelengths, these variations are mainly due to differences in the amount of water vapor in the turbulent cells, particularly near the ground, but temperature differences may also play a role. For example, even on the high dry site planned for the FYST where the atmospheric pressure is ~ 0.5 bar and the temperature ~ 265 K, the total additional path due to refraction over the 300m distance is about 45mm and, if the relative humidity is 20%, the water vapor contributes about 1mm. This means that either a change in the temperature of ~ 0.6K or a change in the humidity from 19% to 21% would change the path by ~ 100µm. The path from the source to the reference receiver is, however, close to that from the source to the telescope aperture, so most of the variations will be common mode and will not affect the measurements.

To model the atmospheric phase fluctuations, we assume that they are random with a power-law spectrum with a slope of -8/3, which is expected if they are produced by Kolmogorov turbulence [89]. We can make a suitable time series by generating white noise, transforming to the frequency domain and adjusting the magnitudes to have the desired slope, and then transforming back to the time domain again. Figure 4.14 shows the power spectrum of one such series.

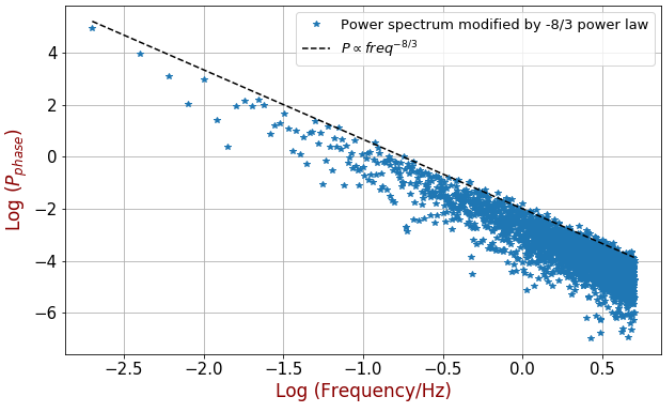

Figure 4.14.: Temporal power spectrum of the phase fluctuations assumed for simulation of atmospheric effects.

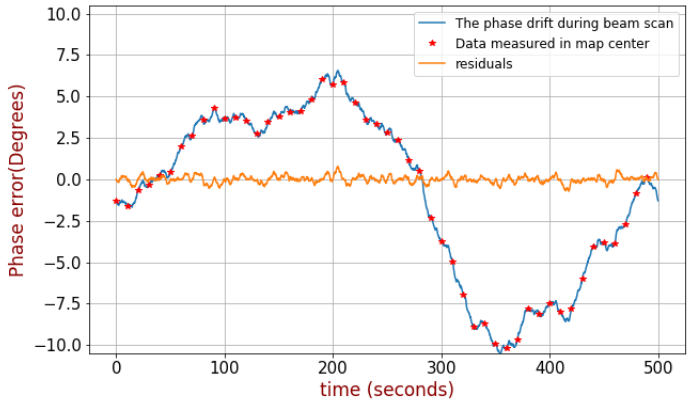

Figure 4.15.: Simulated phase error due to atmospheric variations as a function of time (blue). The data points where the beam passes through the center of the map are in red. The residuals after correction using these data points are in orange.

Figure 4.15 shows the time sequence of the phase errors. If we apply these to a model set of data and solve for the mirror surfaces, we find that the RMS error in the solution ϵ is 2.5µm. We can, however, apply the correction procedure, where we take out the more slowly varying components by using the data points taken when the beam is frequently passing over the center of the pattern. This leaves the residual errors shown as the orange line in figure 4.15. With these applied to the model data, we find errors in the solution of only 0.5µm. Although we cannot predict in advance what the magnitude of the atmospheric phase errors will really be at the site, this result demonstrates that the correction technique that we plan to use should make a large reduction in their effects.

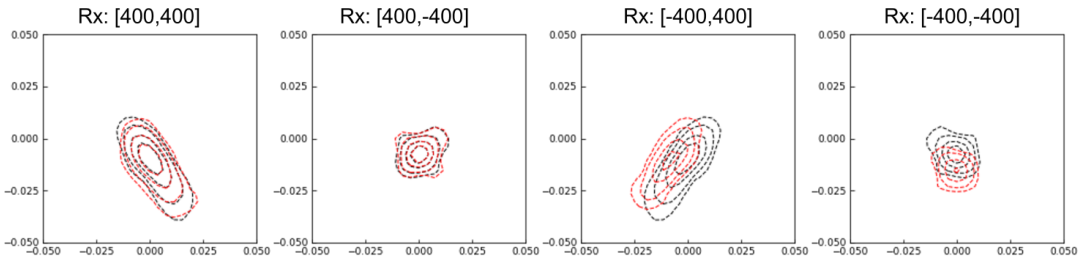

Figure 4.16.: 4 off-axis focused beams of the ideal telescope (black) and the telescope with large spatial amplitude and phase errors (red). From left to right, the large-scale amplitude, defocus, x-pointing, and y-pointing errors are introduced to the four off-axis beams separately.

4.3.3. Optical Alignment Mismatch

The practical holography system always differs from the designed model, for example, the uncertainty of the locations of the receivers or source and the inaccuracy of the their beam size. These mismatches modulate the amplitude and phase distributions of the telescope's aperture fields in large spatial scales. Section 4.2 presented how to express these amplitude and phase errors by two second-order polynomials. The coefficients of the polynomials are included as free parameters in the holographic fitting process. To check the feasibility, we plan to create these large spatial-scale errors and check if the fitting software can precisely find these errors. The input 1/e beam size of the receiver at the point [400mm,400mm] in the focal plane is changed from 0.2rad to 0.16rad to model the large spatial amplitude errors. The edge taper (the ratio of the maximum power of the aperture fields to the power of the field at the telescope's edge) is reduced by 4.88 dB. The second beam map, a receiver at [400mm,-400mm], is defocused by moving the receiver 2mm back from the designed position, then the curved phase terms are produced over the aperture plane. The receiver locations of the rest two beams are set to the points of [-402mm, 400mm] and [-400mm, -398mm] to simulate the position errors of the receiver. In order to easily see the effects of these large spatial errors on the telescope's beams, the focused optical setup is employed. The red contour lines in figure 4.16 show the beams modified by these errors. The black lines show the ideal beams.

In the fitting process of the surface analysis, we find it is better first to fit these large spatial errors in the measurement system. These errors can be efficiently found and used as the initial fitting values for the following surface analysis. The top plots in figure 4.17 show the calculated beams after the large spatial error fitting in blue contour lines. The red lines in the figure are measured distorted beam. The pointing and defocused errors in figure 4.16 have been found. After this step, the fine surface analysis is carried out and starts from the ideal mirror surface and the large spatial parameters found above.

The beams calculated by the best-fit surfaces are displayed in figure 4.17 bottom; more details of the beams are displayed. We can see the fitting beams agree very well with the measured beams. Only the first beam, which has a 4.88dB illumination error in aperture fields, doesn't agree well with the measured beam. Because the 4.88dB edge taper change is too large, the linear approximation of describing the aperture amplitude changes is not accurate enough. The practical source has about 10m 1/e beam size at the telescope and reduces the edge tape only by 0.83dB. The simulations tell that its effect on fitting surfaces is less than 0.1µm.

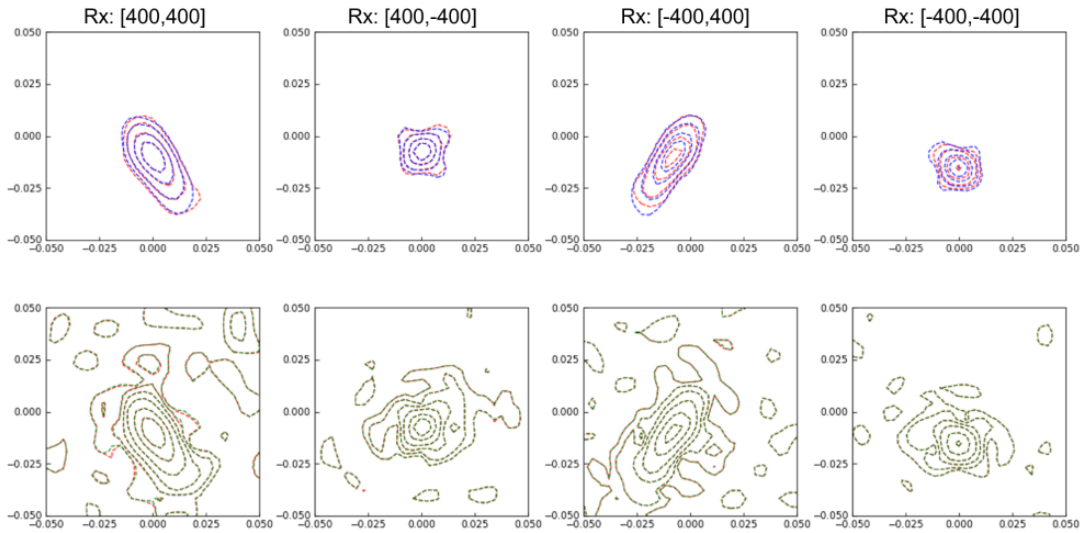

Figure 4.17.: The comparison of the observed beams (red curves) and beams calculated by fitting process. The top is the contour plot of the four off-axis beams (blue) after fitting the large-scale parameters. The bottom is the beams (green) calculated by the best fitting surfaces, and more details of the beams are displayed.

These simulations prove that the terms used to express the aperture field errors in large spatial scales are precise enough to compensate for the mismatches between the designed holographic and practical systems. In real measurement, these terms can be fitted and compared with the designed parameters; if their differences are too large, that means something is wrong in the measurement. The simulations are also carried out for the defocused holographic setup where the receiver is 125mm before the focus, which indicates the same measurement accuracy.

4.3.4. Telescope Pointing Errors

We now consider the effect of the telescope pointing inaccuracy during beam scan. The telescope pointing errors may result from servo tracking errors or telescope deformations

due to a slow change of centrifugal forces or temperature with time. We simulate the pointing errors by assuming that each sample in the observed maps is shifted by random distance δEl, δAz from the expected position in elevation and azimuth directions. These pointing offers are simulated with a 'random-walk' process which calculates the accumulative sum of Gaussian random variables to get random variables, and the RMS of the new random data is modified to the designed level. We expect that the pointing errors will be small and assume the telescope pointing direction will not offset too much from the commanded position, so the mean of the simulated pointing errors is removed. Figure 4.18 shows the measured surface errors as a function of the RMS of the pointing errors. It is found that the accuracy of the is quite sensitive to pointing errors. 2 arcseconds RMS (6 arcseconds peak-to-peak) of pointing error degrades the measurement accuracy by around 4.5µm, which is already higher than the required $<$ 2µm measurement accuracy.

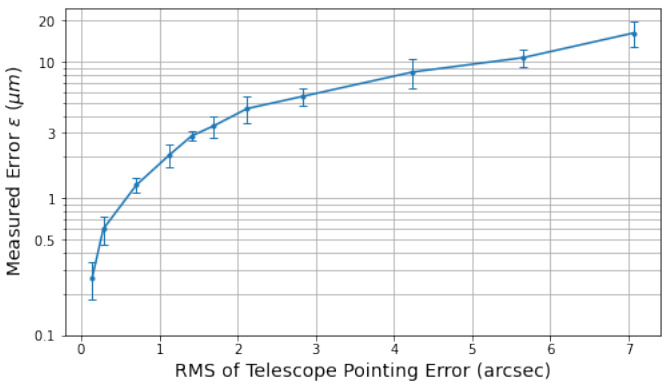

Figure 4.18.: The RMS of the measurement surface accuracy ϵ as a function of the RMS of the telescope 'random-walk' pointing errors.

The actual situation of the pointing error is not as bad because the telescope's pointing position can be read by the encoder. The readout from the encoder is much close to the actual pointing position. In case there is a large pointing error in the future measurement system, the actual telescope scanning path needs to be measured. After the holographic analysis, we plan to implement additional fitting processes called the 'outer loop'. After the surface analysis, we believe most surface errors of the telescope have been discovered, although the results are not accurate enough. The solved reflector surfaces are fed into the model in the holographic software. We express the trajectory of the telescope in the time series by the sum of a set of the Fourier series. Then the holographic software is employed to fit the Fourier series coefficients to find the actual telescope scanning path. It was found that the measurement accuracy can be significantly improved by

repeating this process twice. Figure 4.19 presents the simulated telescope variations in the elevation angle of one scan. The fitting scanning path can compensate for most of these deviations. The derived scanning path is fed into the holographic software, and a new surface error analysis, in turn, is taken and results in a measurement error of $< 1.5\mu m$.

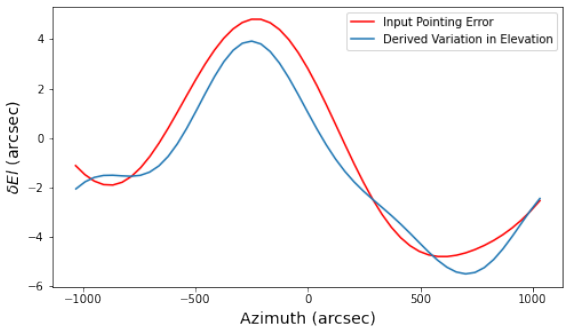

Figure 4.19.: Simulated telescope pointing error in elevation angle for an azimuthal scan (red) and the derived elevation changes (blue).

4.3.5. Effect of Panel Fabrication Errors

The manufacturing accuracy of the panels is one dominant surface error source of the telescope. Figure 4.20 shows an overview of the panel fabrication errors measured by the coordinate measuring machine (CMM). The average RMS of the errors is less than 3µm (2.77µm in M1, 2.82µm on M2). This section studies the effects of panel manufacturing errors on the accuracy of the fitting movements of the panel adjusters.

Assuming the panel adjusters are located in the ideal positions, and only the panel fabrication errors exist on the reflector surfaces, we employ the holographic analysis to the measured beams. As expected, a set of non-zero adjuster movements are found to describe the surface errors. The analysis software uses the model with perfect panel surfaces to find the best adjuster movements to express the panel fabrication errors. But using five adjusters cannot precisely describe the detailed panel surface roughness. Numerical simulations tell us that the RMS of the surface errors over the entire mirror can be improved from 3µm to 2.5µm after applying these non-zero values to correct the panel deformations. It means panel surface roughness will not affect the accuracy of the holographic system; instead, the errors would be measured and compensated by turning panel adjusters.

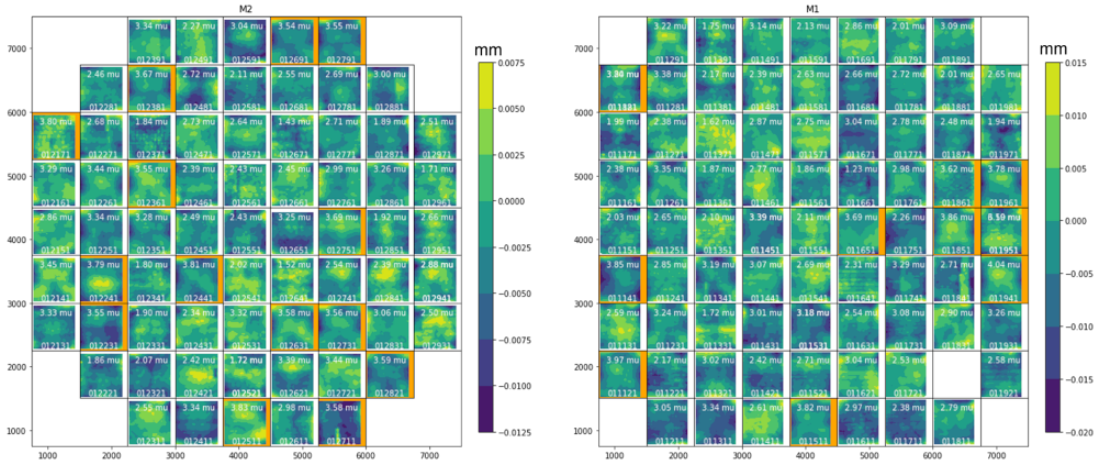

Figure 4.20.: Summary of the measured surfaces of the panels on M2 (Left) and M1 (right), the panel number, and RMS of the errors on each panel are written. Panels highlighted in orange have an RMS greater than 3.5µm.

4.3.6. Summary and Error Budget

The feasibility of the Multi-map holography measurement and the developed software technique has been proven by numerical simulations for the FYST telescope. The effect of several errors in the FYST holographic system on measurement accuracy and the optimal observation approach to minimize these effects are also investigated. It was seen that the new software analysis technique could compensate for the error caused by a mismatch between the practical system and the built model in the analysis software, and the manufacturing error on each panel would not degrade the final measurement accuracy. The most sensitive factor of degrading measurement accuracy is the telescope pointing error. Fortunately, the scan trajectory of the telescope can be analyzed by the fitting program if the relative pointing errors of the telescope are not much significant. The contribution of the above measurement errors to the holographic measurement accuracy is summarized in table 4.1. These simulations indicate that a measurement accuracy of ~ 2µm is achievable.

Error Source	**Surface Error ϵ**
Receiver noise ($SNR < 65\ dB$)	$< 1\mu m$
Random gain fluctuation ($\Delta G < 0.01$)	$< 0.5\mu m$
Random phase changes ($\Delta\phi < 1$)	$< 0.5\mu m$
Atmosphere turbulence after calibration	$0.5\mu m$
Pointing errors (Max 6 arc second)	$< 1.5\mu m$
Others (e.g,. phase error of Feedhorn)	$< 1\mu m$
Total	$< 2.2\mu m$

Table 4.1.: Summary of the measurement errors in the FYST holography system.

4.4. Star Sampling Pattern

The conventional holography technique uses the Fourier transform to analyze the measured beam, which requires sampling the beam map in rectangular grids. This limitation demands the telescope to scan the source row by row or use other scanning modes but regrids the data series to the required grids. The data regridding may create spatial errors, which is the inaccuracy of the telescope pointing directions. In addition, it is also necessary to apply the calibration process during the telescope scan to correct the effects of the drift of the instruments and the fluctuations of the atmosphere. The calibrations are usually done by frequently moving the telescope to look at a fixed point and recording the fields of this point in amplitude and phase. So the fluctuations can be tracked and removed from the measured data. To implement this, additional motions of the telescope are required, and this will reduce the ratio of the valid data during the measurement.

Fortunately, the new holographic analysis technique doesn't require the points to be on a regular grid with uniform coverage of the beam map area. Therefore, the data can be arranged in any pattern, which can easily achieve the data calibration procedure with keeping good data-taking efficiency. One example is to use a 'star' pattern [96], which moves the telescope in a straight radial line, with each motion passing the nominal on-axis position. Figure 4.21 blue dots show a radial scan pattern that has 50 radial slices with 3.6° interval, and 72 points sample each slice. This pattern results in a sampling biased toward the center of the beam, where the fields are sampled more densely than the outer region. The center part of the telescope beam has higher gain compared to the outer region, and we thought these regions include more important information to resolve telescope mirror surfaces.

The gray curve in figure 4.21 is a regular raster scan pattern that includes 61-row scans with 61 data points per line. So the valid observing time and noise in the measured

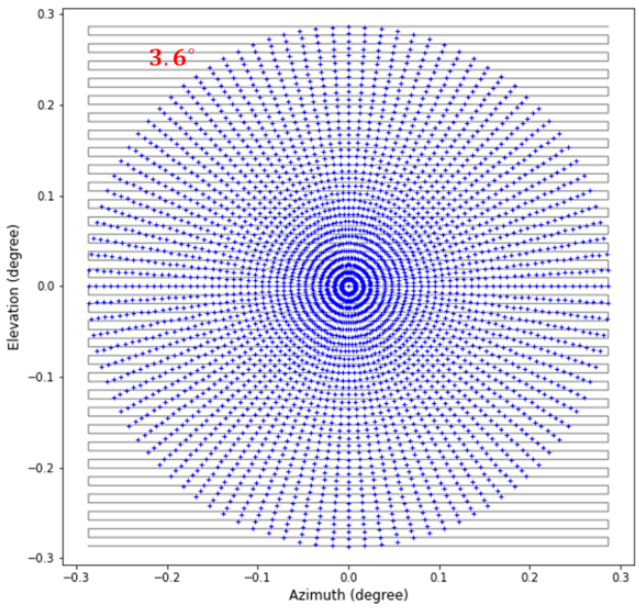

Figure 4.21.: Telescope scan patterns, the radial data sampling pattern with 50 radial slices 3.6 degrees apart in azimuth (blue dots) and 72 points in each slice, and regular square raster scan with 61-row scan, and each scan contains 61 sampled data points.

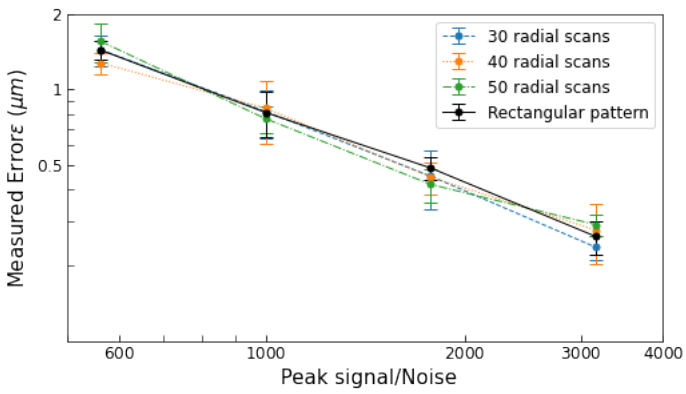

Figure 4.22.: The RMS of illumination-weighted error ϵ of the fitting mirror surfaces as a function of the peak signal-to-noise ratio for the case using different scan patterns. The black curve uses a regular square pattern with 61-row scans and 61 points in each line. Other colorful curves are the cases of 'star' scan patterns with different radial scan numbers.

data are the same for the two scanning patterns. The simulations indicate that the accuracy of the solved surfaces of the reflectors is the same for the cases using the two scan patterns with the same noise in the measured beam maps. The simulated results are shown in figure 4.22. We also checked the effect of the slice numbers by using 50, 40, and 30 scans in each beam pattern but keeping the total number of sampling points and signal-to-noise ratio, simulated measurement error as a function of the signal-to-noise ratio of the beam is also plotted in figure 4.22. The effects of the errors described in previous sections were also checked for the case of using this 'star' scan pattern by numerical simulations, which gave the same level of measurement accuracy. Due to the sequential nature of the studies, the results in the preceding sections still use the rectangular scan pattern.

4.5. Summary

In this chapter, the new holographic technique for surface diagnosis of a 'two-reflector' system, which is named as 'Multi-map' holography method, has been developed and verified by numerical simulations for the FYST telescope. In the first part of the chapter, surface error degeneracy between two reflectors of the FYST telescope was explained, and it was emphasized that measuring and correcting the surface errors for both reflectors was very important to preserve the optical performance of the designed telescope. In the second part, the new multi-map holography approach and the new data analysis technique were proposed and developed. Then the feasibility and accuracy of the new method were verified by numerical simulations. The effects of different types of errors in the measurement system on the accuracy were also investigated. The optimal configuration, measurement approach, and analysis flow were explored to optimize the measurement accuracy. This study concludes that the novel multi-map holography can successfully discriminate surface errors on the two reflectors of FYST by observing five different beam maps, and the measurement accuracy of $\sim 2\mu m$ is achievable. In the next part, the multi-map holography and the new software technique will be implemented on a small Crossed-Dragone antenna to check further the feasibility of the method and the accuracy of the designed holographic hardware for FYST.

Chapter 5.

The FYST Holographic System

Based on the holographic design and the study of the 'Multi-map' holography technique described in the preceding chapters, the details of the FYST holographic system are presented. The chapter begins with the holographic hardware which is designed to satisfy the required surface accuracy and spatial resolution. Then the setup of the holographic measurement and the data pre-processing procedures are described to get the telescope's beams. Finally, the holographic analysis flow is explained.

5.1. Hardware Design

We now describe the hardware design needed to make the FYST holographic measurement. The diagram of the electronic schematic of the holographic system has been illustrated in figure 3.7. There are four main modules: 1) the source (transmitter) that will be mounted on a steel tower on the shoulder of the mountain, about 20m higher than the telescope and 300m away; 2) the signal receiver, which is supported by a frame close to the focal plane; 3) the reference receiver mounted on the telescope's yoke, immediately below the telescope aperture, where it has a direct view of the source; 4) the digital correlation receiver housed in the electronics space inside the yoke. These modules were designed, assembled and tested by our collaborator in Universidad de Chile to meet the holographic requirements that were summarized in Table 3.3 in Chapter 3. The specification of the receiver and source are given in Table 5.1.

The modules of the source and the receivers are all enclosed in temperature-controlled boxes to provide stability and protection. The local oscillator (LO) signals shown in figure 3.7 for the two receivers are derived from a common microwave reference at 12.32GHz which is also located in the electronics space. Since coherence during the measurement is paramount, identical high-quality and phase-stable cables will be used to carry this reference signal to the two receivers. The rest of this section will present these modules' optical design and electronic parts.

	Source		Receiver	
			Reference	Signal
Frequency	295.74GHz	LO Frequency (×2)	295.68GHz	295.68GHz
Beam FWHM	1.8°	Beam FWHM	1.1°	16°
Frequency Stability	1×10^{-9}	Noise temperature	$< 5800\ K$	$< 5800\ K$
Output power	> 100µW	IF Frequency	60 MHz	60 MHz
Phase noise @ 1kHz	-80 dBc/Hz	Channel Bandwidth	8.2kHz	8.2kHz

Table 5.1.: The specifications of the FYST holography hardware.

Feed Horns

The same design of profiled diagonal horn [97] was used for all three radio frequency (RF) modules, the source and two receivers. The horn of the signal receiver illuminates the telescope directly, whereas the source and the reference receivers contain additional optics to provide narrow well-defined beams, which serves both to increase the power level of the signal and to reduce unwanted reflections.

This horn design was chosen because it is relatively simple to machine but has good properties for our application. The half-power beamwidth (HPBW) is around 16°, which was chosen to provide an edge taper of 7dB on the telescope. This relatively modest taper enables us to measure the outer parts of the reflectors accurately. The equivalent beam waist of the designed horn is around 1.4mm at 295.74GHz. The sidelobes are more than 20 dB below the co-polar maximum and the peak cross-polar components are below -25 dB. We have manufactured the horns and verified their compliance with the predictions of electromagnetic modeling by measuring the pattern at 296GHz in the laboratory, using the planar near-field technique. The reconstructed far-field complex (amplitude and phase) beam of the horn is shown in figure 5.1.

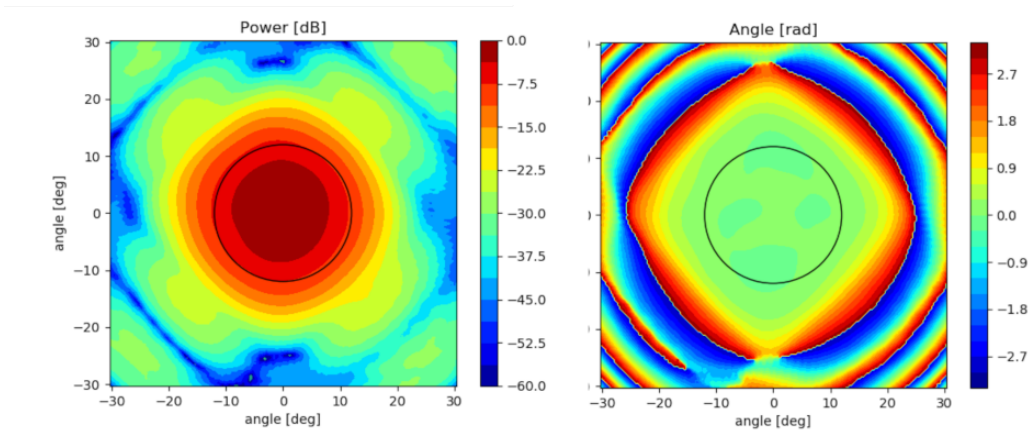

Figure 5.1.: Radiation pattern of the conical-spline horn. The black circle represents the edge of the 6m telescope aperture.

Source Module

The 295.74GHz signal is produced by multiplying a 16.43GHz dielectric resonance oscillator (DRO) in two stages - the first active and the second passive. The DRO is in turn locked to a GPS-disciplined 10MHz oscillator. The combination is designed to provide a stable signal with low-phase noise. The components making up the source are shown in figure 5.2. All these components were obtained from commercial sources.

The feed horn illuminates a small off-axis parabolic mirror producing a beamwidth of 1.8° FWHM, which means that its output beam is $\sim$ 10m wide when the output beam reaches the telescope. This beam size is chosen as a compromise between making it small to minimize the chance of reflection from the ground between the source and the telescope and making it large to ensure that the wavefront across that telescope aperture is spherical. After reflection off a flat mirror, which is used to align the beam, the signal passes through a hermetic window, which is tilted to avoid reflections. Figure 5.3 shows the optical layout of the source and its CAD model.

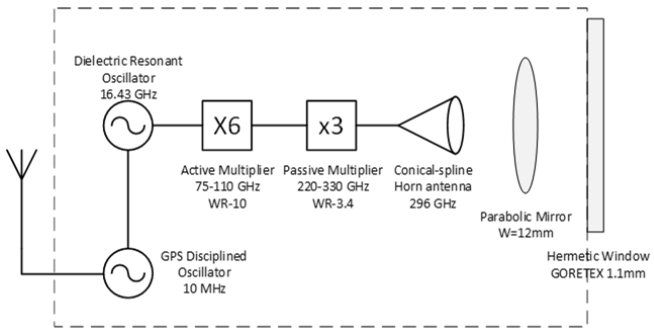

Figure 5.2.: Schematic of the source.

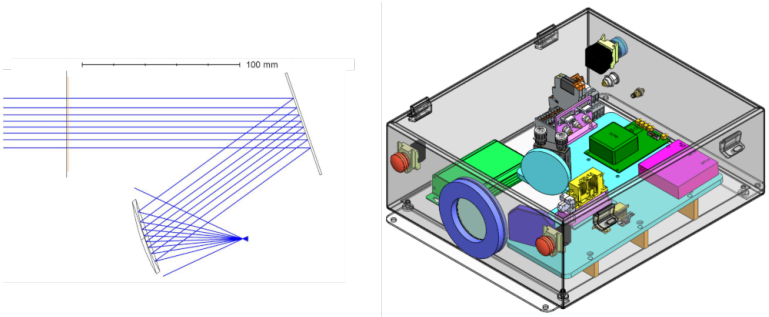

Figure 5.3.: Left: The optical layout of the source module; **right**: the view of the source CAD model.

Receiver Modules

The two receivers contain almost-identical RF modules. The main components are shown in figure 5.4.Each module contains a horn, a sub-harmonic mixer, an active multiplier

chain for the LO, and amplifiers for the LO and IF signals. Apart from the horn, these are again commercially available devices. The LO frequency is 147.84GHz, which means that the IF frequency is 60MHz. The signal and reference receiver modules differ only in the amount of IF gain, which is determined by the peak signal level expected. The use of an ambient-temperature sub-harmonic mixer means that the noise temperature is relatively high, $\sim$ 5.000K but, because we have a relatively powerful source that is quite close and there is a substantial amount of gain in the optics, this is sufficient to give a signal-to-noise ratio of more than 70dB. For this application, simplicity and stability are more important than sensitivity. To assist in this, the components are again mounted on an isolated, temperature-controlled plate and enclosed. See figure 5.5.

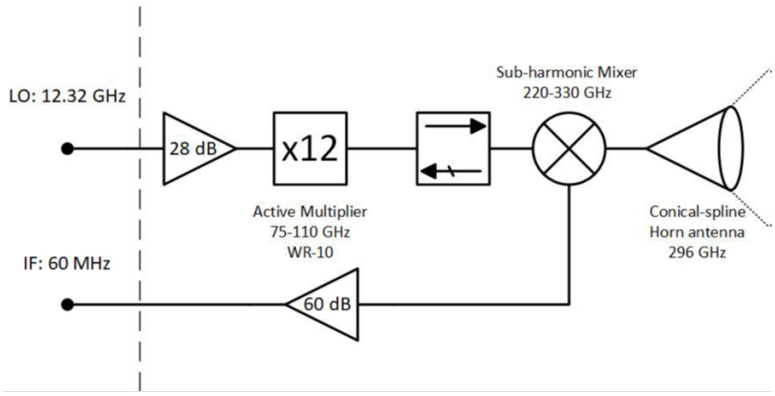

Figure 5.4.: Schematic of the receiver module.

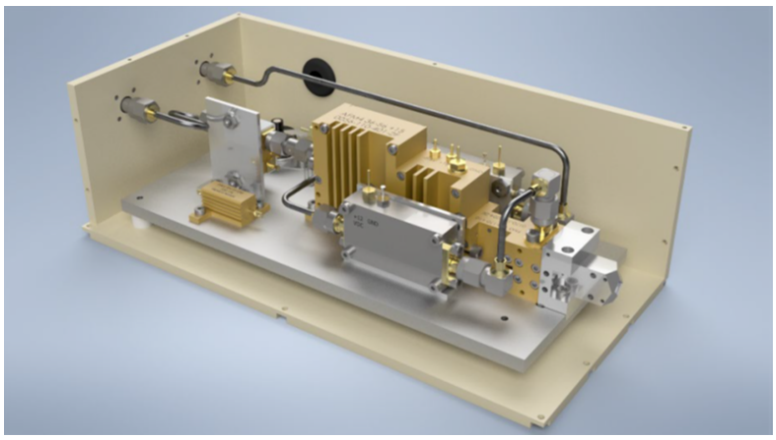

Figure 5.5.: View of receiver module with part of the cover removed.

The signal receiver to sample the signal in the focal plane is supported by a stiff frame which will be erected in the instrument space when measurements are to be undertaken,

see figure 5.6. The receiver module sits on one of a set of mounting points on this frame, chosen to give the required coverage of the focal plane.

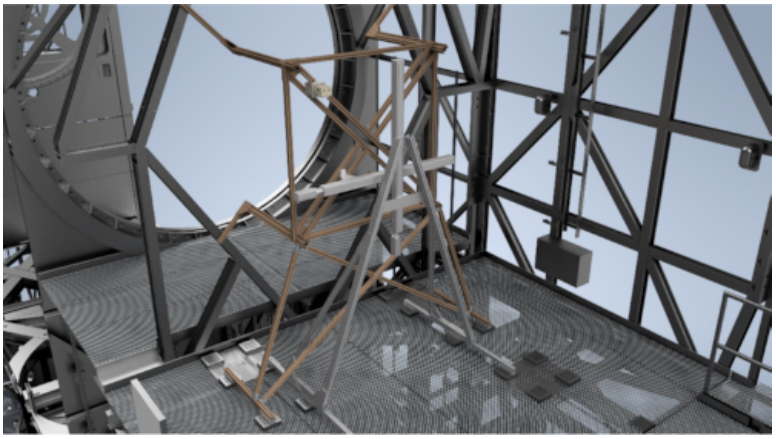

Figure 5.6.: The mount for the receiver in the telescope focal plane, showing the support frame (brown) and the X-Y stage (light grey).

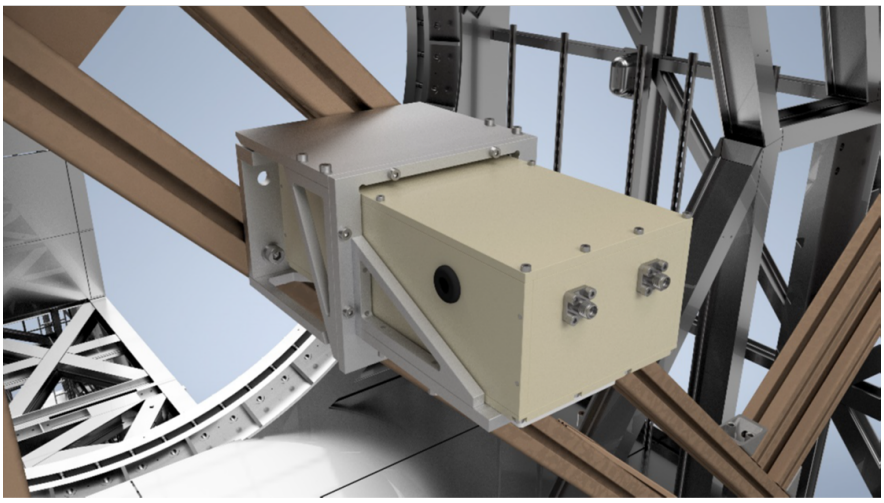

Figure 5.7.: Close-up view of the signal receiver module at one of the mounting positions.

There is a motorized X-Y drive behind the frame that can pick up the receiver module and move it from one mounting point to another under remote control. This should take less than a minute. The support of the receiver module is kinematic to ensure that it can be moved and replaced with repeatability. The locations of the mounting points can be changed (manually) if we find that a different spacing is necessary. In addition, the mounting frame can be moved nearer or closer to the focal plane to change the amount of defocus.

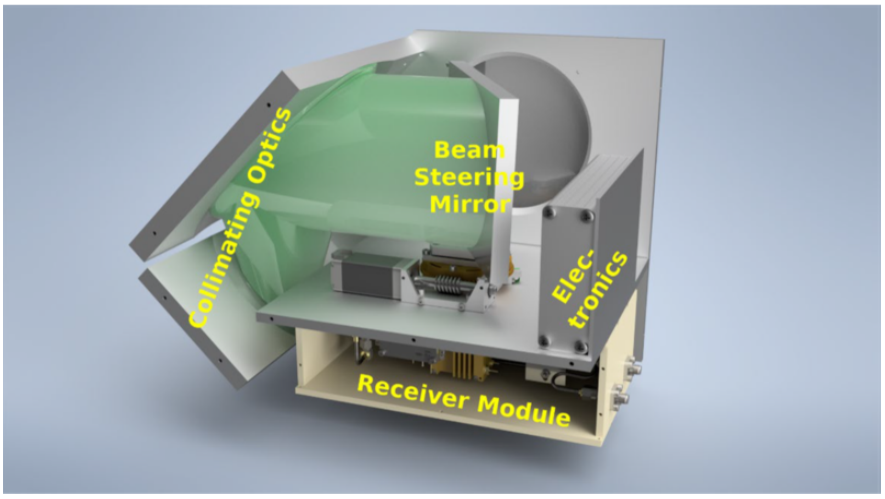

Figure 5.8.: Cut-away view of the reference receiver.

The reference receiver, which will be mounted directly on the structure of the telescope yoke to ensure a stable attachment, contains the second receiver module and optical components. See figure 5.8. Two off-axis mirrors produce a collimated beam with a FWHM of 1.1°. This is again a compromise between making the beam narrow, to reduce reflections and increase the signal level, and making it wide so that the change in phase and amplitude during the scanning movement, which will typically be $\sim 0.6°$. The optics was designed based on Gaussian optics theory, and mirror parameters and optical performance are shown in appendix B. A third flat mirror is mounted on a motorized rotation stage which directs the beam at the source. The rotation is controlled remotely over an Ethernet connection. This is needed because the telescope azimuth at the center of the scan will change when we move the signal receiver to a different position in the focal plane (by about 1.6° for a 400mm offset). We can also make a small scan with this stage, while keeping the telescope stationary and pointed at the source, to calibrate the phase and amplitude of the reference system as a function of azimuth. The mirror can also turn the beam in the opposite direction so that we can make measurements with the telescope flipped "over the back", which will be important for testing whether the deflections in the telescope mirrors due to the force of gravity are consistent with the designers' predictions.

Digital Back-end Correlator with high spectral resolution

We need to measure the amplitude and phase of the signal that has come via the telescope reflectors relative to that from the reference receiver. Since we are using a coherent source it is advantageous for us to make this measurement using a narrow bandwidth. We do this using digital rather than analogue techniques which provides more flexibility and, most importantly, guarantees that the signal and reference are treated

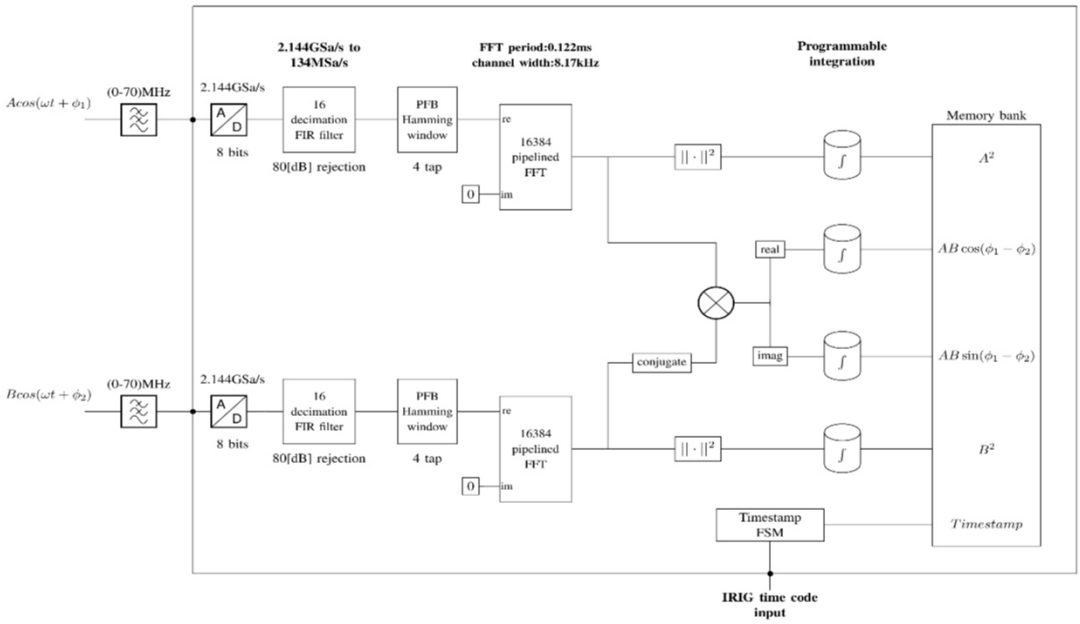

Figure 5.9.: Diagram of the digital back-end correlator. The architecture consists in a FX correlator with an oversampling and decimation stage. Concurrently a timestamp subsystem based on the IRIG protocol is running.

in an identical way. Our approach is to use a dual-input high-resolution spectrometer, essentially acting as a narrow-band filter on the signal and reference, followed by digital multiplication and integration stages. This has been implemented in the Reconfigurable Open Architecture Computing Hardware 2 (ROACH2) platform, composed of two 8-bit high speed analogue to digital converters (ADCs), a Virtex6 FPGA and a PowerPC 440 microprocessor. Figure 5.9 shows the configuration of this subsystem. We run the ADCs at a high rate, $\sim$ 2GS/s, and then reduce the sampling frequency by a factor of 16 using a polyphase decimation FIR filter with 80dB of rejection, which gives us a usable bandwidth of 67MHz and reduces the quantization noise by $\sim$12 dB. The resampled data are then passed through a pipelined FFT using a polyphase window, which provides high isolation between spectral channels and a relatively flat frequency response within a channel. We fine-tune the ADC sampling frequency to place the signal in the middle of a channel. We then select the real and imaginary outputs from this channel and form the cross-product and the magnitudes. These are produced at a rate of $\sim$8.2kHz and integrated for a selectable time, typically between 1 and 20ms. The data are stored in the internal memory of the PowerPC for post-processing offline.

Concurrently, we run a finite-state machine to provide timestamps so we can align the data samples with the corresponding telescope pointing position. The timestamp subsystem is calibrated using an Inter-Range Instrumentation Group (IRIG) time code

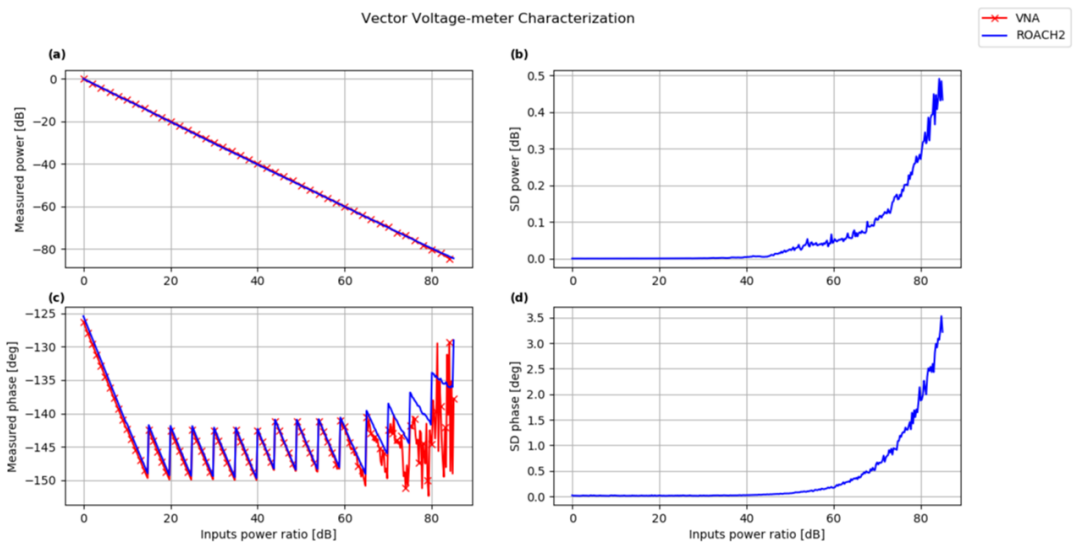

Figure 5.10.: Characterization of the vector voltage meter system. ROACH2 measurements in blue and VNA measurements in red, for input difference in the range (0-85) dB. (a) Average power difference; (b) ROACH2 standard deviation for the power differences; (c) Average phase difference; (d) ROACH2 standard deviation for the phase differences.

signal fed by the observatory's master clock and uses each pulse of the IRIG packet to update its internal value, ensuring that the system is locked to the master clock with a time resolution of 957ns.

We have run numerous tests on this system, of which one is illustrated in figure 5.10. Here we compare the results from our system with those from a commercial vector network analyzer (Keysight E8364C VNA). We use two signal generators locked to the same frequency, keeping one at a fixed power level (to represent the reference in the holography measurement) while making a sweep in the power level of the other (to represent the signal). Note that the relative phase of the two outputs will alter as the power level is changed because of the switching of the internal attenuators: this is seen in the results – figure 14c. The signals from the two oscillators are split so that we can make measurements simultaneously with the ROACH2 system and the VNA. With the ROACH2 system we collect 128 measurements and calculate averages and standard deviations producing the blue curves in the plots. The red curves are the VNA values. We find that the agreement is better than 0.2 dB in amplitude and 1° in phase when the ratio of the powers is in the range 0 to 65dB. At lower power levels differences start to appear, but the VNA values become noisy. These results do however confirm the accuracy of our system over a larger dynamic range than we need. The measured standard deviations (figure 5.10 b and d) represent an upper limit on internal random errors due to things like round-off in the ROACH2 system. These are well below the

levels that would affect our measurements.

5.2. Beam Measurement and Data Analysis Procedure

In this section, we describe the procedure of measuring the FYST holographic beam maps using the developed measurement system. Based on the numerical study in chapter 4, the optimal beam measurement steps and data analysis procedure are also presented. The numerical simulations tell us that five complex (amplitude and phase) beam maps of the FYST telescope are needed to be measured by putting the signal receiver to 5 separated points in the focal plane (the center of the field and the corners of a square with 800mm side). Each beam map has to be sampled in an angular range of $\sim 0.6°$ to obtain the required 100mm spatial resolution in the resolved mirror maps. We plan to measure the beam pattern over a region about 0.7° in extent. Since the inference data analysis approach doesn't require sampling the beam map in regular grids, we plan to use a radial scanning or star-scan pattern, where the telescope can repeatedly pass to the map center and record the amplitude and phase. These data measured in the map center will be used to calibrate the atmospheric fluctuations and the drift of the holographic instruments.

Figure 5.11 shows one completed scan trajectory of the star scan pattern for the FYST holography measurement. The scanning angular range is 0.7° which is slightly wider than that used above simulations. Each scan takes 7 seconds on the straight sections and 3 seconds on the turn-around path, so one full map scan will take 500 seconds. Actually, the turns can be executed as quickly as possible without exciting vibrations in the telescope structure because the data recorded in these periods will not be used for data analysis. The efficiency of the observing time can achieve about 70%. It means the fluctuation of the measurement system can be calibrated and corrected every 10 seconds.

Since the designed artificial transmitter is close to the telescope and reference receiver, a high enough signal-to-noise ratio, for example, $> 50dB$ using 0.15ms integration time, is obtained, we adopt the 'on-the-fly' (OTF) measurement mode, telescope continuously scans the source, and the back-end digital voltage meter samples the beam patterns in high rate. The telescope pointing position is recorded by the encoder on the telescope at a rate of 200Hz, and read position values and sampled beam data are synchronized using a time reference or timestamp. The recorded encoder values are interpolated to find the actual pointing positions a the times when the field points were measured. In the case of the FYST holography system, the scanning speed is about $0.1°/s$. The smallest angular size required in the measured beam is about $< 0.01°$ that is set by the beam size of

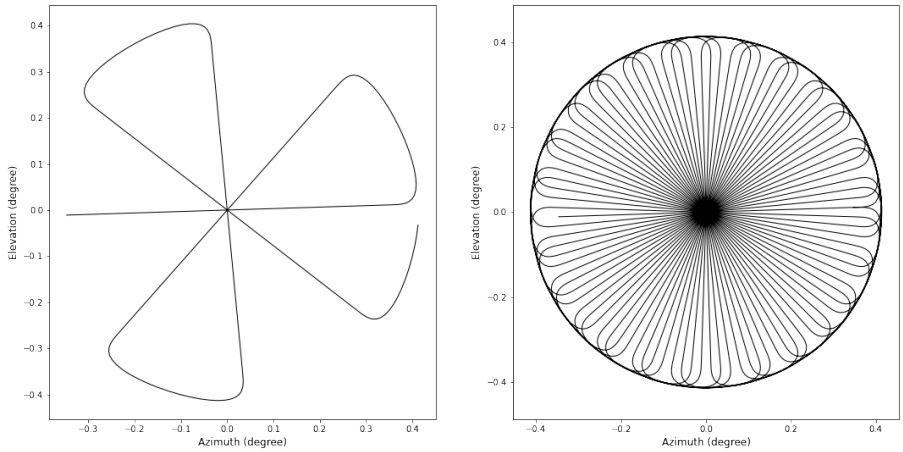

Figure 5.11.: A possible star scan pattern for the FYST holography measurement. Left is the first 4 scans, and right is the designed full pattern with 50 scans. The line is the trajectory of the telescope pointing position.

the telescope which is the ratio of the operating wavelength to the telescope aperture size. So, we only need about 10 data points per second to sample the beam pattern. However, to avoid smearing the data along the scan, we will oversample - e.g., we set the integration time in the digital back-end to ∼0.01s giving ∼ 100 points per second. The highest sampling rate of the designed back-end voltage meter is about 8.2kHz. Based on the above setup, the beam measurement process, including the calibration step and data pre-processing, is summarized in the following steps:

1. Correct amplitude fluctuations of the source. Since the quantity that we need in order to have a result that is independent of amplitude fluctuations in the source is the ratio of the output of signal receiver denoted by A in figure 5.9 to that of reference receiver expressed by B. The recorded voltage product of the two outputs is divided by the power of the reference channel, which is expressed by $A \times B/|B|^2$.

2. Measure and correct the amplitude and phase pattern of the reference receiver as a function of telescope azimuth. The reference receiver is placed in the yoke of the telescope, and its pointing direction changes in azimuth during the telescope scan. Its Gaussian amplitude beam and non-constant phase pattern will modify the telescope's beams. This effect can be calibrated if we know the exact beam pattern of the reference both in amplitude and phase. Therefore, before the holographic beam measurement, we fix the pointing direction of the telescope and scan the reference receiver beam by rotating its flat mirror to measure its beam in azimuth.

Since five beam maps are required with different pointing directions, the reference beam measurement has to be carried out before each beam measuring. We label the measured reference beam as $B_{ref}(\phi)$, where ϕ is the azimuth angle. In this step, the signal receiver works as a reference. Following the correction described in item 2, we can express the measured reference beam as $B_{ref}(\phi) = A \times B/|A|^2$. After this, the telescope's beam is recorded by dividing the measured beam by $(B_{ref}(\phi))$.

3. Smooth the recorded data. After the correction step, the recorded data is smoothed using a sinc function. The width of this sinc function is chosen to make sure that all the actual structure in the pattern is preserved, but the noise on the samples is reduced as far as possible. In principle, it is unnecessary to smooth the data, using the inference approach, we can calculate the complex fields of all recorded map points and compare them with the measured data. But this slows down the beam calculations and costs more computation resources. Consequently, the smoothed data is resampled at coarser intervals (Nyquist sampling) so that we do not have to process an unnecessarily large number of samples in the later data analysis.

4. Remove the systematic amplitude and phase drift using the field points at the center of the map. The data from each radial scan is interpolated to find the amplitude and phase of the center point. Ideally, these values would all be the same, but in practice, there will be drifts from scan to scan due to changes in the instrument and, probably more significantly, in the atmospheric path between the source and the telescope. (It is of course only the differences between the atmosphere along the path from the source to the telescope aperture and that along the path to the reference receiver that matter). Then we get the field changes as a function of time, fit a suitable smooth function of time to the amplitude and phase of the field at the center points, and adopt these as representing the drifts that occurred during the course of making the entire beam map. We then use these fitted functions to correct the observed data.

Surface error analysis

When we get the corrected beam maps, using the inference technique described in chapter 4 we can convert these beam maps to two surface error maps. The basic data analysis flow has been explained in figure 4.6. In the practical experiments, some modifications are required for different measuring purposes. The points are listed below:

1. The telescope model has to include the beam pattern of the feed horn in the signal receiver model. The numerical simulation used in the previous section assumes

that the receiver feed horn beam is ideal Gaussian and has a spherical wavefront. Any wavefront errors of the practical feed horn will be transferred to the final analyzed reflector surfaces. We do not think that we can measure the horn phase pattern well enough for the holographic purpose. So we will rely on the theoretical modeling of the horn for this. The measured beam pattern of the profiled diagonal horn shown in figure 5.1 do confirm that the horn basically works as expected, and we are confident that the phase must be very smooth on small and medium angular scales because the physical dimensions of the horn aperture are small in terms of the wavelength. We can check for phase errors on large scales by, for example, making measurements with the horn rotated to different angles about the line of sight. We can use a set of Zernike polynomials to express the wavefront of the feed horn and fit their coefficients to study its wavefront errors.

2. Analyze large spatial errors of the holographic system. Telescope misalignment and inaccuracy of beam size of the source and the signal receiver in the software model create amplitude and phase errors over telescope aperture in large spatial scales. The effect of these errors on telescope beams is obvious, assuming telescope mirror shapes are ideal, first fitting these errors can significantly reduce the residual of simulated beam and observed beam. This step is very fast because of the few fitting parameters and beam calculating loops. Then using fitted results as the initial values for the following mirror surface analysis can reduce the fitting time and avoid the algorithm from choosing wrong fitting paths.

3. Fit mirror surface errors. Since the parameters of the fit are the deviation of the points of panel supporters, these values can be used directly to make the adjustments required to bring the surfaces to the desired shape.

4. Check telescope scanning trajectory. The above analysis assumes that the telescope's pointing is stable throughout the beam scanning. In the practical, telescope moving may have glitches. The pointing position would be different from the expected position. To check the trajectory errors, after the surface error fitting, we can look at the residuals, the difference between the measured data and the beam of the best-fitting models, to see if there is evidence for trajectory errors. If there is, we can build a model to express the telescope moving errors as a time function. Using the fitted surfaces as the telescope model, we can fit the telescope tracking errors. Corrections to this pointing error could then be made, and second iteration of the surface solution carried out. This step has been explained in section 4.3.4.

5. Repeat the holographic analysis and reflector corrections. The adjustment of the reflectors is unlikely to be perfect in a single step, especially if the initial errors are large: amongst other things some of the approximations in our model require that the errors be small compared to the observing wavelength. The adjustment process will be converged after a small number of iterations.

6. Other cases. If we want to monitor the mirror deformations, e.g., as a function of temperature or over time, it is more convenient to fit for the surface shapes as a sum of polynomials. This will give us numerical values for errors of various forms, such as astigmatism, and can be used to make images of surface deformations. Note that, because we are using a source at a fixed elevation, we cannot measure the changing effect of gravity on the structure as the telescope is pointed to different elevations. It is however possible to flip the telescope over and turn the azimuth through 180 degrees so that it again points at the source. This essentially reverses the gravity vector with respect to the reflectors. Hence, we should be able to check whether or not the response to this component of gravity is as expected.

Chapter 6.

Holographic Test for a Small Crossed-Dragone Antenna

In the preceding chapters of this thesis, a new holographic metrology has been built upon which to measure the surface errors of the reflectors of FYST. The optimal setup and detail of the data analysis procedure are studied with numerical techniques. In this chapter, the new metrology is utilized for a small Crossed-Dragone configuration antenna in the laboratory to demonstrate the feasibility and accuracy of the new method. The details of the experimental setup and design are presented. The conventional holography analysis is compared with the new multi-map holography analysis in order to validate that the new technique can break the surface error degeneracy and discriminate the surface errors in the 'two-reflector' system.

6.1. Overview the Holographic Testbed

6.1.1. Small Laboratory Antenna

A small Crossed-Dragone antenna, hereafter called the Lab antenna, was designed and constructed to test the feasibility of the novel FYST holography system. These include checking measurement surface accuracy, designed spatial resolution, and the ability to discriminate surface errors between two reflectors. The simple case is to shrink the whole FYST holography system, including the antenna model and the requirements of the holographic measurement, and the instruments developed for the FYST holography measurement are used for the laboratory test. This means the operating wavelength λ of the holographic test is still ~ 1 mm, and the Lab antenna offers a broad beam size compared to the FYST telescope. Its beam map must be measured in a wider angular range than the FYST holographic measurement to achieve the scaled spatial resolution.

The Lab antenna with 400 mm aperture size is used because the reflectors with this size can be manufactured precisely in-house. Simply shrinking all the dimensions of the 6-meter FYST telescope by a factor of 15 can produce a model with this aperture size. Then we get a spacing of 400 mm (L_m) between its two reflectors, a distance from M2 to the focal plane, $L_s = 800$mm, and an effective focal length $f_{eff} = 960$mm. Figure 6.1(a) shows the optical layout of the scale model. However, the edge of its two reflectors marked by red circles in Figure 6.1 may cause clearance problems, because the Lab holographic beam needs to be measured in a wide angular range. Ideally, the incoming light from the sky is reflected by M1, in turn, delivered to the receiver by M2. But for the off-axis beam measurement, the incident light is first scattered by the edge of M2. The scattered fields are reflected by M1 and M2 to the receiver, significantly affecting the receiver response. To improve the clearance, the distance of the two reflectors is increased from 400 mm to 450 mm, keeping the reflecting angles of the on-axis light. The optics is modified to satisfy the Mizuguchi-Dragone condition. The details of the geometry of the Lab antenna are summarized in appendix A

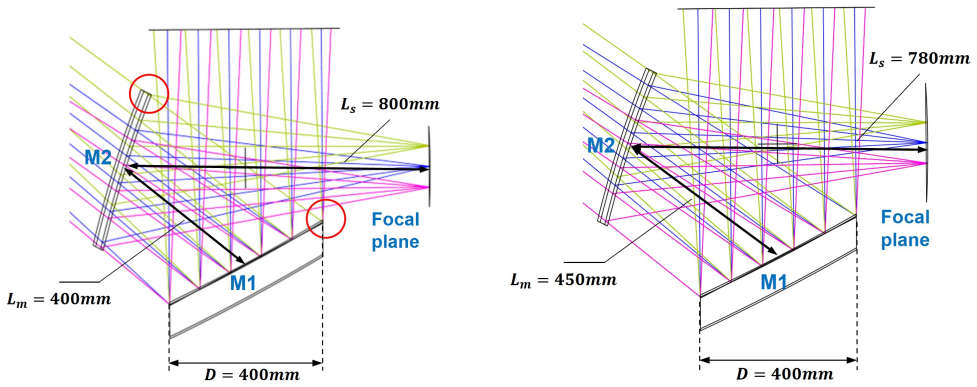

Figure 6.1.: Optical layout of the Lab antenna. (a) The 1/15th scale FYST model; (b) Modified scale model with increasing the space between its two mirrors also meeting the Mizuguchi-Dragone condition.

The two reflectors were milled directly from an aluminum plate. Elliptical rims truncated by the rectangular aluminum plate were used for the two reflectors. The CAD model of the reflectors is shown in figure 6.2. The rim effect on the antenna's radiation beam was simulated and presented in figure 6.3. The diffraction structures in horizontal and vertical directions in the beam are caused by four straight edges cut by the rectangular plate, and four planar areas produce the diffraction structures along the diagonal of the simulated beam map. The effect of the planar regions of the four corners on each reflector can be eliminated by covering absorbers. The two reflectors were then fixed on an aluminum frame and arranged in designed angular positions. The whole structure was mounted on the laboratory wall as shown in Figure 6.2.

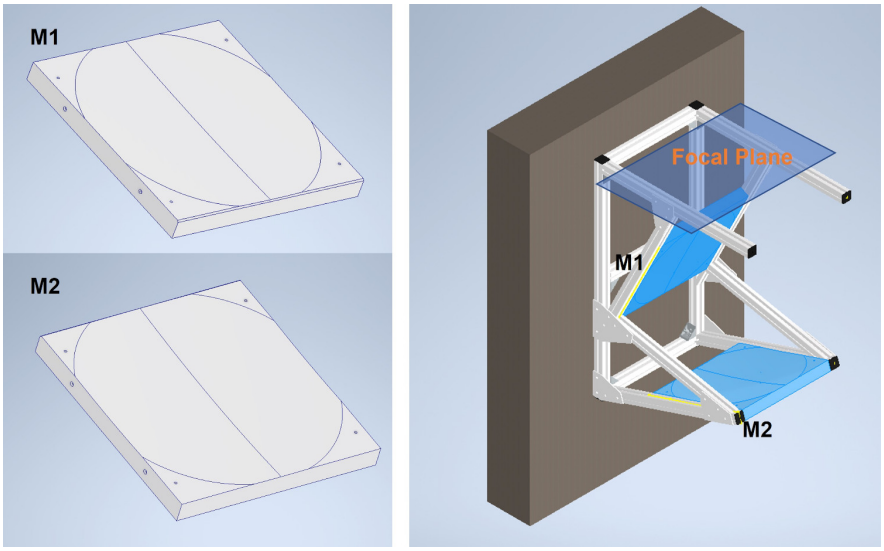

Figure 6.2.: CAD model of the scaled laboratory telescope. Left is model of the two mirrors with four planar area at their corners. Right is the CAD model of the assembled telescope

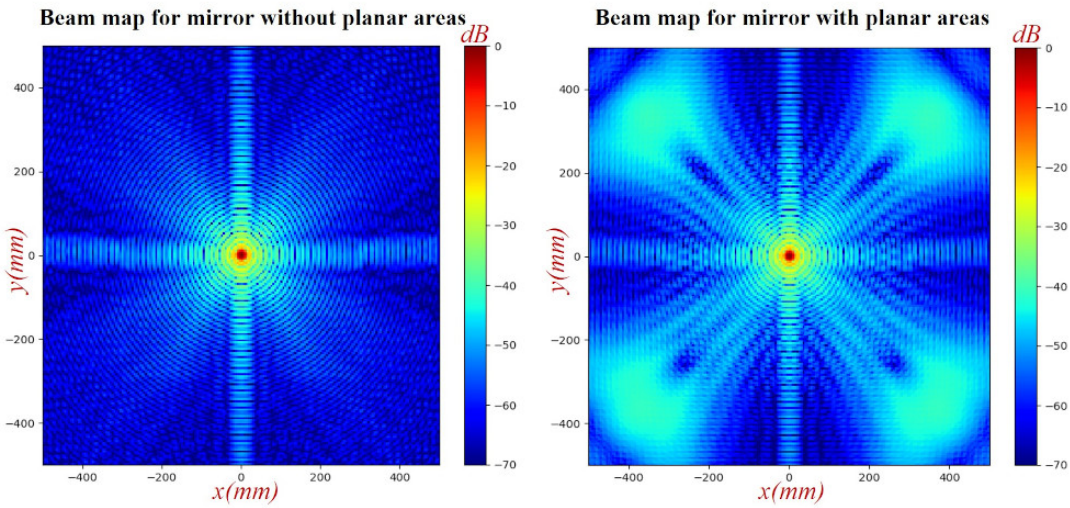

Figure 6.3.: Simulated beam maps of the Lab antenna in source plane that is 5 meters away from the scale telescope. Left is the focused beam for the reflectors without four planar areas in the reflector corners. Right is the simulated beam of the antenna shown in CAD model.

6.1.2. Holographic Design

Requirements of the holography system

The aperture size of the Lab antenna is 1/15th of the FYST telescope. In comparison with the requirement of 100 mm spatial resolution of the 6-m FYST holographic measurement, choosing 10 mm as the spatial resolution to measure the surface errors of

the 400 mm reflectors of the Lab antenna is reasonable, which means 40×40 points on the measured error map. We expect that the measurement accuracy still be better than 2µm, and the measurement error contributed by the thermal noise of the receivers is less than 1µm. Therefore, according to the holography theory described in Chapter 3, to achieve these requirements, the lab antenna's beam maps need to be measured in the angular range of 0.1 radians ($40 \times \lambda/\mathrm{D},\ \mathrm{D} = 400\mathrm{mm}$) with the measurement SNR of > 70 dB.

Then, the new 'Multi-map' holography technique is applied to measure the shapes of the two reflectors separately. In keeping with the FYST holographic design, five beam maps, an on-axis beam, and four off-axis beam maps, are measured by mounting the holographic receiver at the center and 4 corners of a square with a side length of 100 mm in the focal plane shown in figure 6.4. Since The antenna is fixed on the wall, the beam maps only can be measured by scanning the source instead of rotating the antenna. An XY-scanner with a delivery range of 1100 mm in both x and y axes, is used to scan the source over the measured field region. To make sure the XY-scanner covers the whole beam scan range including the four off-axis beams, the distance between the source with XY-scanner and the antenna is set by 5 m. Using this distance, the beam maps are measured in the region of 500×500 mm^2 to achieve the required 0.1 radians beam map size. For the off-axis beam measurement, the receiver deviates from the optical axis by ± 50 mm, which leads to ± 0.048 radians offset of the antenna's pointing direction and ± 240 mm changes of the beam center in the XY-scanner plane. The requirements of the laboratory holography system are summarized in table 6.1 and compared with the FYST holographic design.

Parameters	**FYST**	**Lab-Telescope**
Wavelength λ	$\sim 1\ mm$	$\sim 1\ mm$
Aperture diameter D	6000 mm	400 mm
Beam size λ/D	34.4 arcsec	515.7 arcsec
Distance of source and telescope L	300 m	5 m
Error caused by receiver noise ϵ	1 μm	1 μm
Spatial Resolution δ	100 mm	10 mm
Measured angular range θ	0.01 rad	0.1 rad
Required SNR	>73 dB	>70 dB
Receiver offset from optical axis	$\pm 400\ mm$	$\pm 50\ mm$
Measured map size in the XY-scanner plane		$500 \times 500\ mm^2$

Table 6.1.: Comparison of the basic holographic design for FYST and the Lab antenna.

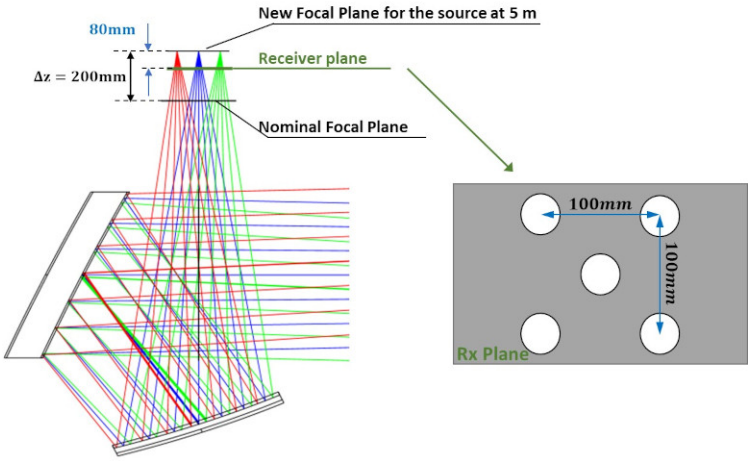

Figure 6.4.: 5 receiver mounting positions in focal plane. One is in center of focal plane. Other 4 positions are at the corners of a 100mm square.

Out-of-focus beam measurements

For the source 5 m away from the antenna, the system's focus is moved 200 mm back from the nominal focus; see figure 6.5. Following the defocused measurement in the FYST holographic system, we put the receiver at the green plane in figure 6.5, 80 mm before the new focal plane, to spread out the antenna's beam and reduce the required dynamic range of the receiver systems. The value of the beam peak is reduced by about 12 dB. Figure 6.6 shows several beams with different amounts of defocus.

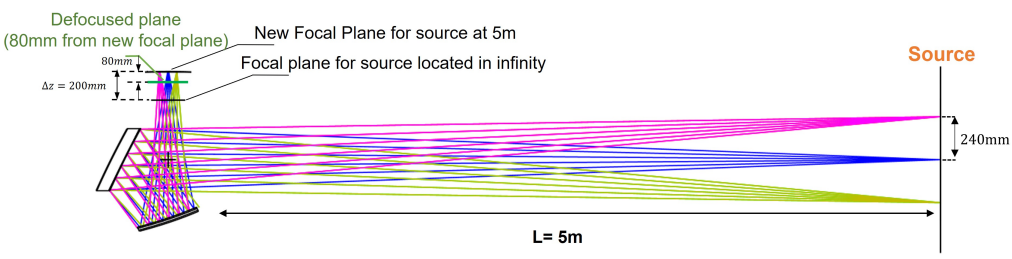

Figure 6.5.: Focused optics of the Lab antenna for the source located at 5 meters from the antenna. The new focal plane is 200mm behind the nominal focal plane. The holographic beam maps are designed to be measured at the green plane in order to spread out the antenna's beam.

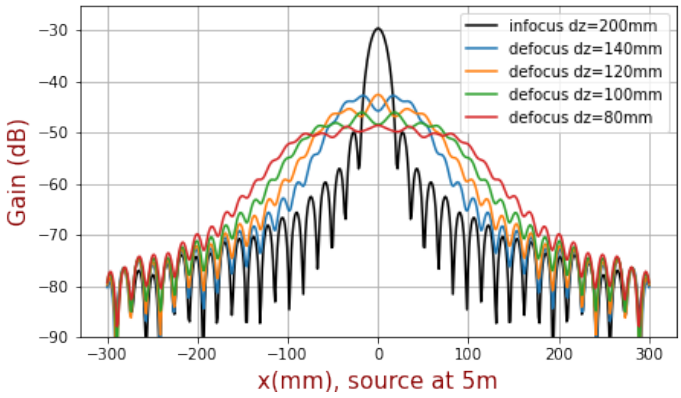

Figure 6.6.: Simulated beams of the Lab antenna with different amounts of defocus. Defocused optics spreads out the antenna's beam. The maximum gain is reduced by 12dB when the receiver is located at the plane of 120 mm behind the antenna's nominal focus or 80mm before the new focused plane for the source at 5 m.

Configuration of the Holographic Testbed

The most critical step of the entire holographic analysis is to measure the antenna's beam maps both in amplitude and phase efficiently and accurately. Figure 6.7 shows the schematic of the holographic system and the testbed in the laboratory. One receiver is vertically sat in the receiver plate to record the incident signal collected by the reflectors of the antenna under test. The reference receiver is mounted on the left of the antenna and keeps looking at the source on XY-scanner to provide the phase reference. Here, the beam is measured by moving the source, so the pathlength of the light from the source to the reference receiver is not constant anymore, but the changes can be measured by simple geometrical calculations. The source module is attached to a plate on the XY-scanner. Its output beam points to the ground and is reflected by a 45-degree mirror to illuminate the antenna and reference receiver.

The extra optics of the reference receiver and source modules presented in section 5.1 is removed, and just the bare feed horns with 1.4 mm beam waist are used to offer a wide beam. The 1/e amplitude beam size of the horn is about 2.3 m for a 5 m wave propagating distance, so the Lab antenna and reference receiver can be sufficiently illuminated even if the source is delivered to the edge of the XY-scanner (550 mm from the antenna center).

Scanning the source changes the pathlength of the signal between the source and reference receiver. We cannot directly measure the phase changes in the reference receiver because of the lack of phase reference. But for the reference receiver with a small beam waist (1.4 mm), 5 meters is much larger than its confocal distance ($\sim$ 6 mm), which means the source is in the far-field region of the reference receiver. Therefore,

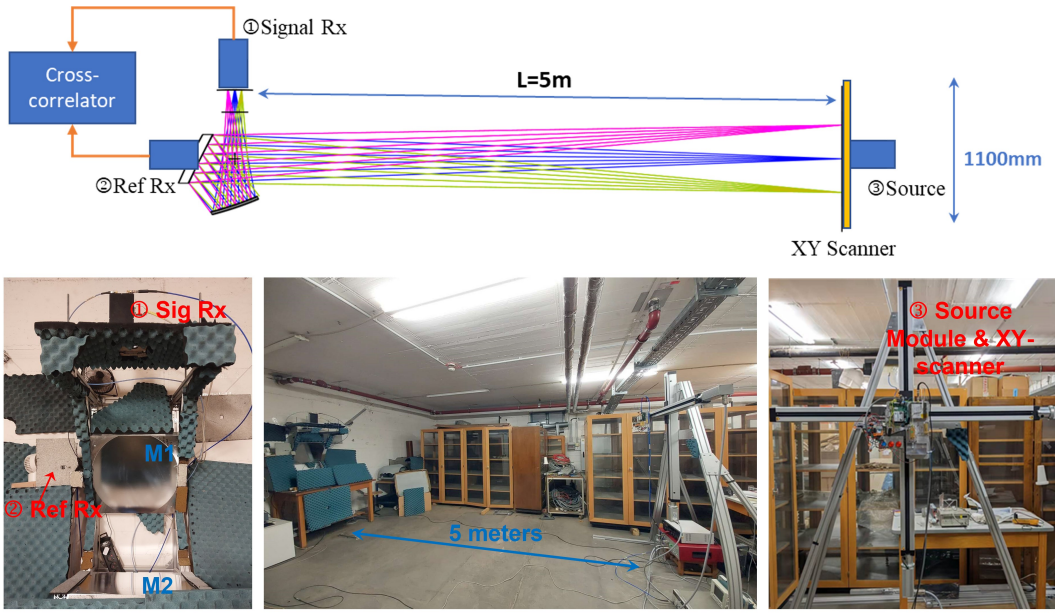

Figure 6.7.: Setup of the laboratory holographic testbed. The top is the Schematic of the test setup. The moving range of the XY-scanner is 1100mm in both the x and y axes to cover all required measured field ranges. The signal receiver (Signal Rx) is sited at the focal plane to observe the beam delivered by the telescope. The reference receiver (Ref Rx) is mounted beside the telescope on its frame to provide phase reference. Cross-correlator is built by the ROACH2 platform and used to digitize receiver responses and calculate the phase difference between the two receiver outputs. The bottom shows the actual testbed setup.

the phase changes in the reference receiver are only related to the distance between the source and the receiver.

Figure 6.8 illustrates the electronic connections of the holography system. The source and the local oscillator of the two receivers are locked by a 10MHz reference signal from the time reference box SyncBox N2X. The beam measurement uses the on-the-fly (OTF) mode, where the source is moved with a speed of 50mm/s while taking data continuously. Then the data stream and the points in the beam map are mapped based on the time stamp. The output data stream includes the power intensity of the signal receiver $|A|^2$, the measured power of the reference receiver $|B|^2$ and the Conjugate multiplication of the outputs of the two receivers.

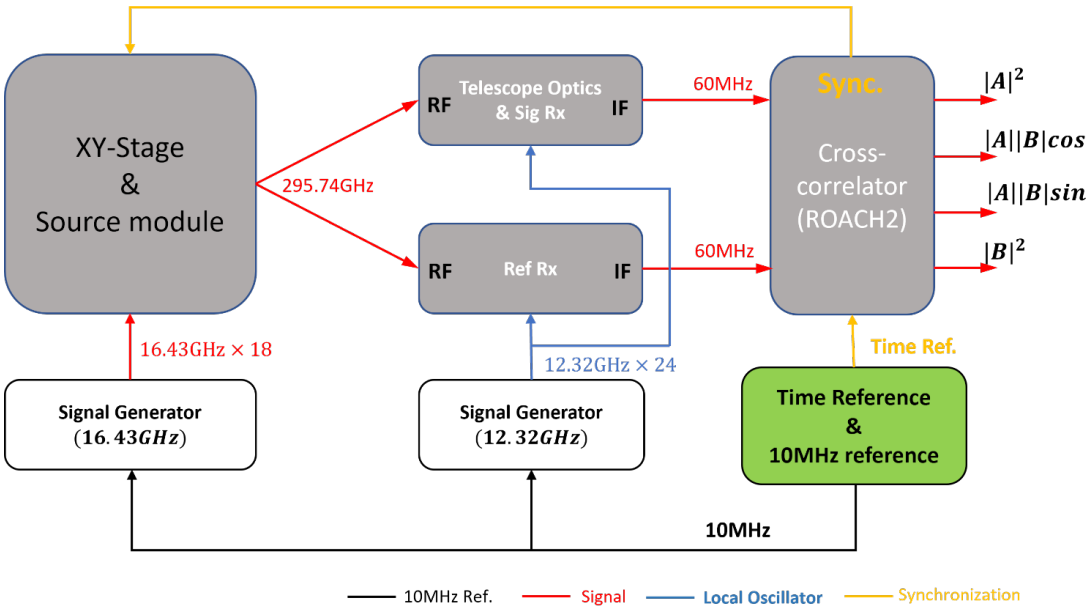

Figure 6.8.: Schematic of Lab electronic connection. All components are locked by a 10MHz reference (black line). The recorded data stream and source moving trace are synchronized by a time reference.

Data taking and pre-processing

We would like to employ the advanced 'star' scanning pattern described in Chapter 5 for the laboratory test. However, the XY-scanner only can maintain stable movements when moving vertically or horizontally. To obtain reliable test data, the regular square pattern is adopted to scan the Lab antenna's beam column by column, frequently passing to the map center to calibrate the systematic drift. The sampled beam map can first be analyzed using conventional holography analysis to check the measurement system. The antenna's beam is recorded in the range of 500×500 mm^2 by 51 vertical scans with an interval of 10mm. The speed of each column scan is around 50 mm/s, so each scan takes around 10s. The data sampling ratio of the back-end receiver is set by 830 points per second to avoid smearing the data. The measured data is convolved with a Gaussian filter to smooth the measured data. We set the Gaussian filter with a bandwidth of 10 points. Then the smoothed data is interpolated into a square grid with 51×51 points that are used for the holographic analysis in the following sections.

6.2. Experiment 1: Conventional One-beam Holography Analysis

We start the Lab test from the conventional near-field holography experiment to check the operational performance of the Lab system. Measuring one beam map only offers one reflector surface errors that are the error combinations in the two reflectors of the antenna, but its mature theoretical frame and analysis technique can help verify the accuracy of the test platform and check the systematic mistakes. In this section, the software technique developed in Chapter 4, which analyze the reflector surfaces by fitting the measured beam maps, in theory, also works foro the one-beam holography. Therefore, we also present the results analyzed by this new technique, and compare the analyzed errors with the conventional results.

6.2.1. Surface Diagnosis for the Smooth Reflectors

The initial test is to measure the antenna's beam in the map size of 1000×1000 mm^2 by mounting the receiver at the focus, which means the optics is focused. The smooth reflectors means that there is no artificial surface errors in the reflectors such as copper foils used later. Figure 6.9 shows the measured and simulated beam pattern of the small antenna. The diffraction features caused by the four planar corners in the reflector and the reflectors' rectangular rims are observed compared to the simulated beam. The bottom plots in the figure are the zoomed-in central beams and their contour maps. It can be seen that the measured center beam is distorted, which means the reflectors of the antenna are not perfect, the surface deformations exist. The following holographic analysis is presented to analysis the antenna deformations.

According to the holographic design in section 6.1, the beam map in the range of 500×500 mm^2 is required for 10 mm spatial resolution. Figure 6.10 is the holographic beam in amplitude and phase which is measured in the near field. The conventional holographic analysis only gives one aperture field distribution, and the phase deviations are contributed by the surface errors in both reflectors. In this section, the solved aperture phase distribution is converted into the equivalent surface errors in M1 with assuming a perfect surface in M2. The data is first analyzed based on the physical optics propagation (POP) [98][99]. Equivalent surface errors in M1 are also analyzed by using the new fitting technique.

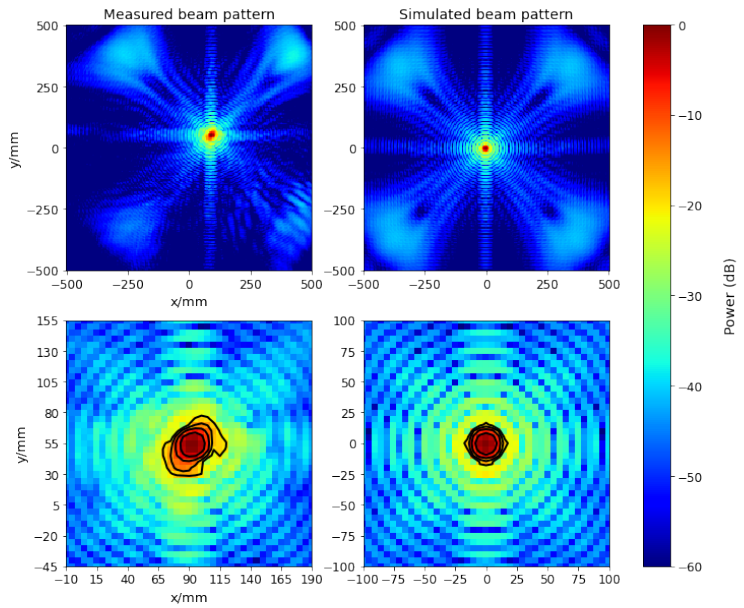

Figure 6.9.: Initial measured beam pattern at the range of of $1000 \times 1000mm^2$ and the simulated beam for the antenna with ideal reflectors. Top: Measured beam pattern of the Lab antenna and the simulated beam pattern for the ideal antenna model; Bottom: Enlarged center beam of the measured and simulated beam maps. Their contour maps are also drawn, and the contour line level represent 0, -5, -10, -15, and -20 dB from inner contour line to outer line.

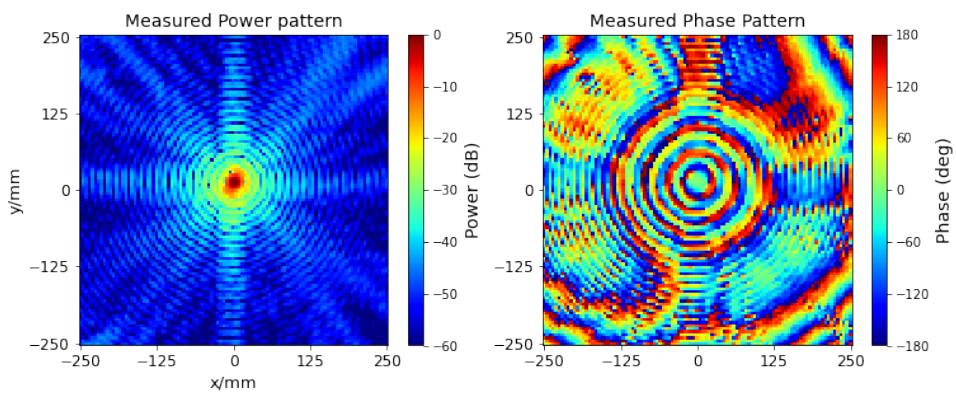

Figure 6.10.: Measured focused beam map in amplitude and phase. Size of the beam map is $500 \times 500mm^2$ to achieve 10mm spatial resolution for the measured surface error map.

Analysis Using Angular Spectrum Propagation

The Fourier transform pair exists between an antenna's far-field complex (power and phase) beam map expressed in the angular domain and its aperture fields. According to this relationship, we can call the antenna's far-field beam the angular spectrum of the aperture fields, meaning that the aperture fields can be decomposed into parallel waves from different directions with specific intensities and phases. Therefore, the fields in any planes between the aperture and infinity can be predicted by correcting the phase changes in each wave component. This technique is called angular spectrum propagation [98][99].

The beam is measured in the plane parallel to the aperture plane and 5 m apart. We denote the measured beam map as $f_A(x, y)$, which is converted into the aperture fields expressed by $f_B(x, y)$ using the angular spectrum propagation technique. The analysis processes are summarized below:

1. Calculate angular spectrum of the observed field labelled by $F_A(u, v)$ using fast Fourier transform algorithm [100], where u and v are expressed by $sin\theta \cdot cos\phi$ and $sin\theta \cdot sin\phi$ respectively. θ and ϕ represent the elevation and azimuth angles of the antenna pointing direction. This step is expressed by equation 6.1.

$$F_A(u, v) = FT[f_A(x, y)] \tag{6.1}$$

2. Compute the angular spectrum of the field in aperture $F_B(u, v)$. The calculated angular spectrum in step 1 is modified in phase term by multiplying $e^{j2\pi/\lambda\delta z\cdot\sqrt{1-u^2-v^2}}$, where δz is 5 m, the distance between the two planes. The angular spectrum of the aperture fields is expressed by

$$F_B(u, v) = F_A(u, v) \cdot e^{j\frac{2\pi}{\lambda}\Delta z\cdot\sqrt{1-u^2-v^2}}. \tag{6.2}$$

3. Make inverse Fourier transform on the new angular spectrum $F_B(u, v)$ to get the aperture fields $f_B(x, y)$ which is expressed by

$$f_B(x, y) = IFT[F_B(u, v)]. \tag{6.3}$$

4. Calculate the phase deviations $\Delta\phi$ in the aperture plane. Subtracting the phase of the ideal aperture fields $F_{ideal}(x, y)$ from the measured aperture fields gives the phase deviations produced by the surface errors of the reflectors. The calculation is expressed by equation 6.4. Here, in the phase residual, the phase slope along the x and y axes and curved phase terms must be removed by the fitting process,

which is caused by the position errors of the receiver and the inaccuracy of the measured distance between the source and the antenna's aperture plane.

$$\Delta\phi(x,y) = Phase\{f_B(x,y)/f_{ideal}(x,y)\} \tag{6.4}$$

5. Convert the aperture phase deviations into the equivalent surface errors ϵ_{M1} in M1 based on the reflection angle Θ and the operating wavelength λ.

$$\epsilon_{M1} = \frac{\Delta\phi \cdot \lambda}{4\pi \cdot cos(\Theta/2)} \tag{6.5}$$

Figure 6.11 left is the phase deviations in the aperture plane before removing the slope and curvature terms. Figure 6.11 right shows the errors in M1 analyzed using the above algorithm. It can be seen that twist errors in the reflector surfaces are observed, which distorts the center beam of the antenna shown in figure 6.9. But the surface errors cannot tell us which reflector is twisted.

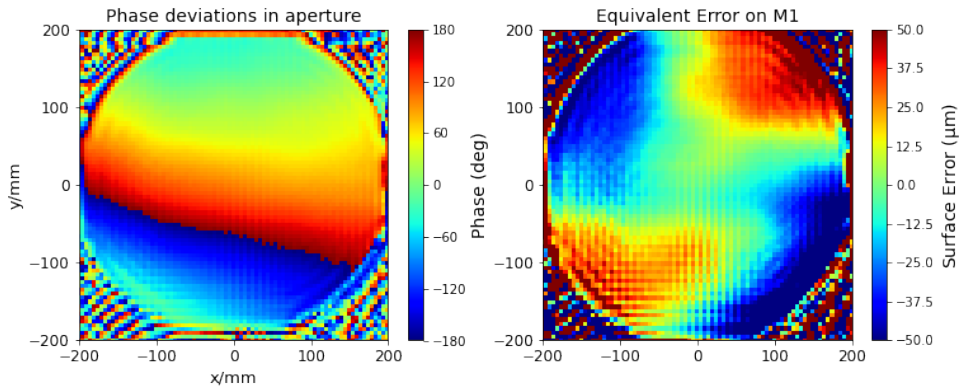

Figure 6.11.: Measured equivalent surface error in M1 using the conventional holographic analysis. Left: Phase difference between measured phase and theoretical phase on aperture plane. The phase difference shows that sloped phase and curved terms exist because of alignment systematic errors in the test system. Right: the equivalent surface errors in M1 after removing sloped and curved phase terms from phase difference on aperture.

Analysis Using the Fitting Algorithm

In theory, the fitting algorithm in the software developed for analyzing the multiple beam maps also works for the system with one reflector. The surface errors in M1 are expressed by 30×30 grids (900 fitting parameters), and each grid has a size of $\sim 13.33 \times 13.33$ mm^2 that is a little bit larger than the design 10 mm spatial resolution. We also can parametrize the surface by Zernike polynomials [101][11], for example, the polynomials with a maximum order of 30th (496 parameters). The surface of M2 in the

analysis is also assumed to be perfect. The parameters described in section 4.2 that express the large spatial errors are also included in the fitting process. The analysis procedure is summarized below:

1. Fit the parameters describing large spatial errors. These large spatial errors can be caused by the misalignment of the antenna's optical axis, inaccuracy of the location of the receiver or source, and the size of the illumination beam of the source and receiver. The fitting step converges quickly and can significantly reduce the residual between the measured beam and the simulated data. It also helps to improve the fitting efficiency for the next detailed surface analysis.

2. Fit surface errors. The fitting parameters from Step 1 are fed into the model to compensate for the systematic errors; then, surface parameters are fitted.

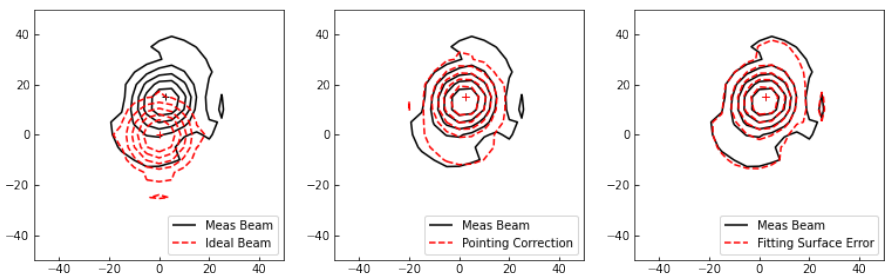

Figure 6.12.: The computed beam in the different fitting stages. Black contour lines represent the observed beam, and red lines are the computed beams in the fitting stages. Left: The comparison of the observed beam and ideal simulated beam; Middle: The beam after fitting large spatial parameters, here the large spatial error is a pointing error; Right: The beam simulated by the fitting M1 surfaces.

Figure 6.12 gradually demonstrates the improvement in the agreement between the observed and fitted beams. It can be seen that the pointing offset in the system is obvious and can be found and compensated by the fitting analysis. The parameters describing the M1 surface deviations are also solved following the fitting process. Figure 6.13 shows the fitted surface maps analyzed using the Zernike polynomials and 900 grids. The twist errors are also observed compared to the previous analysis.

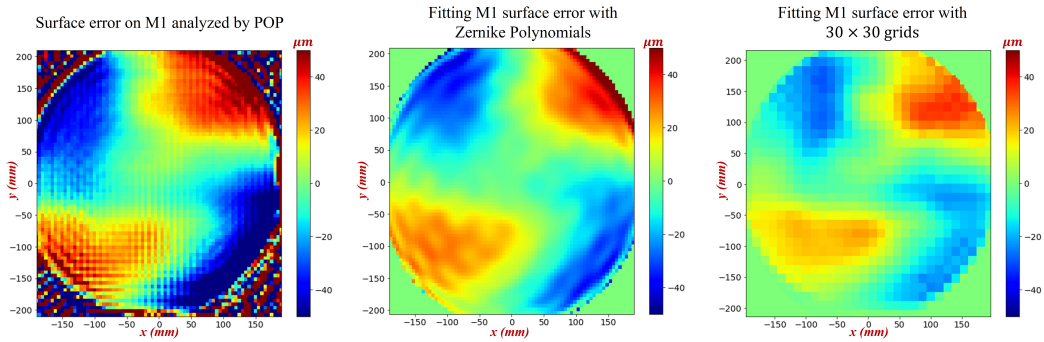

Figure 6.13.: Equivalent surface error map in M1 analyzed by three different software methods. Left: Error map analyzed by using physical optics propagation technique. Middle: Error map analyzed by fitting the coefficients of 496 Zernike polynomials. Right: M1 error map resolved by inference approach with 30×30 grids. Results produced by the POP technique and inference approach both indicate that the twist distortions exist in the antenna system.

6.2.2. Diagnosis for Artificial Surface Errors in the Reflectors

To further test the accuracy of the measurement system, copper foil with known thickness is used to create piston surface errors. Some dielectric materials like Mylar and plastic tape are used to make negative piston errors. The equivalent surface displacement of the transparent dielectric materials is unknown because of the unknown dielectric constant of the glue layer and the multi-reflection of the surfaces. But it is still worth introducing negative piston errors. We expect that the laboratory test platform can measure it. Figure 6.14 shows the position of patches in M1 and the image of the copper patch in M2.

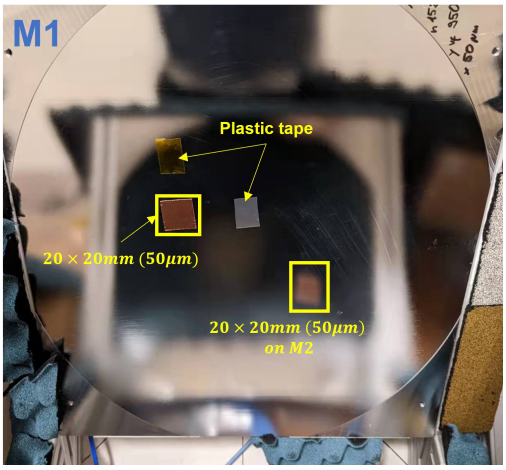

Figure 6.14.: Artificial piston errors in M1 and M2. Two copper tapes with the size of $20 \times 20mm^2$ and thickness of $50\mu m$ are separately attached in M1 and M2. Dielectric materials, plastic tape, and Malyer membrane are used for negative piston errors.

The beam distorted by these error patches is measured and compared with that of the smooth reflectors shown in Figure 6.15. The distortion in the central beam is still observed. Repeating the previous holographic analysis and comparing the position and thickness of the artificial errors can help check the system's accuracy. Figure 6.16 middle presents the analyzed error map. Removing the twist errors from the newly measured error map can show the piston errors caused by copper and plastic patches. The resolved piston errors caused by copper patches agree very well with the copper thickness that we used. The equivalent negative piston errors created by plastic tape and Mayler membrane are also measured. Figure 6.16 right shows the measured patches and −10µm and 50µm contour line.

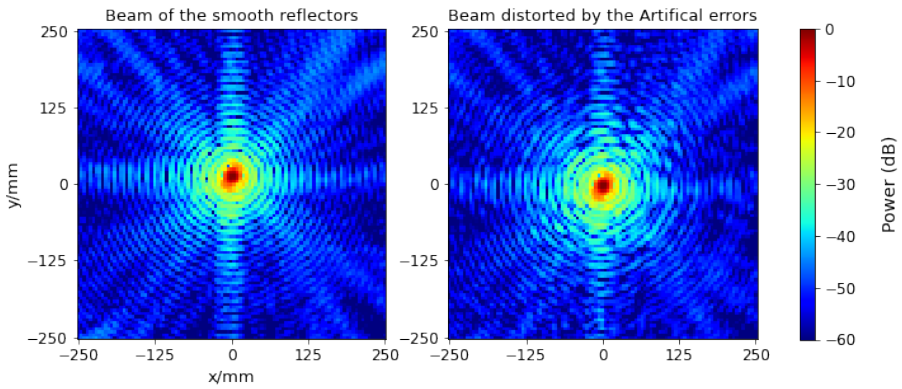

Figure 6.15.: The observed beam that is distorted by artificial errors explained in Figure 6.14. The right picture is the measured distorted beam compared to the smooth mirror beam (Left).

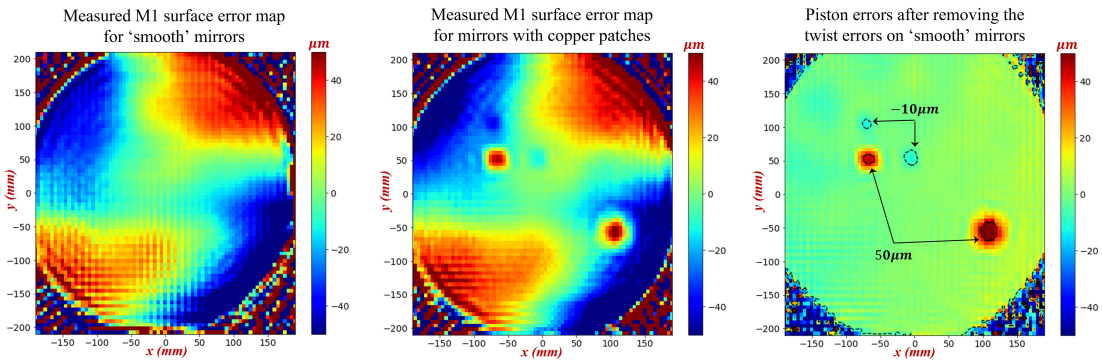

Figure 6.16.: Measured artificial piston errors in M1. The 50µm copper patches are precisely resolved. Left: The error map of smooth mirrors. Middle: Error map for mirror surfaces with copper tape, plastic tape, and Mylar membrane. Right: Piston errors caused by artificial patches by removing the measured twist error over the smooth reflectors.

6.2.3. Summary

The holographic beam measurement system was successfully established and implemented for the conventional holographic analysis and measuring the equivalent surface errors in M1. It is proven that the 300GHz holographic system is operational in the laboratory. The twist error in the antenna system and the artificial square errors in the reflectors also can be measured. To test the system's stability and statistical performance, 8 independent measurements were implemented. The results indicate that the equivalent M1 surface errors can be measured with a $< 1\mu m$ statistic error.

The test also proves that using the fitting technique developed in Chapter 4 to analyze traditional near-field holographic data also works. This analysis technique also can offer the information about systematic errors, such as the misalignment of the antenna's optical axis and the illumination errors caused by the inaccuracy of the beam size of the source and receiver.

Conventional holography measurement cannot solve the issue of surface error degeneracy between two reflectors. The measured surface error tells us that the twist error exists in the optics. But it cannot point out from which reflector the errors are. Therefore, the designed multi-beam holography system will be implemented to solve the issue, which will be presented in the rest of this chapter.

6.3. Experiment 2: Multi-map Holography Measurement

The operational performance of the laboratory holographic system has been verified. The conventional holographic analysis can accurately measure the artificial errors and indicates the twist errors in the reflectors. In this section, the multi-map holography analysis is implemented to distinguish the source of the measured errors between the two reflectors. The feasibility of breaking the surface degeneracy between the reflectors and the ability to discriminate the small-size artificial surface errors are tested. The measurement accuracy and ability to identify the large-scale deformations over the entire reflector are also checked.

Following the configuration described in section 6.1, the other four off-axis beam maps need to be measured by putting the receiver two four corners of a square in the focal plane shown in figure 6.4. The two reflectors have the same size, 400×440 mm^2 The surface deviations of the two reflectors are expressed by the piston displacement of 30×30 grids, respectively. Each grid is about 14.7×13.3 mm^2. There are 1850 parameters in total for fitting, 1800 for describing the reflector surface errors, and additional ten parameters for correcting the large spatial errors (50 parameters for the five measured beams).

6.3.1. Analysis for the Distorted Reflectors in Experiment 1

We first continue the surface diagnosis for the antenna with artificial surface errors shown in figure 6.14 in Experiment 1. The one-beam holographic measurement accurately measures the four error patches and indicates the twist-like large spatial errors in the antenna system. Then the other four off-axis beams are measured to distinguish these errors between the two reflectors. The four off-axis and focused beam maps are presented in figure 6.17 compared to the ideal antenna's simulated beam maps.

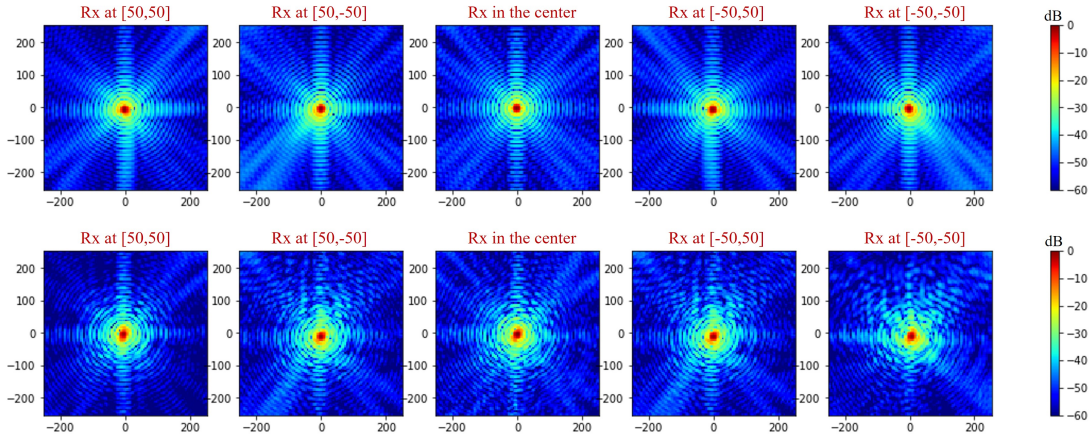

Figure 6.17.: Top: The simulated 5 focused beam patterns for the ideal reflectors; **Bottom:** Measured 5 focused beams of the distorted mirrors in 6.14, including center beam and 4 off-axis beams.

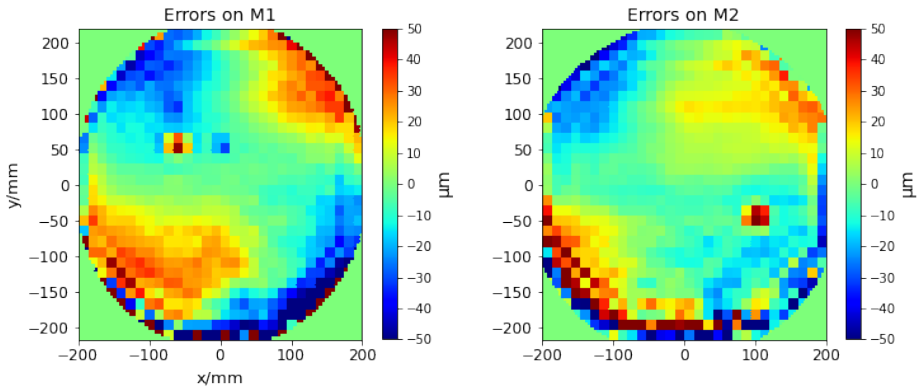

Figure 6.18.: Measured surface error maps of the laboratory antenna with artificial errors shown in figure 6.14. The reflector surfaces are analyzed by fitting 30×30 grids on each reflector.

The optical alignment errors in the five beam measurements are first analyzed by fitting the 50 parameters describing large spatial errors. Then the detailed surface analysis is implemented to fit the 1800 surface parameters. Figure 6.18 shows the analyzed surface error maps. The two copper patches are measured and identified

between the errors on the two reflectors. The two plastic squares (negative piston errors) are also correctly distinguished.

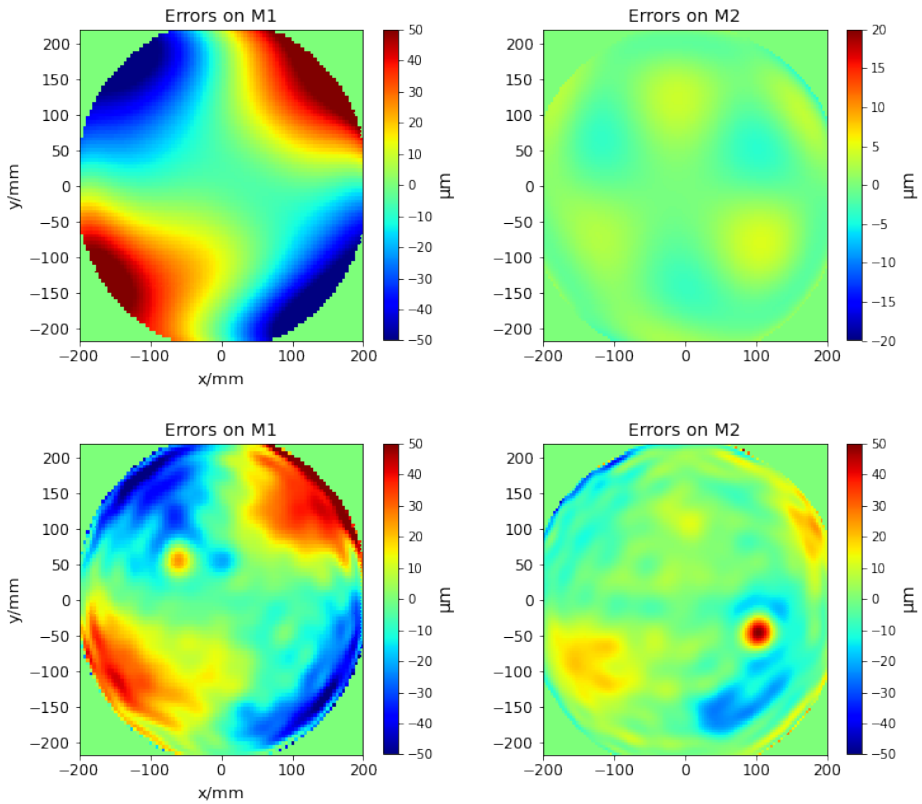

Figure 6.19.: Error maps analyzed using Zernike Polynomials to express the surface deviations. a): Large-scale error in the reflector surfaces analyzed by using Zernike polynomials with a maximum order of 7th, indicating the large-scale twist-like errors are from M1; b): Error maps analyzed by using Zernike polynomials with a maximum order of 30th.

In addition, the twist error observed in the previous experiment is also measured in the multi-map experiment. It can be seen that both reflectors are twisted, but the errors in M1 are more obvious than that in M2. To verify this large-scale error, we measured the flatness of the two reflectors with a flat panel and found the errors only existed in M1. The analyzed twist errors in M2 should be fake. Since the beam distorted by the twist errors in M1 also can be produced by the similar error patterns in M2, and these surface errors change smoothly in the reflector, even the difference in off-axis beams is also slight. Moreover, using 30×30 grids for expressing the surface deviations, the inference software only partly measures the large-scale errors. But if the Zernike polynomials with a maximum order of 7th are used to express the surface, and the fitting analysis shows more reasonable results seen in figure 6.19 top. Using the Zernike polynomials with a maximum order of 30th, 496 parameters describing surface errors of

one reflector, the details of the reflector surfaces are also solved shown in figure 6.19 bottom.

This experiment proves that the multi-map holographic analysis can help distinguish surface errors between the two reflectors for the case where the errors are not overlapped in the aperture plane. The existing large-scale errors can also be measured and separated by using the Zernike polynomials describe the surface deviations and fitting their coefficients. Next step, the errors on the two reflectors overlapped in the aperture are made to test the new metorogy further.

6.3.2. Analysis for the Case with Artificial Degenerate Errors

In this experiment, the copper foil with a thickness of 50µm is used to make the surface errors on the reflectors, and the phase errors on the aperture plane produced by these errors are overlapped. Figure 6.20 details the error patches on M1 and M2 and the phase deviations on the aperture plane.

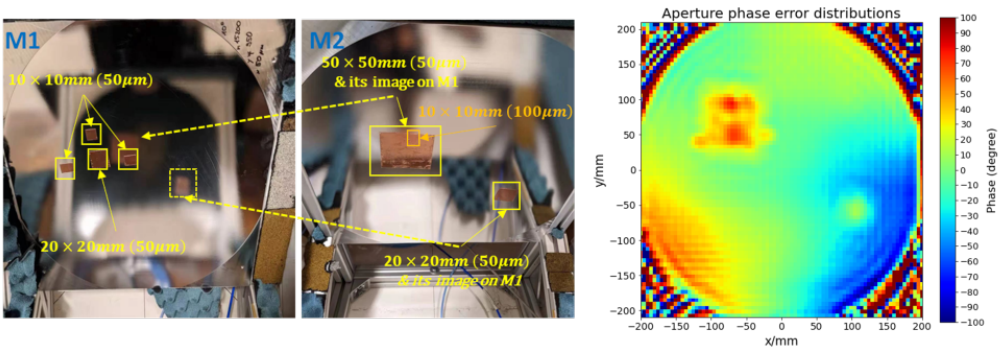

Figure 6.20.: Surface errors producing overlapped phase errors on the aperture plane. Left: Artificial piston errors on the two mirrors created by copper tape with a thickness of 50µm; Right: Overlapped phase errors on aperture produced by the piston errors on M1 and M2.

The multi-map holography analysis is implemented for the focused and out-of-focus optical setups, respectively. For the out-of-focus setup, the receiver is placed at 120 mm behind the antenna's nominal focus or 80 mm before the new focus of the near-field system. Figure 6.21 presents the measured distorted beams. The defocused setup spreads out the antenna beam and reduces the maximum gain of the antenna by 12 dB relative to the focused beam. The out-of-focus measurement is to verify the setup for the FYST holographic test, which is designed to spread out the beam and decrease the gain by 20 dB to reduce the requirement of the dynamic range of the holographic hardware.

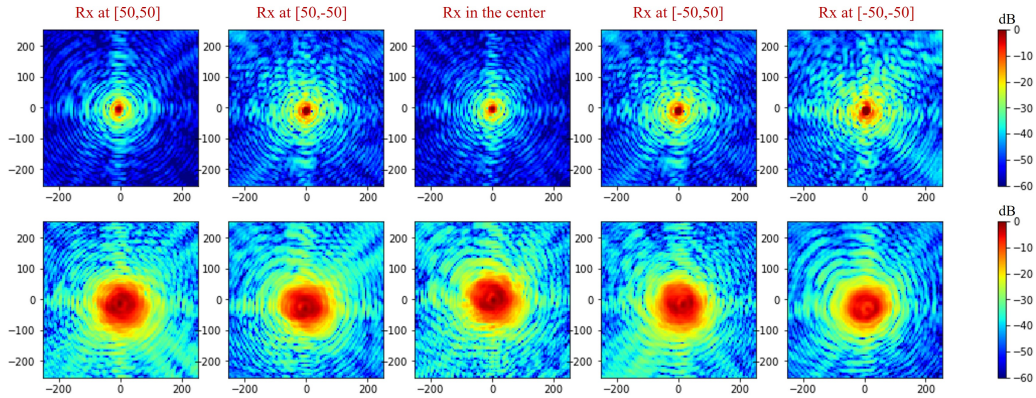

Figure 6.21.: Measured beam maps distorted by the reflector errors in figure 6.20 Top: Distorted beam maps for the focused system; Bottom: Out-of-focus beam maps, receiver is 120 mm behind the antenna's nominal focal plane and 80 mm before the new focal plane of the near field system.

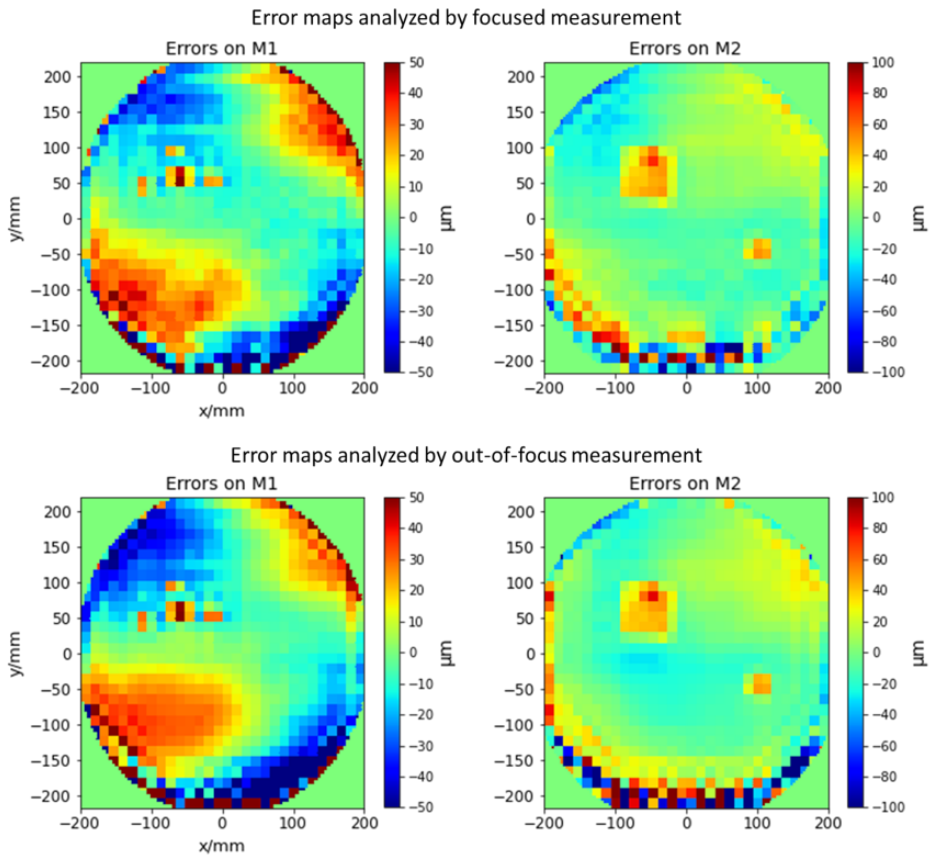

Figure 6.22.: Solved error maps of the Lab antenna using the focused and out-of-focused multi-map holographic measurement. Top: Analzyed error maps using the focused beams; Bottom: Error maps analyzed by the out-of-focus beam measurements.

The solved error maps are shown in figure 6.22. The two independent tests give

a similar surface error distribution on the two reflectors, and both can distinguish the overlapped surface errors between the two reflectors and gives the same values. The difference between the two measurements is mainly caused by the changes in the multi-path reflections in the laboratory and other unstable systematic errors, such as the movement errors of the XY-scanner. The twist error on M1 is still observed.

Twist Errors

The one-beam holographic test shows that twist-like errors exist in the laboratory antenna. Then, the multi-map holographic measurements further indicate that M1 is twisted. Unfortunately, we cannot offer another way to measure the twisted reflector and verify the validity of the measurements. The reflectors also cannot be precisely adjusted. We used a flat panel to measure the flatness of M1 and can confirm the distorted M1. In order to verify the tests, we adjust the mounting frame of M1 to fix the twist error manually with keeping M2 unchanged. The multi-map holographic test is employed again to check the surface changes in M1. Figure 6.23 presents the error maps after the correction.

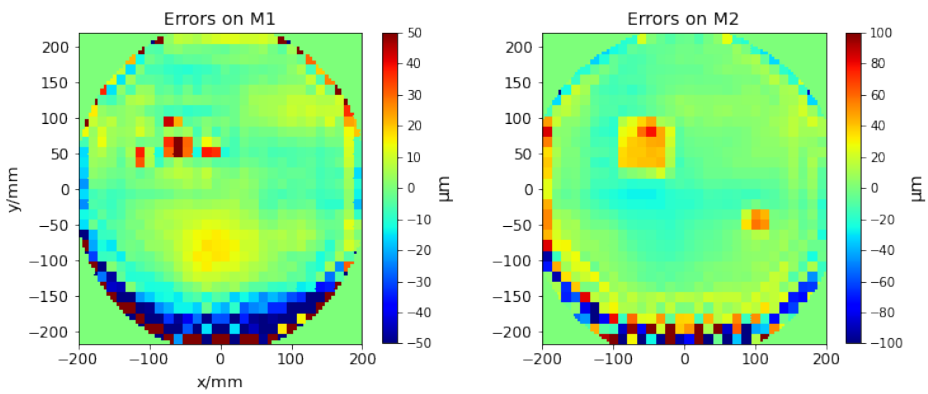

Figure 6.23.: Holography analysis results after correcting the twist error on the M1 surface.

From figure 6.23, it can be seen that the twist errors on M1 disappear compared to the error maps in figure 6.22. The previous measurements also indicate slight twist errors in M2, but the errors also disappear in figure 6.23. This further confirms that the measured twist errors in M2 are fake, as explained in section 6.3.1. We also find that using Zernike polynomials to describe the reflector surface deviations can discover the large-scale surface errors more precisely than that using 30×30 grids. This means the accuracy of modeling the surface deviations degrades the ability to discriminate the large-scale errors. Therefore, we suggest estimating large-scale errors of an antenna under test before starting the detailed surface analysis.

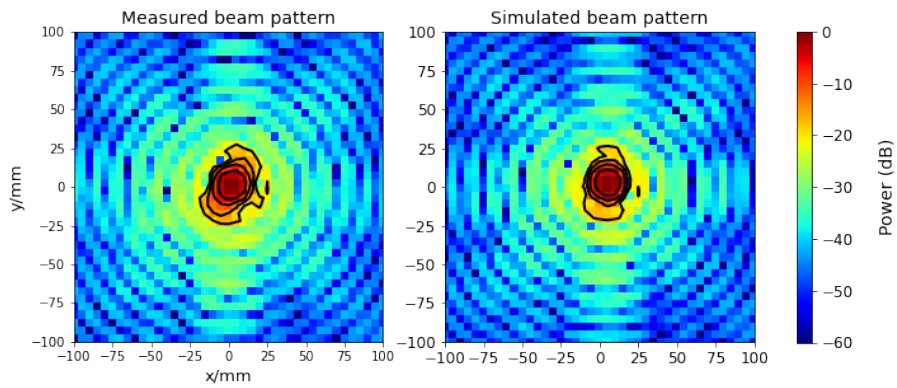

Figure 6.24.: Comparison of the focused beams before and after the twist error correction. The contour lines represent the power levels of 0, -5, -10, -15, and -20 from inner to outer contour lines. Left: Focused beam distorted by twist error on M1. Bottom: Measured beam map after correcting the measured twist error.

After the correction, the focused beam of the lab antenna removing all artificial errors is measured and compared with the beam measured at the beginning of the laboratory test. Figure 6.24 shows the beam comparison. It can be seen the beam distortion is partly fixed after the previous holographic tests and corrections.

6.3.3. Measurement Accuracy

The thickness of the copper foil used in the previous experiments is around 50µm. Since the copper foil is attached to the reflector surfaces with a glue layer of unknown thickness. To check the measurement accuracy, we use highly precise copper foil with a thickness of 10µm and 20µm and attach them to the reflectors by oil. The multi-map holographic analysis is implemented twice, one for the smooth reflectors without artificial surface errors and another for the errors described in figure 6.25. Taking the difference between the two measurements can cancel the effect of the laboratory's unknown reflections and manufacturing errors in the two reflectors. Then the difference shows the measured errors of the created errors. The results are displayed in figure 6.26.

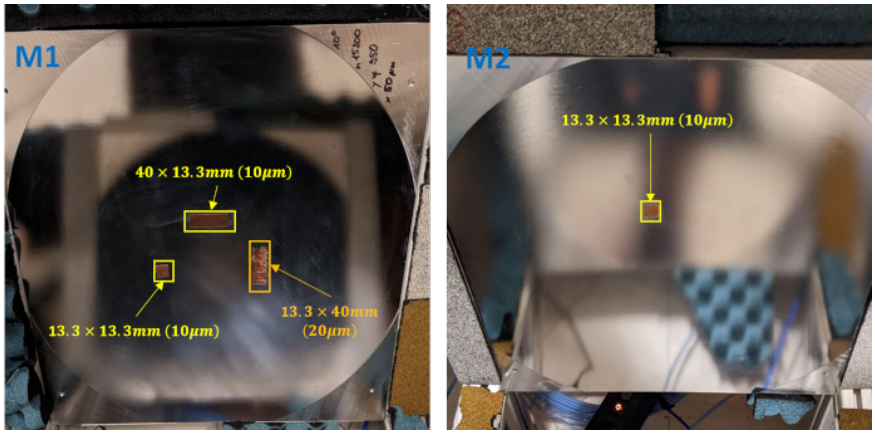

Figure 6.25.: Surface errors on M1 and M2 using high precise copper foil with thickness of 10µm and 20µm.

The measured surface error maps prove that the holographic system can measure 10µm surface deviations with an error of < 2.5µm. We can see that the measured error maps still have high-order surface errors on the two reflectors, which are almost compensated for each other. It is because the regularization term described in section 4.2.2 is used in the fitting software, which compresses the total surface deviations to avoid the wrong fitting route. Seven independent tests show a statistic error with a standard deviation of 0.8µm.

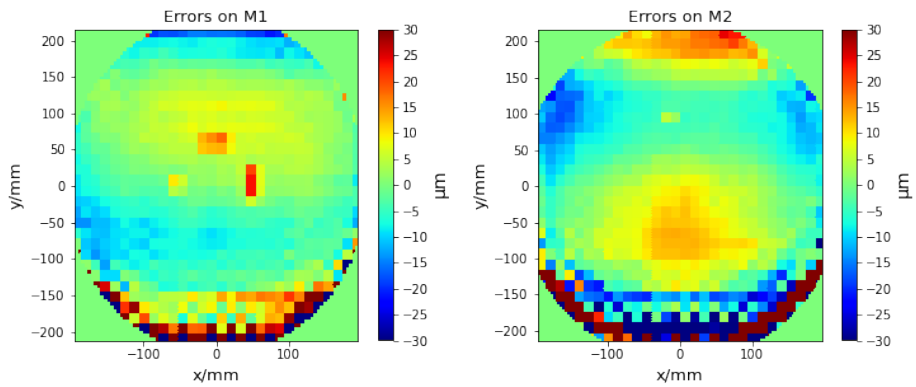

Figure 6.26.: Measured surface error maps for the 10µm surface errors. The statistic error is less than 0.8µm estimated by repeating the measurements seven times. The maximal measurement error for these copper foil is less than 2.5µm.

6.3.4. Summary

The novel multi-map holographic approach has been successfully implemented to analyze the artificial surface errors and the twist large-scale errors in the small Crossed-Dragone

antenna. It has been proven that the new technique could discriminate and measure these minor surface errors with a repeatable error of $< 1\mu m$. The tests have been done for the focused and out-of-focus optical setups, and both could precisely discriminate and measure the created errors. Large-scale errors, such as the twist errors on M1, can also be measured and discriminated using the new method. We found that employing Zernike polynomials in the fitting software to express large-scale surface errors can give more precise results.

Chapter 7.

Conclusion and Outlook

In this dissertation, a novel holography metrology for measuring the surface shapes of the reflectors of FYST has been investigated. This breaks new ground in both the high measurement accuracy ($< 2\mu m$) and in the fact that it can measure and discriminate the surface errors in the two large reflectors making up the FYST optics. The thesis accomplished these goals through three aspects: 1) The multi-map holography technique was developed to break the degeneracy between the two reflectors of FYST by making beam measurements at multiple positions in the focal plane; 2) The method for efficiently calculating the beam pattern of the Crossed-Dragone optics of FYST was developed by using the scalar Kirchhoff-Fresnel diffraction theory and calculating the diffraction fields of FYST by two steps. This method is the critical step for the new data processing software of the multi-map holography to convert the multiple beam maps to two surface maps; 3) The 300GHz holography system, including the necessary hardware, software, and telescope scanning pattern, was designed and built to precisely measure beam maps and minimize the effects of systematic errors.

In the first part of the thesis, the fundamentals of the PO analysis technique were presented and used to demonstrate the reflecting antenna radiation theory, which explains the basic principle of conventional microwave holography. Then, the electromagnetic characteristics of FYST were also studied by the PO method with the commercial TICRA GRASP software. The efficient 'two-step' PO analysis was developed by breaking the PO analysis into two steps and calculating the fields in an intermediate focal plane first, which can reduce the computational time by two orders of magnitude. Replacing the PO analysis with the scalar Kirchhoff's diffraction method, which neglects the polarization information, the computational was further reduced by two orders of magnitude. This technique makes it possible to analyze the data of the multiple holographic beams efficiently. The computational accuracy of the two new techniques has been verified using the commercial GRASP software to model the same optics. The 'two-step' PO

method is equivalent to the fundamental PO analysis, which can simulate any large and complex optical system.

Extensive numerical simulations of the FYST multi-map holography measurement have been carried out to test its accuracy, sensitivity, and optical setup. The results indicate that measurement accuracy of $\sim 2\mu m$ can be achieved. It was found that the telescope's pointing/tacking errors can significantly degrade the accuracy. To solve this, an additional fitting model, modeling the telescope's motion on time, is required to fit the telescope's moving path. The new holographic doesn't require the measured field points to be on a regular grid, so an efficient circular or star scanning pattern can be used, effectively minimizing the systematic errors caused by instrument drafts and atmospheric fluctuations.

In the final part of the thesis, the developed 'multi-map' holography method and the FYST holographic instruments were implemented for the small laboratory 'Crossed-Dragone' antenna to measure the artificial piston errors on its reflectors. The experiments prove that this technique can help to identify the surface errors on the two reflectors and achieve a statistic error of less than 1µm. Unexpected large spatial surface errors caused by the twisted primary reflector (M1) were observed by both the conventional holographic analysis and the multi-map holography software. The conventional holography analysis only points out the existence of errors but cannot give a detailed diagnosis. The new 'multi-map' holographic analysis, if fitting the large-scale errors by using a few low-order Zernike polynomials (e.g., maximum order of 7th), can identify the large spatial errors between two reflectors. But if fitting the 30×30 square grids to solve the surface details of the reflectors, the part of the large scale errors are converted to another reflector because the fitting process rudely finds the fitting parameters to minimize the difference between measured and simulated data. Actually, the large spatial errors are still partly measured and corrected after the panel adjustment. Repeating another holographic measurement, analysis, and panel corrections, the large-scale errors can still be removed. Thus, in this dissertation, it has been shown that the new holographic metrology can diagnose the surface quality for FYST.

The developed holographic system will be the first instrument installed in FYST. The pretest and panel alignment for FYST will be in Xanten, Germany. In the laboratory experiments, the analyzed surface maps suffer from multi-path reflections in the small lab space, especially the reflections between the antenna and the source module. This can be avoided for the FYST holography because of the outdoor test and the long distance (200-300 m) between the source and telescope. Hence, the measurement accuracy should be better than the laboratory measurement. Nevertheless, the atmosphere's influence will worsen, and the form of the phase errors caused by atmospheric turbulence

may differ from what we assumed. It is better to measure the phase stability of the atmosphere on the site by having the telescope and reference receiver observe the source from their boresight. So that we can find the best telescope scanning pattern to minimize these effects. For example, if the atmospheric phase errors change too fast, let the telescope pass to the beam center more frequently by increasing the scanning speed and the number of radial scans. It is effortless to load the developed data processing software to a commercial graphic card with more than 20GB of memory. The time of the holographic data analysis can be reduced from < 1 hour to < 20 min. It is also worth checking the feasibility of this metrology for a telescope with three reflectors.

Bibliography

[1] Karl G Jansky. "Electrical disturbances apparently of extraterrestrial origin". In: *Proceedings of the Institute of Radio Engineers* 21.10 (1933), pp. 1387–1398.

[2] Harold Irving Ewen and Edward Mills Purcell. "Observation of a Line in the Galactic Radio Spectrum: Radiation from Galactic Hydrogen at 1,420 Mc./sec." In: *Nature* 168.4270 (1951), pp. 356–356.

[3] Harold Weaver, David RW Williams, NH Dieter, and WT Lum. "Observations of a strong unidentified microwave line and of emission from the OH molecule". In: *Nature* 208.5005 (1965), pp. 29–31.

[4] Arno A Penzias and Robert W Wilson. "A measurement of excess antenna temperature at 4080 MHz". In: *A Source Book in Astronomy and Astrophysics, 1900–1975*. Harvard University Press, 1979, pp. 873–876.

[5] Aleksander Wolszczan and Dail A Frail. "A planetary system around the millisecond pulsar PSR1257+ 12". In: *Nature* 355.6356 (1992), pp. 145–147.

[6] Wayne Hu and Martin White. "A CMB polarization primer". In: *New Astronomy* 2.4 (1997), pp. 323–344. ISSN: 1384-1076. DOI: `https://doi.org/10.1016/S1384-1076(97)00022-5`. URL: `https://www.sciencedirect.com/science/article/pii/S1384107697000225`.

[7] Mark Birkinshaw. "The sunyaev–zel'dovich effect". In: *Physics Reports* 310.2-3 (1999), pp. 97–195.

[8] Alwyn Wootten and A Richard Thompson. "The Atacama large millimeter /submillimeter array". In: *Proceedings of the IEEE* 97.8 (2009), pp. 1463–1471.

[9] GL Pilbratt, JR Riedinger, T Passvogel, G Crone, D Doyle, U Gageur, AM Heras, C Jewell, L Metcalfe, S Ott, et al. "Herschel Space Observatory-An ESA facility for far-infrared and submillimetre astronomy". In: *Astronomy & Astrophysics* 518 (2010), p. L1.

[10] Rolf Güsten, Paul Hartogh, Heinz-Wilhelm Hübers, Urs U Graf, Karl Jacobs, Hans-Peter Röser, Frank Schäfer, Rudolf T Schieder, Ronald Stark, Jürgen Stutzki, et al. "GREAT: the first-generation German heterodyne receiver for SOFIA". In: *Airborne Telescope Systems*. Vol. 4014. SPIE. 2000, pp. 23–30.

[11] Max Born and Emil Wolf. *Principles of optics: electromagnetic theory of propagation, interference and diffraction of light*. Elsevier, 2013.

[12] Terry D Oswalt. *Planets, stars and stellar systems Volume 1: Telescopes and Instrumentation*. Springer, 2013.

[13] J. Ruze. "The effect of aperture errors on the antenna radiation pattern". In: *Il Nuovo Cimento* 9.S3 (Mar. 1952), pp. 364–380. DOI: 10.1007/bf02903409. URL: https://doi.org/10.1007/bf02903409.

[14] J. Ruze. "Antenna tolerance theory—A review". In: *Proceedings of the IEEE* 54.4 (1966), pp. 633–640. DOI: 10.1109/PROC.1966.4784.

[15] Samuel Silver, ed. *Microwave antenna theory and design*. Electromagnetics and Radar. Stevenage, England: Institution of Engineering and Technology, June 1984.

[16] Jacob Baars. *The paraboloidal reflector antenna in radio astronomy and communication*. en. 2007th ed. Astrophysics and Space Science Library. New York, NY: Springer, Dec. 2007.

[17] SILVER SAMUEL. *Microwave antenna theory and design*. 1949.

[18] RHT Bates. "Holographic approach to radiation pattern measurement—I general theory". In: *International Journal of Engineering Science* 9.11 (1971), pp. 1107–1121.

[19] PJ Napier and RHT Bates. "Holographic approach to radiation pattern measurement—II experimental verification". In: *International Journal of Engineering Science* 9.12 (1971), pp. 1193–1208.

[20] Martin Ryle. "The 5-km radio telescope at Cambridge". In: *Nature* 239.5373 (1972), pp. 435–438.

[21] P F Scott and M Ryle. "A rapid method for measuring the figure of a radio telescope reflector". In: *Mon. Not. R. Astron. Soc.* 178.4 (Apr. 1977), pp. 539–545.

[22] RA Gaume, TL Wilson, FJ Vrba, KJ Johnston, and J Schmid-Burgk. "Water masers in Orion". In: *The Astrophysical Journal* 493.2 (1998), p. 940.

[23] MP Godwin, EP Schoessow, and BH Grahl. "Improvement of the Effelsberg 100 meter telescope based on holographic reflector surface measurement". In: *Astronomy and Astrophysics* 167 (1986), pp. 390–394.

[24] D Morris, JWM Baars, H Hein, H Steppe, and C Thum. "Radio-holographic reflector measurement of the 30-m millimeter radio telescope at 22 Ghz with a cosmic signal source". In: *Astronomy and Astrophysics (ISSN 0004-6361), vol. 203, no. 2, Sept. 1988, p. 399-406.* 203 (1988), pp. 399–406.

[25] Richard Hills, Youri Dabrowski, Hugh Gibson, John Richer, Harry Smith, Fred Baas, Per Friberg, Philip Jewell, Firmin Olivera, Richard Prestage, et al. "High-resolution millimetre-wave holography on the James Clerk Maxwell Telescope". In: *URSI Assembly Maastricht* (2002).

[26] IA Smith, Fred Baas, Firmin Olivera, NP Rees, Youri Dabrowski, Richard Hills, John Richer, Harry Smith, and Brian Ellison. "The New JCMT Holographic Surface Mapping System-Implementation". In: *Astronomical Data Analysis Software and Systems X.* Vol. 238. 2001, p. 93.

[27] D Morris. "Phase retrieval in the radio holography of reflector antennas and radio telescopes". In: *IEEE transactions on antennas and propagation* 33.7 (1985), pp. 749–755.

[28] Nikolic, B., Hills, R. E., and Richer, J. S. "Measurement of antenna surfaces from in- and out-of-focus beam maps using astronomical sources". In: *A&A* 465.2 (2007), pp. 679–683. DOI: `10.1051/0004-6361:20065603`. URL: `https://doi.org/10.1051/0004-6361:20065603`.

[29] D Morris, H Hein, H Steppe, and JWM Baars. "Phase retrieval radio holography in the Fresnel region: tests on the 30 m telescope at 86 GHz". In: *IEE Proceedings H-Microwaves, Antennas and Propagation.* Vol. 135. 1. IET. 1988, pp. 61–64.

[30] W Fuhr, J Staguhn, A Schulz, RE Hills, AN Lasenby, J Lasenby, M Miller, R Schieder, J Stutzki, B Vowinkel, et al. "Surface adjustment of the KOSMA 3m telescope using phase retrieval" holography"". In: *Astronomy and Astrophysics, Vol. 274, p. 975 (1993)* 274 (1993), p. 975.

[31] Stephen C. Parshley, Jörg Kronshage, James Blair, Terry Herter, Mike Nolta, Gordon J. Stacey, Andrew Bazarko, Frank Bertoldi, Ricardo Bustos, Donald B. Campbell, Scott Chapman, Nicolas Cothard, Mark Devlin, Jens Erler, Michel Fich, Patricio A. Gallardo, Riccardo Giovanelli, Urs Graf, Scott Gramke, Martha P. Haynes, Richard Hills, Michele Limon, Jeffrey G. Mangum, Jeff McMahon, Michael D. Niemack, Thomas Nikola, Markus Omlor, Dominik A. Riechers, Karl

Steeger, Jürgen Stutzki, and Eve M. Vavagiakis. "CCAT-prime: a novel telescope for sub-millimeter astronomy". In: *Ground-based and Airborne Telescopes VII*. Ed. by Heather K. Marshall and Jason Spyromilio. Vol. 10700. International Society for Optics and Photonics. SPIE, 2018, p. 107005X. DOI: 10.1117/12.2314046. URL: https://doi.org/10.1117/12.2314046.

[32] Stephen C Parshley, Scott Gramke, Ronan Higgins, Jörg Kronshage, Karl Steeger, and Klaus Willmeroth. "CCAT-prime: the Fred Young Submillimeter Telescope (FYST) final design and fabrication". In: *Ground-based and Airborne Telescopes IX*. Vol. 12182. SPIE. 2022, pp. 543–550.

[33] Simon JE Radford and Jeffery B Peterson. "Submillimeter atmospheric transparency at Maunakea, at the south pole, and at Chajnantor". In: *Publications of the Astronomical Society of the Pacific* 128.965 (2016), p. 075001.

[34] J.R. Pardo, J. Cernicharo, and E. Serabyn. "Atmospheric transmission at microwaves (ATM): an improved model for millimeter/submillimeter applications". In: *IEEE Transactions on Antennas and Propagation* 49.12 (2001), pp. 1683–1694. DOI: 10.1109/8.982447.

[35] T. E. Oberst, S. C. Parshley, G. J. Stacey, T. Nikola, A. Löhr, J. I. Harnett, N. F. H. Tothill, A. P. Lane, A. A. Stark, and C. E. Tucker. "Detection of the 205 μm [NII] Line from the Carina Nebula". In: *The Astrophysical Journal* 652.2 (Nov. 2006), pp. L125–L128. DOI: 10.1086/510289. URL: https://doi.org/10.1086/510289.

[36] *CCAT Observatory*. URL: https://www.ccatobservatory.org/.

[37] Scott C Chapman, Anthony I Huber, Adrian K Sinclair, Jordan D Wheeler, Jason E Austermann, James Beall, James Burgoyne, Steve K Choi, Abigail Crites, Cody J Duell, et al. "CCAT-prime: The 850 GHz camera for PrimeCam on FYST". In: *Millimeter, Submillimeter, and Far-Infrared Detectors and Instrumentation for Astronomy XI*. Vol. 12190. SPIE. 2022, pp. 77–91.

[38] Urs U Graf, Netty Honingh, Ignacio Barrueto, Karl Jacobs, Bernd Klein, Rocio Molina, Nicolás A Reyes, Pablo A Tapia, and Jürgen Stutzki. "CHAI, the CCAT-prime Heterodyne Array Instrument". In: *30th International Symposium on Space Terahertz Technology*. Vol. 30. 2019, p. 77.

[39] Ricardo Bustos, Mónica Rubio, Angel Otárola, and Neil Nagar. "Parque astronómico de atacama: An ideal site for millimeter, submillimeter, and mid-infrared astronomy". In: *Publications of the Astronomical Society of the Pacific* 126.946 (2014), p. 1126.

[40] E. M. Vavagiakis, Z. Ahmed, A. Ali, K. Basu, N. Battaglia, F. Bertoldi, R. Bond, R. Bustos, S. C. Chapman, D. Chung, G. Coppi, N. F. Cothard, S. Dicker, C. J. Duell, S. M. Duff, J. Erler, M. Fich, N. Galitzki, P. A. Gallardo, S. W. Henderson, T. L. Herter, G. Hilton, J. Hubmayr, K. D. Irwin, B. J. Koopman, J. McMahon, N. Murray, M. D. Niemack, T. Nikola, M. Nolta, J. Orlowski-Scherer, S. C. Parshley, D. A. Riechers, K. Rossi, D. Scott, C. Sierra, M. Silva-Feaver, S. M. Simon, G. J. Stacey, J. R. Stevens, J. N. Ullom, M. R. Vissers, S. Walker, E. J. Wollack, Z. Xu, and N. Zhu. "Prime-Cam: a first-light instrument for the CCAT-prime telescope". In: *Millimeter, Submillimeter, and Far-Infrared Detectors and Instrumentation for Astronomy IX*. Ed. by Jonas Zmuidzinas and Jian-Rong Gao. Vol. 10708. International Society for Optics and Photonics. SPIE, 2018, 107081U. DOI: `10.1117/12.2313868`. URL: `https://doi.org/10.1117/12.2313868`.

[41] Manuel Aravena, Jason E Austermann, Kaustuv Basu, Nicholas Battaglia, Benjamin Beringue, Frank Bertoldi, Frank Bigiel, J Richard Bond, Patrick C Breysse, Colton Broughton, et al. "CCAT-prime collaboration: Science goals and forecasts with Prime-Cam on the Fred Young submillimeter telescope". In: *The Astrophysical Journal Supplement Series* 264.1 (2022), p. 7.

[42] Kent D Irwin and Gene C Hilton. "Transition-edge sensors". In: *Cryogenic particle detection* (2005), pp. 63–150.

[43] Benjamin A Mazin. *Microwave kinetic inductance detectors*. California Institute of Technology, 2005.

[44] Steve K Choi, Jason Austermann, Kaustuv Basu, Nicholas Battaglia, Frank Bertoldi, Dongwoo T Chung, Nicholas F Cothard, Shannon Duff, Cody J Duell, Patricio A Gallardo, et al. "Sensitivity of the Prime-Cam Instrument on the CCAT-prime Telescope". In: *Journal of Low Temperature Physics* 199 (2020), pp. 1089–1097.

[45] I. Barrueto, U.U. Graf, C.E. Honingh, K. Jacobs, M. Justen, H. Krüger, M. Schultz, K. Vynokurova, L. Weikert, S. Wulff, and J. Stutzki. "CCAT-prime Heterodyne Instrument (CHAI) advances". In: *2022 47th International Conference on Infrared, Millimeter and Terahertz Waves (IRMMW-THz)*. 2022, pp. 1–2. DOI: `10.1109/IRMMW-THz50927.2022.9895806`.

[46] V Ossenkopf-Okada, R Schaaf, I Breloy, and J Stutzki. "Physics and Chemistry of Star Formation: The Dynamical ISM Across Time and Spatial Scales". In: *Physics and Chemistry of Star Formation: The Dynamical ISM Across Time and Spatial Scales. Proceedings of the 7th Chile-Cologne-Bonn Symposium*. 2023.

[47] C. Dragone. "Offset multireflector antennas with perfect pattern symmetry and polarization discrimination". In: *The Bell System Technical Journal* 57.7 (1978), pp. 2663–2684. DOI: 10.1002/j.1538-7305.1978.tb02171.x.

[48] Y. Mizugutch, M. Akagawa, and H. Yokoi. "Offset dual reflector antenna". In: *1976 Antennas and Propagation Society International Symposium.* Vol. 14. 1976, pp. 2–5. DOI: 10.1109/APS.1976.1147539.

[49] Huan T Tran. "Polarization comparison between on-axis and off-axis dual reflector telescopes: Zemax and Grasp8 simulations". In: *New Astronomy Reviews* 47.11 (2003). Proceedings of the Workshop on The Cosmic Microwave Background Radiation and its Polarization, pp. 1091–1096. ISSN: 1387-6473.

[50] R Güsten, LÅ Nyman, P Schilke, K Menten, C Cesarsky, and Roy Booth. "The Atacama Pathfinder EXperiment (APEX)–a new submillimeter facility for southern skies–". In: *Astronomy & Astrophysics* 454.2 (2006), pp. L13–L16.

[51] Shaul Hanany, Michael Niemack, and Lyman Page. "CMB telescopes and optical systems". In: *arXiv preprint arXiv:1206.2402* (2012).

[52] Zhilei Xu, Shunsuke Adachi, Peter Ade, JA Beall, Tanay Bhandarkar, J Richard Bond, Grace E Chesmore, Yuji Chinone, Steve K Choi, Jake A Connors, et al. "The Simons Observatory: the large aperture telescope (LAT)". In: *Research Notes of the AAS* 5.4 (2021), p. 100.

[53] Kevork N Abazajian, Peter Adshead, Zeeshan Ahmed, Steven W Allen, David Alonso, Kam S Arnold, Carlo Baccigalupi, James G Bartlett, Nicholas Battaglia, Bradford A Benson, et al. "CMB-S4 science book". In: *rXiv:1610.02743* (2016).

[54] Michael D. Niemack. "Designs for a large-aperture telescope to map the CMB 10x; faster". In: *Appl. Opt.* 55.7 (Mar. 2016), pp. 1688–1696. DOI: 10.1364/AO.55.001688. URL: https://opg.optica.org/ao/abstract.cfm?URI=ao-55-7-1688.

[55] Stephen C. Parshley, Michael D. Niemack, Richard E. Hills, Simon R. Dicker, Rolando Dünner, Jens Erler, Patricio A. Gallardo, Jon E. Gudmundsson, Terry L. Herter, Brian J. Koopman, Michele Limon, Frederick Matsuda, P. D. Mauskopf, Dominik A. Riechers, Gordon J. Stacey, and E. M. Vavagiakis. "The optical design of the six-meter CCAT-prime and Simons Observatory telescopes". In: *Astronomical Telescopes + Instrumentation.* 2018.

[56] Patricio A. Gallardo, Jon Gudmundsson, Brian J. Koopman, Frederick T. Matsuda, Sara M. Simon, Aamir Ali, Sean Bryan, Yuji Chinone, Gabriele Coppi, Nicholas Cothard, Mark J. Devlin, Simon Dicker, Giulio Fabbian, Nicholas Galitzki, Charles A. Hill, Brian Keating, Akito Kusaka, Jacob Lashner, Adrian T. Lee, Michele Limon, Philip D. Mauskopf, Jeff McMahon, Federico Nati, Michael D. Niemack, John L. Orlowski-Scherer, Stephen C. Parshley, Giuseppe Puglisi, Christian L. Reichardt, Maria Salatino, Suzanne Staggs, Aritoki Suzuki, Eve M. Vavagiakis, Edward J. Wollack, Zhilei Xu, and Ningfeng Zhu. "Systematic uncertainties in the Simons Observatory: optical effects and sensitivity considerations". In: *Millimeter, Submillimeter, and Far-Infrared Detectors and Instrumentation for Astronomy IX*. Ed. by Jonas Zmuidzinas and Jian-Rong Gao. Vol. 10708. International Society for Optics and Photonics. SPIE, 2018, 107083Y. DOI: 10.1117/12.2312971. URL: https://doi.org/10.1117/12.2312971.

[57] GRASP Version. "GRASP Version 10.5. 0, TICRA". In: *Copenhagen, Denmark* (2015).

[58] Ronan Higgins, Stephen Parshley, Xiaodong Ren, Jörg Kronshage, Scott Gramke, and Michele Limon. "CCAT-prime: mirror panel manufacture for FYST". In: *Advances in Optical and Mechanical Technologies for Telescopes and Instrumentation V*. Vol. 12188. SPIE. 2022, pp. 979–986.

[59] J. W. M. Baars, R. Lucas, J. G. Mangum, and J. A. Lopez-Perez. "Near-Field Radio Holography of Large Reflector Antennas". In: *IEEE Antennas and Propagation Magazine* 49.5 (2007), pp. 24–41. DOI: 10.1109/MAP.2007.4395293.

[60] *RPG Radiometer Physics GmbH*. URL: https://www.radiometer-physics.de/.

[61] *Reconfigurable Open Architecture Computing Hardware*. URL: https://casper.astro.berkeley.edu/wiki/ROACH2.

[62] W. V. T. Rusch. "Reflector antennas". In: *Numerical and Asymptotic Techniques in Electromagnetics*. Ed. by Raj Mittra. Berlin, Heidelberg: Springer Berlin Heidelberg, 1975, pp. 217–256. ISBN: 978-3-540-37391-9. DOI: 10.1007/3540070729_28. URL: https://doi.org/10.1007/3540070729_28.

[63] W. Wong. "On the equivalent parabola technique to predict the performance characteristics of a Cassegrainian system with an offset feed". In: *IEEE Transactions on Antennas and Propagation* 21.3 (1973), pp. 335–339. DOI: 10.1109/TAP.1973.1140477.

[64] P. Ya. Ufimtsev. "Elementary Edge Waves and the Physical Theory of Diffraction". In: *Electromagnetics* 11.2 (1991), pp. 125–160. DOI: 10.1080/02726349108908270. eprint: https://doi.org/10.1080/02726349108908270. URL: https://doi.org/10.1080/02726349108908270.

[65] P.M. Johansen. "Uniform physical theory of diffraction equivalent edge currents for truncated wedge strips". In: *IEEE Transactions on Antennas and Propagation* 44.7 (1996), pp. 989–995. DOI: 10.1109/8.504306.

[66] Joseph B. Keller. "Geometrical Theory of Diffraction∗". In: *J. Opt. Soc. Am.* 52.2 (Feb. 1962), pp. 116–130. DOI: 10.1364/JOSA.52.000116. URL: https://opg.optica.org/abstract.cfm?URI=josa-52-2-116.

[67] Graeme L James. *Geometrical theory of diffraction for electromagnetic waves*. 1. IET, 1986.

[68] W.V.T. Rusch, A. Prata, Y. Rahmat-Samii, and R.A. Shore. "Derivation and application of the equivalent paraboloid for classical offset Cassegrain and Gregorian antennas". In: *IEEE Transactions on Antennas and Propagation* 38.8 (1990), pp. 1141–1149. DOI: 10.1109/8.56949.

[69] M.S. Neiman. "The Principle of Reciprocity in Antenna Theory". In: *Proceedings of the IRE* 31.12 (1943), pp. 666–671. DOI: 10.1109/JRPROC.1943.233683.

[70] Robert E Collin and Francis J Zucker. *Antenna theory*. 1. McGraw-Hill, 1969.

[71] C. Dragone. "A first-order treatment of aberrations in Cassegrainian and Gregorian antennas". In: *IEEE Transactions on Antennas and Propagation* 30.3 (1982), pp. 331–339. DOI: 10.1109/TAP.1982.1142793.

[72] C. Granet. "Designing classical Dragonian offset dual-reflector antennas from combinations of prescribed geometric parameters". In: *IEEE Antennas and Propagation Magazine* 43.6 (2001), pp. 100–107. DOI: 10.1109/74.979502.

[73] W. Rusch, Y. Rahmat-Samii, and R. Shore. "The equivalent paraboloid of an optimized off-set cassegrain antenna". In: *1986 Antennas and Propagation Society International Symposium*. Vol. 24. 1986, pp. 639–642. DOI: 10.1109/APS.1986.1149634.

[74] Pyotr Ya Ufimtsev. *Fundamentals of the physical theory of diffraction*. John Wiley & Sons, 2014.

[75] T. Bondo and S.B. Sorensen. "Physical optics analysis of beam waveguides using auxiliary planes". In: *IEEE Transactions on Antennas and Propagation* 53.3 (2005), pp. 1062–1068. DOI: 10.1109/TAP.2004.842698.

[76] Torsten Bondo and SB Sorensen. "A fast physical optics method for the analysis of beam waveguides". In: *25th ESA Antenna Workshop on Satellite Antenna Technology*. European Space Agency. 2002, pp. 671–678.

[77] Matthew J. Griffin, Bruce Miles Swinyard, and Laurent Vigroux. "The Herschel-SPIRE instrument". In: *Optical, Infrared, and Millimeter Space Telescopes*. Ed. by John C. Mather. Vol. 5487. International Society for Optics and Photonics. SPIE, 2004, pp. 413–424. DOI: 10.1117/12.552695. URL: https://doi.org/10.1117/12.552695.

[78] Paul F Goldsmith et al. *Quasioptical systems*. Chapman & Hall New York, NY, USA, 1998.

[79] Richard S Longhurst. *Geometrical and physical optics*. Orient BlackSwan, 1973.

[80] E. Wolf and E. W. Marchand. "Comparison of the Kirchhoff and the Rayleigh–Sommerfeld Theories of Diffraction at an Aperture". In: *J. Opt. Soc. Am.* 54.5 (May 1964), pp. 587–594. DOI: 10.1364/JOSA.54.000587. URL: https://opg.optica.org/abstract.cfm?URI=josa-54-5-587.

[81] Roger Clifton Jennison. *Introduction to radio astronomy*. 1967.

[82] Todd R Hunter, Frederic R Schwab, Steven D White, John M Ford, Frank D Ghigo, Ronald J Maddalena, Brian S Mason, Jack D Nelson, Richard M Prestage, Jason Ray, et al. "Holographic measurement and improvement of the green bank telescope surface". In: *Publications of the Astronomical Society of the Pacific* 123.907 (2011), p. 1087.

[83] Constantine A Balanis. *Antenna theory: analysis and design*. John wiley & sons, 2016.

[84] Mark J Reid and James M Moran. "Masers". In: *Annual review of astronomy and astrophysics* 19.1 (1981), pp. 231–276.

[85] D. Morris, Baars J.W.M., H. Hein, H. Steppe, and C. Thum. "Radio-holographic reflector measurement of the 30-m millimeter radio telescope at 22 GHz with a cosmic signal source". In: *Astronomy and Astrophysics* 203.2 (Sept. 1988), pp. 399–406.

[86] C.E. Mayer, D.T. Emerson, and J.H. Davis. "Design and implementation of an error-compensating subreflector for the NRAO 12-m radio telescope". In: *Proceedings of the IEEE* 82.5 (1994), pp. 756–762. DOI: 10.1109/5.284742.

[87] Jacob WM Baars, Robert N Martin, Jeffrey G Mangum, Joseph P McMullin, and William L Peters. "The Heinrich Hertz telescope and the submillimeter telescope observatory". In: *Publications of the Astronomical Society of the Pacific* 111.759 (1999), p. 627.

[88] CL Carilli and MA Holdaway. "Tropospheric phase calibration in millimeter interferometry". In: *Radio Science* 34.4 (1999), pp. 817–840.

[89] OP Lay. "The temporal power spectrum of atmospheric fluctuations due to water vapor". In: *Astronomy and Astrophysics Supplement Series* 122.3 (1997), pp. 535–545.

[90] Charles E. Mayer, John H. Davis, William L. Peters, and Wolfhard J. Vogel. "A Holographic Surface Measurement of the Texas 4.9-m Antenna at 86 GHz". In: *IEEE Transactions on Instrumentation and Measurement* 32.1 (1983), pp. 102–109. DOI: 10.1109/TIM.1983.4315018.

[91] Jeffrey G Mangum, Jacob WM Baars, Albert Greve, Robert Lucas, Ralph C Snel, Patrick Wallace, and Mark Holdaway. "Evaluation of the ALMA Prototype Antennas1". In: *Publications of the Astronomical Society of the Pacific* 118.847 (2006), p. 1257.

[92] Joe Carr. *RF components and circuits*. Newnes, 2002.

[93] R. Fletcher. *Practical methods of optimization. 2nd edition*. John Wiley & Sons, 1987.

[94] *Numerical Optimization*. New York, NY: Springer New York, 2006, pp. 1–9. ISBN: 978-0-387-40065-5. DOI: 10.1007/978-0-387-40065-5_1. URL: https://doi.org/10.1007/978-0-387-40065-5_1.

[95] Adam Paszke, Sam Gross, Soumith Chintala, Gregory Chanan, Edward Yang, Zachary DeVito, Zeming Lin, Alban Desmaison, Luca Antiga, and Adam Lerer. "Automatic Differentiation in PyTorch". In: *NIPS 2017 Workshop on Autodiff*. Long Beach, California, USA, 2017. URL: https://openreview.net/forum?id=BJJsrmfCZ.

[96] S Bhatnagar PI, P Jagannathan, S Sekhar, BM Kirk, C Hull, P Cortez, S Kameno, E Fomolant, T Hunter, and C Brogan. "ALMA Study Project Report: Full-Mueller Mosaic Imaging With ALMA". In: (2021).

[97] Hugh J. Gibson, Bertrand Thomas, Luís Rolo, Martina C. Wiedner, Alain Eric Maestrini, and Peter de Maagt. "A Novel Spline-Profile Diagonal Horn Suitable for Integration Into THz Split-Block Components". In: *IEEE Transactions on*

Terahertz Science and Technology 7.6 (2017), pp. 657–663. DOI: 10.1109/TTHZ.2017.2752423.

[98] Joseph W Goodman. "Introduction to Fourier optics". In: *Introduction to Fourier optics, 3rd ed., by JW Goodman. Englewood, CO: Roberts & Co. Publishers, 2005* 1 (2005).

[99] LLC Zemax. "OpticStudio user manual". In: *Zemax LLC: Kirkland, WA, USA* (2017).

[100] Henri J Nussbaumer and Henri J Nussbaumer. *The fast Fourier transform*. Springer, 1981.

[101] Vasudevan Lakshminarayanan and Andre Fleck. "Zernike polynomials: a guide". In: *Journal of Modern Optics* 58.7 (2011), pp. 545–561.

[102] Larry R. D'Addario. *Holographic antenna measurements: Further technical considerations*. November, 1982. URL: https://www.cv.nrao.edu/~demerson/osfholo/12M_202.pdf.

[103] J Anthony Murphy and Stafford Withington. "Perturbation analysis of Gaussian-beam-mode scattering at off-axis ellipsoidal mirrors". In: *Infrared Physics & Technology* 37.2 (1996), pp. 205–219.

[104] JA Murphy. "Distortion of a simple Gaussian beam on reflection from off-axis ellipsoidal mirrors". In: *International Journal of Infrared and Millimeter Waves* 8 (1987), pp. 1165–1187.

Acknowledgements

First of all, I would like to express my deepest remembrance and gratitude to Prof. Dr. Richard Hills. It was my great fortune to work with such an insightful and omnipotent scientist. Since we worked together on the new holographic metrology for the FYST telescope in early 2018, we had numerous emails and online discussions. He never hesitated to share his wisdom on technical and non-technical issues for me. It is with great regret that I didn't in time complete this thesis and get it to him.

I would like to thank my principal advisor, Prof. Dr. Jürgen Stutzki, for supporting me in many aspects of my studies in Cologne. He served as an excellent mentor and shared with me a lot of advice about work-life balance. He spent time reading through my draft thesis and gave me a lot of valuable advice.

Dr. Urs Graf, in the past six years, served as my academic advisor and provided me with valuable advice and feedback on my research. I gained a lot of experience about Quasi-optics design for radio receivers, knowledge of Fourier Grating design and experimental skills. He read the complete draft of this dissertation, and offered great linguistic assistance.

Throughout my stay in Cologne, I have learned a lot from the interactions with my colleagues and graduate students. For this I am grateful to Marc Mertens, Sajjad Mahdizadeh, Dr. Justen Matthias, Slava Kabanovic, Ignacio Barruet, Johanna Böhm, Kateryna Vynokurova Harsha Rajan, Dr. Ronan Higgins, Ayyaz Mahmood and Adam Henning. For assistance with travel reimbursement and paper works, I am grateful to our secretaries, Bettina Krause, Steffi Krämer, et al.

Thank our Chilean collaborators, Sebastian Jorquera and Pablo Astudillo, for developing and testing the excellent electric modules of the FYST holographic system.

Many thank Bojan Nikolic, who is from Cavendish Laboratory, for his support in solving software issues and sharing his experiences about practical holographic tests.

Thank Nicolás Reyes for sharing his experimental experiences of microwave optical measurements and useful information about APEX telescope holography.

Thank Stephen Parshley for communicating with the CCAT-p observatory and providing useful information for the holographic design.

The laboratory experiments reported in this dissertation could not have been possible without support from our engineer group, Lars Weikert, Hanna and Bernard Schmidt. Lars Weikert designed and built all of the mechanical structures for the laboratory system.

It is a pleasure to acknowledge the encouragement and support of the CCAT-prime Observatory.

Finally, I would like to express my deepest gratitude to my parents, siblings and all of whom have supported me throughout my PhD study. Deepest thanks to Ms. Zhou for her companionship and understanding while I was writing this thesis

This thesis work was carried out within the Collaborative Research Centre 956, sub-project D2 and S, funded by the Deutsche Forschungsgemeinschaft (DFG) - project ID 184018867.

Appendix A.

Optical Parameters of FYST and Laboratory Antenna

FYST employs an advanced 'Crossed-Dragone' (CD) optics which is made of two similar-sized mirrors and arranges them off-axis to achieve a large field of view without optical blockage in the telescope's aperture. Figure A.1 shows the optics of FYST. The two-mirror system is designed by satisfying the Mitzuguchi-Dragone criterion [47][48], so that its optics can be equivalent to a symmetrical parabolic mirror [68][73] and offers a circular symmetrical beam pattern and very low cross-polarization performance [49]. The field of view of FYST is further improved by minimizing the coma aberrations. 7.8 degrees field of view at the wavelength of 3mm is achieved. The details of the FYST optical design and the technique of coma correction are summarized by Stephen Parshley in paper [55][31]. This section shows the details of the geometry of FYST. The optical parameters of FYST and the small laboratory antenna described in chapter 6 are presented. The mirror surfaces and practical panel layout of FYST are also given.

Classical Crossed-Dragone Antenna Design

The classical offset two-mirror antenna is fully characterized by 20 parameters, which is explained by Granet in paper [72]. The paper also indicates that these parameters can be computed from 5 specific parameters given by the designer. Granet offered 5 different options for the design parameters. Here, the following 5 parameters are used as the design parameters: primary diameter D_m, the offset angel of the primary θ_0, the distance between two mirrors L_m, the angle between feed axis and secondary edge θ_e, and angle between the primary axis and feed axis θ_p. The initial optics is based on the design studied by M. Niemack [54]. Then the geometry is modified to increase the clearance between the edges of the mirrors and the optical beam. Figure A.2 shows the optical diagram of the designed optics. It is found that the path traced by the chief ray inside the telescope forms a triangle with side in the proportion 3:4:5. Table A.1

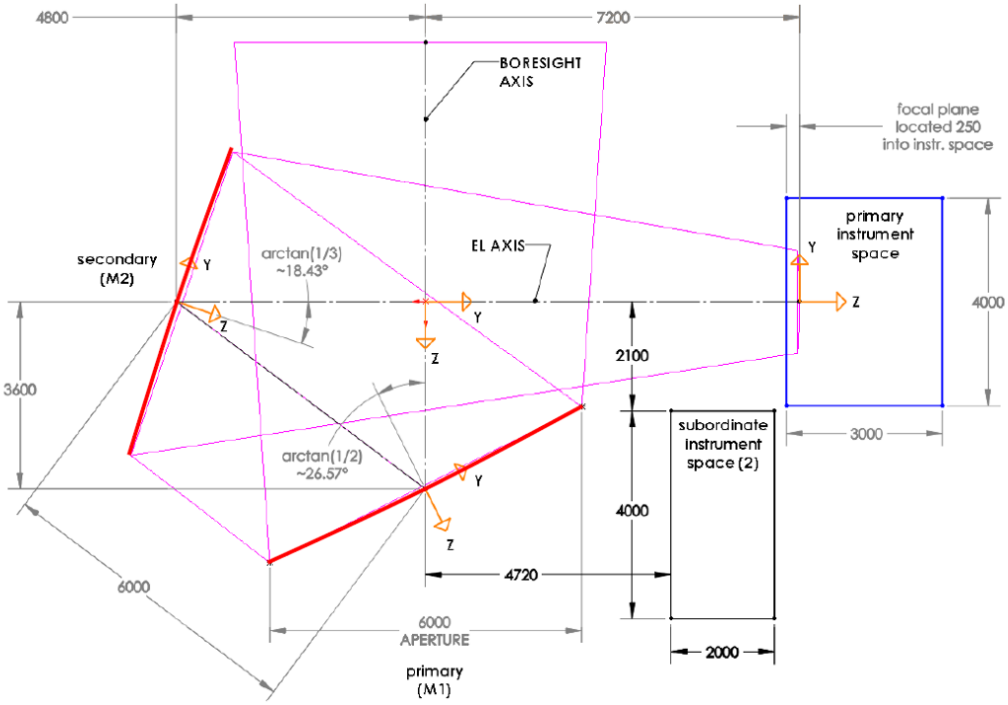

Figure A.1.: 2D layout slice showing the modified crossed-Dragone optical design for CCAT-prime. The optical beam is magenta and mirror sections are red. All linear dimensions are in millimeters, and numbers without decimal points are exact. Local coordinate systems for the primary (M1), the secondary (M2), and the focal plane (FP) are illustrated in orange for the y and z axes (x axes follow the "right-hand rule" convention, they all go into the page). The "world" coordinate system is the intersection of the boresight and elevation axes.

lists the all optical parameters describing the geometry of FYST. The third column in the table is the dimensionless value shown in the optical diagram, and the fourth gives the number scaled for FYST. The small laboratory antenna is designed by scaling the FYST model by a factor of 15. To increase the clearance at edge of the mirror of the scale model, the distance of the two mirrors is increased from 400mm to 450mm.

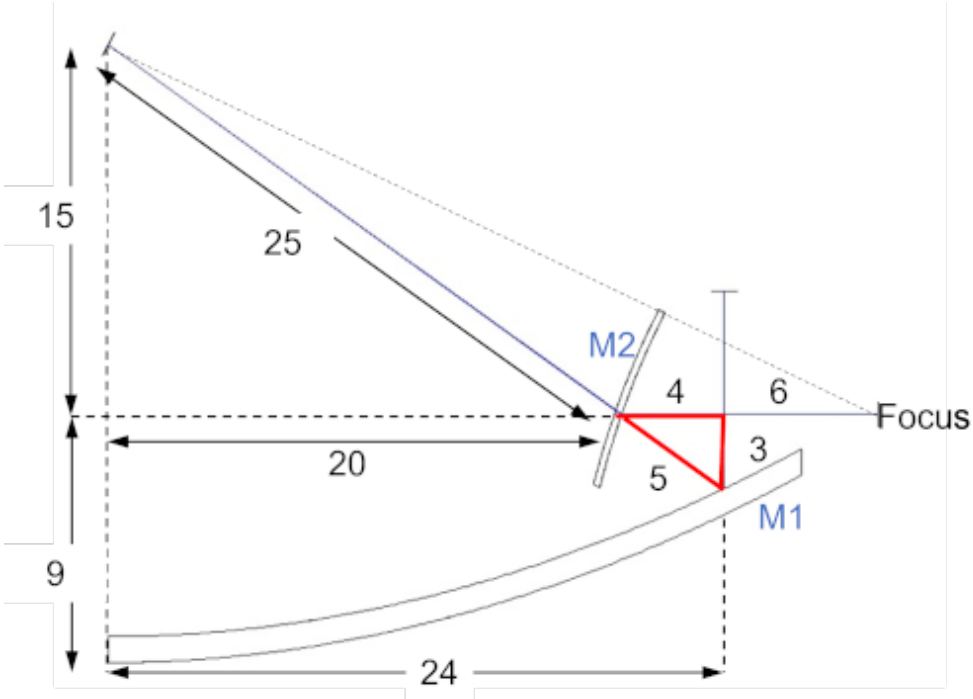

Figure A.2.: Diagram of the FYST optics satisfying the Mitzuguchi-Dragone criterion. Path traced by the chief ray inside the telescope forms a triangle with side in the proportion 3:4:5, which is outlined in red.

Comatic Correction and Mirror Surface

Based on the initial optical design, the comatic aberrations are corrected by reshaping the mirror surfaces to the rms spot size for a set of points in the focal plane. The configuration of the new optics still satisfies the Mizuguchi-Dragone condition. It is found that the usable field of view for high frequency is significantly improved, see Figure A.3. The mirror surfaces are expressed by a polynomial equation in local coordinate system that is explained in Figure A.1. The general form of the mirror surface polynomials are defined by

$$z(x,y) = \sum_{i=0}^{k}\sum_{j=0}^{k} a_{ij}(\frac{x}{R_N})^i(\frac{y}{R_N})^j, \tag{A.1}$$

where z is the mirror sag at a given x and y position, R_N is the normalized factor

			FYST	**Lab Antenna**
Aperture Diameter	$\mathbf{D_m}$	5	6000	400
Offset angle on MR	$\theta_\mathbf{0}$	$tan^{-1}(4/3)$	53.13°	53.13°
Distance MR to SR	$\mathbf{L_m}$	5	6000	450
Angle of edge ray	$\theta_\mathbf{e}$	$2tan^{-1}(D_m/4f_{eff})$	11.894°	11.894°
Angle between boresight and feed axis	$\theta_\mathbf{p}$	90	90	90
MR focal length	F	24	28800	1920
Offset distance on MR	h	24	28800	1920
SR eccentricity	e	$\sqrt{5}$	2.236	2.236
SR parameter	a	7.5	9000	585
Half inter-focal distance	f	$7.5 \times \sqrt{5}$	20124.6	1308.1
Angle between MR and SR axes	β	$tan^{-1}(2)$	63.435°	63.425°
Angle between Feed and SR axes	α	$tan^{-1}(1/2)$	26.565°	26.565°
Distance SR to Feed, on axis	L_s	10	12000	780
Distance SR to primary focus	L_p	25	30000	1950
SR conic constant	$K = -e^2$	-5	-5	-5
SR radius of curvature	$R_s = a(e^2 - 1)$	30	36000	2340
Magnification of SR on axis	m=(e-1)/(e+1)	$(\sqrt{5} - 1)/(\sqrt{5} + 1)$	0.382	0.382
Actual Magnification	$M = L_S/L_p$	0.4	0.4	
Effective focal length	$f_{eff} = M(L_p + L_m)$	12	14400	960
MR chief ray angle of incidence	inc_p	$tan^{-1}(1/2)$	26.565°	26.565°
SR chief ray angle of incidence	inc_s	$tan^{-1}(1/3)$	18.435°	18.435°

Table A.1.: Optical characteristics of the initial FYST design and the small laboratory antenna. The third column gives the values in the arbitrary units used in the diagram and the fourth gives the numbers scaled for FYST. The parameters of the designed laboratory model are shown in fifth column.

and called normalization radius, k is the maximum polynomial power, and a_{ij} are the coefficients. Here, for the primary mirror, the maximum polynomial power k is 6, and for the secondary mirror $k = 7$. The two mirrors use $R_N = 3000\ mm$. The polynomials describing the classical parabolic and hyperbolic surfaces are listed in table A.2. For the modified surfaces are summarized in table A.3.

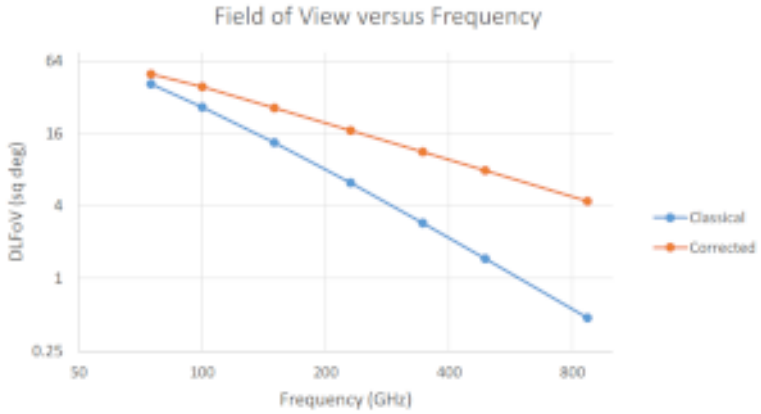

Figure A.3.: Diffraction limited FOV of the coma-corrected optics as a function of frequency.

Parabolic Primary (M1)								
a_{ij}	$j=0$	$j=1$	$j=2$	$j=3$	$j=4$	$j=5$	$j=6$	
$i=0$	0	0	−55.90169	1.04167	−0.02429	0.00063	0.0906601	
$i=1$	0	0	0	0	0	0	0	
$i=2$	−69.87712	1.30208	−0.03643	0.00113	0.2610568	0	0	
$i=3$	0	0	0	0	0	0	0	
$i=4$	−0.00759	0.00042	0.2177414	0	0	0	0.0906601	
$i=5$	0	0	0	0	0	0	0	
$i=6$	0.0394559	0	0	0	0	0	0	
Hyperbolic Secondary (M2)								
a_{ij}	$j=0$	$j=1$	$j=2$	$j=3$	$j=4$	$j=5$	$j=6$	$j=7$
$i=0$	0	0	106.72691	5.90623	−0.25866	−0.07904	−0.00306	0.00081
$i=1$	0	0	0	0	0	0	0	0
$i=2$	118.58541	6.56249	−0.93772	−0.19574	−0.00084	0.00364	0	0
$i=3$	0	0	0	0	0	0	0	0
$i=4$	−0.72256	−0.11993	0.01061	0.00517	0	0	0	0
$i=5$	0	0	0	0	0	0	0	0
$i=6$	0.00863	0.00237	0	0	0	0	0	0
$i=7$	0	0	0	0	0	0	0	0

Table A.2.: Polynomial Coefficients (a_{ij}) for the mirror surfaces of the classical Cross-Dragone Optics.

Modified Primary (M1)

a_{ij}	$j=0$	$j=1$	$j=2$	$j=3$	$j=4$	$j=5$	$j=6$	
$i=0$	0	0	−57.74022	1.5373825	1.154294	−0.441762	0.0906601	
$i=1$	0	0	0	0	0	0	0	
$i=2$	−72.17349	1.8691899	2.8859421	−1.026471	0.2610568	0	0	
$i=3$	0	0	0	0	0	0	0	
$i=4$	1.8083973	−0.603195	0.2177414	0	0	0	0.0906601	
$i=5$	0	0	0	0	0	0	0	
$i=6$	0.0394559	0	0	0	0	0	0	

Modified secondary (M2)

a_{ij}	$j=0$	$j=1$	$j=2$	$j=3$	$j=4$	$j=5$	$j=6$	$j=7$
$i=0$	0	0	103.90461	6.6513025	2.8405781	−0.7819705	−0.0400483	0.0896645
$i=1$	0	0	0	0	0	0	0	0
$i=2$	115.44758	7.3024355	5.7640389	−1.578144	−0.0354326	0.2781226	0	0
$i=3$	0	0	0	0	0	0	0	0
$i=4$	2.9130983	−0.8104051	−0.0185283	0.2626023	0	0	0	0
$i=5$	0	0	0	0	0	0	0	0
$i=6$	−0.0250794	0.0709672	0	0	0	0	0	0
$i=7$	0	0	0	0	0	0	0	0

Table A.3.: Polynomial Coefficients (a_{ij}) for the mirror surfaces with coma correction

Appendix B.

Optics in the Reference Receiver Module

The reference receiver shares the same electronic design with the signal receiver. The receivers employ a spline-profile diagonal horn described in paper [97] and offers a Gaussian beam with half power beam width (HPBW) of around 16 degrees. In the FYST holography system, the beam of the telescope will be measured by recording the product of the signals from the signal receiver and reference receiver. According to the noise theory of a correlation receiver [102], the quality of the recorded holographic beam is determined by the signal-to-noise ratio of the two receivers. Therefore, to improve the quality of the measured beams, additional optics is designed and placed in the front of the reference receiver chain to enlarge the signal collection area and improve its optical gain. Since the reference receiver will be mounted in the yoke of the telescope and rotate with the telescope in azimuth, during the beam scan, to avoid the gain reduction due to receiver pointing offset, the Gaussian beam reshaped by the additional optics has to cover the holographic beam measurement range which is around ± 0.4 degrees at 300GHz. Here, we choose a Gaussian beam with HPBW of around 1.1 degrees as the desired reference receiver beam. Off-axis mirrors are used to converge the HPBW of the feed horn from 16 degrees to 1.1 degrees. In this section, Gaussian beam transformation method of using off-axis curved mirrors is presented and employed to design the receiver optics.

Gaussian Beam Transformation

The electric field E distribution of a propagating Gaussian beam can be represented by its beam waist size w_0 through the following expression[78]

$$E(r,z) = \sqrt{\frac{2}{\pi w(z)^2}} \cdot exp(\frac{-r^2}{w(z)^2} - jkz - \frac{j\pi r^2}{\lambda R(z)} + j\phi_0(z)) \tag{B.1a}$$

$$R(z) = z + \frac{1}{z}(\frac{\pi w_0^2}{\lambda})^2 \tag{B.1b}$$

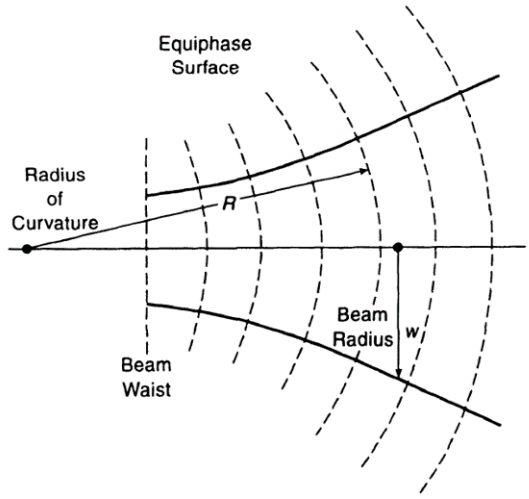

Figure B.1.: Schematic diagram of Gaussian beam propagation.

$$w(z) = w_0 \cdot \sqrt{1 + (\frac{\lambda z}{\pi w_0^2})^2} \tag{B.1c}$$

$$\phi_0(z) = tan^{-1}(\frac{\lambda z}{\pi w_0^2}), \tag{B.1d}$$

where, z is the distance between the field and beam waist, $w(z)$ is the Gaussian beam radius in plane z that is perpendicular to the wave propagating direction, $R(z)$ and $\phi_0(z)$ are radius of wavefront curvature and Gaussian beam phase shift respectively. Figure B.1 shows the schematic diagram of Gaussian beam propagation. We can see the phase center of the beam wavefront is changing along the propagating direction. A critical parameter is called confocal distance z_c which determines the near or field region of the beam. After beam propagation of a distance on the order of the confocal distance, the beam increases significantly and its phase center would be close to the position of the beam waist of the beam. The confocal distance is defined by equation

$$z_c = \frac{\pi w_0^2}{\lambda}. \tag{B.2}$$

Off-axis mirrors with quadric surfaces are commonly used as focusing elements for controlling the properties of Gaussian beams at millimeter and sub-millimeter wavelength. For example, the elliptical mirror in Figure B.2, the phase center of the input Gaussian beam at point P on the mirror (red curve) is placed in a focus F_0 of the mirror, the elliptical mirror can change the curvature of the beam wavefront and convert the reflected beam phase center to the point F_1. The radius R_{in} and R_r of the wavefront curvature

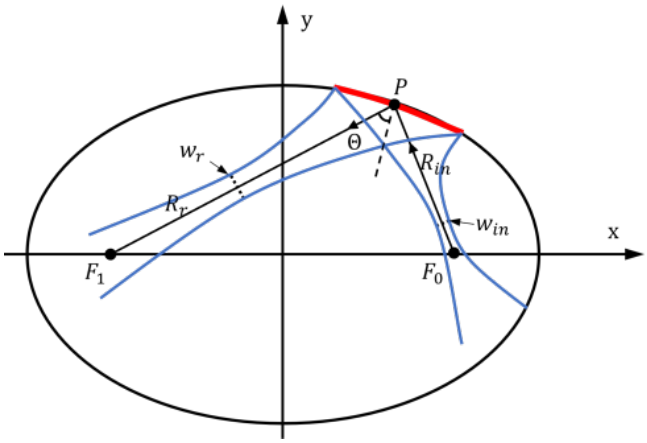

Figure B.2.: Schematic of Gaussian beam transformation by a elliptical mirror.

and mirror local focal length f are related by the following expression

$$\frac{1}{f} = \frac{1}{R_{in}} + \frac{1}{R_r}. \tag{B.3}$$

The sign of R_{in} and R_r should be positive for a real phase center and negative for the case with a virtual one. The distance (d_{in}) between beam waist of the input beam and point P on the mirror can be calculated by equation B.1b. If we assume the quadratic mirror acts as a thin lens, the beam waist w_r of the reflected beam and its position can be found by using ABCD law and calculated by equation B.4, which is presented in chapter 3 of book [78].

$$w_r = \frac{w_{in}}{\sqrt{(d_{in}/f - 1)^2 + (z_c/f)^2}} \tag{B.4a}$$

$$\frac{d_r}{f} = 1 + \frac{d_{in}/f - 1}{(d_{in}/f - 1)^2 + (z_c/f)^2} \tag{B.4b}$$

When the reflection angle of the beam(2Θ) is defined, the geometry of the mirror surface can be determined by the parameters a, b and c, which is resolved by formula B.5 using the computed R_{in}, R_r and Θ. In the case where $R_{in}R_r$ is negative, b is a imaginary number which means the surface of the mirror is hyperbolic.

$$a = \frac{R_{in} + R_r}{2} \tag{B.5a}$$

$$b^2 = \frac{R_{in}R_r(1 \pm cos(2\Theta))}{2} \tag{B.5b}$$

$$(2c)^2 = R_{in}^2 + R_r^2 - 2R_{in}R_r cos(\Theta) \tag{B.5c}$$

Two-Mirror Optics for the Reference Receiver

In the Gaussian beam transformation elements design, it is convenient to use beam waist to represent the beam. Therefore, the beam with 16 degrees and 1.1 degrees HPBW can be described by the beam with beam waist size of 1.4mm and 20mm respectively. A two-mirror system is used to transfer the Gaussian beam twice and achieve the final 20mm beam waist. The diagram about the beam transformation is shown in Figure B.3. The detail of the Gaussian beam parameters and the focal length of the mirrors are summarized in table B.1.

Mirror	w_{in}	d_{in}	R_{in}	w_r	d_r	R_r	f
M1	1.4	33.79	34.87	2.765	-63.54	-72.33	67.34
M2	2.765	170.54	173.82	20	146.938	10553.04	171.004

Table B.1.: The quasi-optical parameters of the two mirrors at frequency of 300GHz. The units in the table is millimeter.

The reflecting mirror has to be off-axis to avoid blockage in the optical path, which results in the distortion effects on the reflection beam from the off-axis mirror. The beam distortion of a fundamental Gaussian beam on the reflection from an off-axis elliptical mirror was studied in paper [103][104]. The paper [104] also presents the way of employing two-mirror system to compensate the beam distortions by properly orienting the secondary mirror and adjusting the distance between two mirrors. Here, the configuration that is similar to the 'crossed-Dragone' optics is adopted. The reflection angle of the beams on both mirror surfaces is 90 degrees, which folds back the receiver beam and make the module compact. The view of the designed optical model, receiver box and beams are shown in Figure B.4.

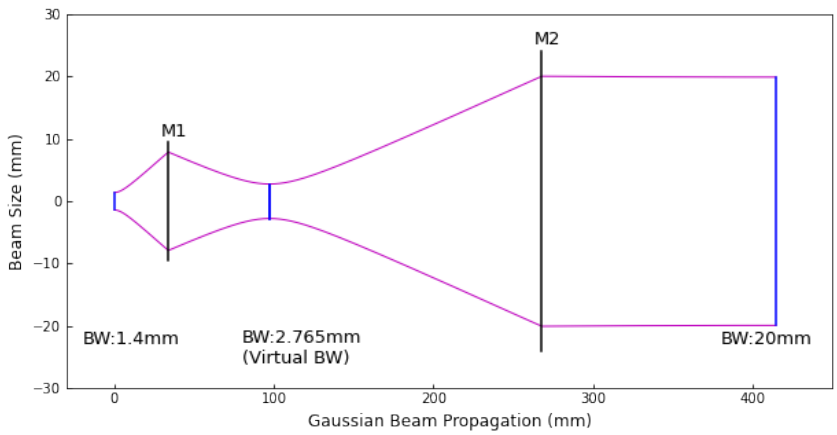

Figure B.3.: Schematic of the Gaussian transformations of the two-mirror system.

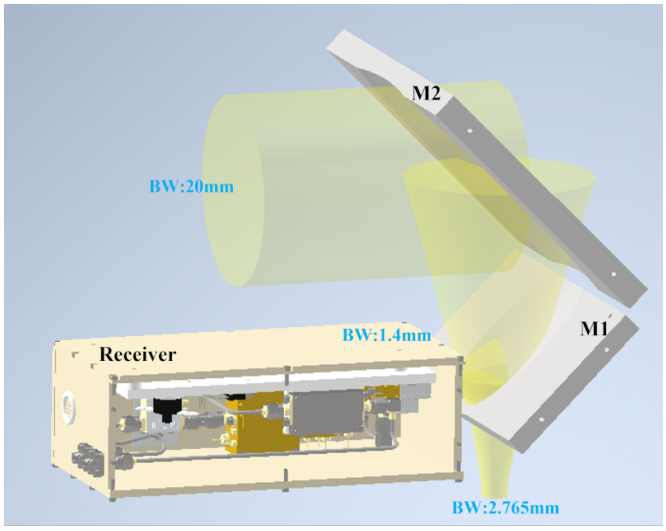

Figure B.4.: View of the CAD model of the reference receiver module and optics.

The far-field electromagnetic beam of the module is simulated by the GRASP package using the method of physical optics, which agrees with the designed 1.1 degrees HPBW. Figure B.5 shows the cut plot of the amplitude and phase beam pattern in azimuth. The optical efficiency decreases by around 1.6dB as the telescope points to the edge of the holographic beam map (±0.4 degrees). It also has been found that this optical layout offers approximately symmetrical Gaussian beam and low cross-polarization, see figure B.6.

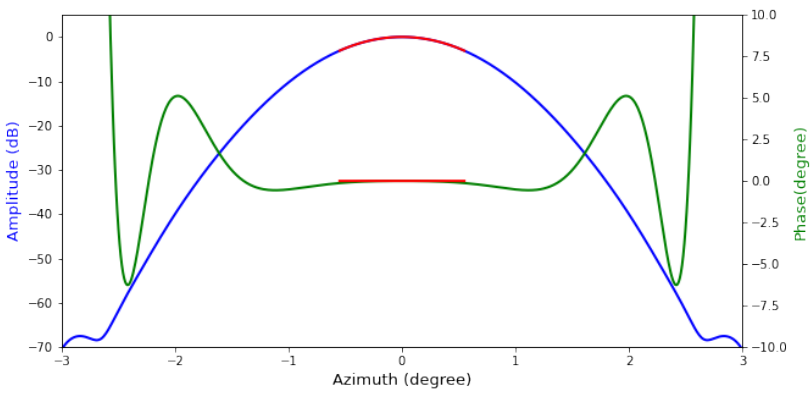

Figure B.5.: Simulated beam of the designed reference receiver optics. The amplitude beam pattern (blue curve) and phase pattern (green). The red curves are used angular region during holographic scan.

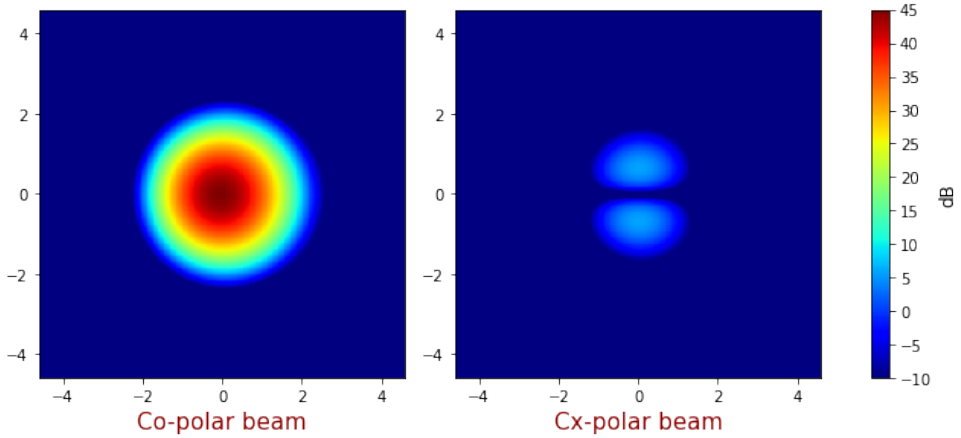

Figure B.6.: Simulated beam patterns of the designed reference Rx optics. Co-polarization beam map (left) and crossed-polarization beam (right).

Erklärung zur Dissertation

gemäß der Promotionsordnung vom 12. März 2020

Hiermit versichere ich an Eides statt, dass ich die vorliegende Dissertation selbstständig und ohne die Benutzung anderer als der angegebenen Hilfsmittel und Literatur angefertigt habe. Alle Stellen, die wörtlich oder sinngemäß aus veröffentlichten und nicht veröffentlichten Werken dem Wortlaut oder dem Sinn nach entnommen wurden, sind als solche kenntlich gemacht. Ich versichere an Eides statt, dass diese Dissertation noch keiner anderen Fakultät oder Universität zur Prüfung vorgelegen hat; dass sie - abgesehen von unten angegebenen Teilpublikationen und eingebundenen Artikeln und Manuskripten - noch nicht veröffentlicht worden ist sowie, dass ich eine Veröffentlichung der Dissertation vor Abschluss der Promotion nicht ohne Genehmigung des Promotionsausschusses vornehmen werde. Die Bestimmungen dieser Ordnung sind mir bekannt. Darüber hinaus erkläre ich hiermit, dass ich die Ordnung zur Sicherung guter wissenschaftlicher Praxis und zum Umgang mit wissenschaftlichem Fehlverhalten der Universität zu Köln gelesen und sie bei der Durchführung der Dissertation zugrundeliegenden Arbeiten und der schriftlich verfassten Dissertation beachtet habe und verpflichte mich hiermit, die dort genannten Vorgaben bei allen wissenschaftlichen Tätigkeiten zu beachten und umzusetzen. Ich versichere, dass die eingereichte elektronische Fassung der eingereichten Druckfassung vollständig entspricht

Xiaodong, Ren.